論文 / 著書情報
Article / Book Information

題目(和文)	
Title(English)	Study on Operation and Control of Isolated Bidirectional DC-DC Converter with Cascaded Converters for Battery Energy Storage Systems
著者(和文)	羅天
Author(English)	TIAN LUO
出典(和文)	学位:博士(学術), 学位授与機関:東京科学大学, 報告番号:甲第379号, 授与年月日:2025年3月26日, 学位の種別:課程博士, 審査員:萩原 誠,藤田 英明,竹内 希,清田 恭平,佐野 憲一朗,小原 秀嶺
Citation(English)	Degree:Doctor (Academic), Conferring organization: Institute of Science Tokyo, Report number:甲第379号, Conferred date:2025/3/26, Degree Type:Course doctor, Examiner:,,,,,
学位種別(和文)	博士論文
Type(English)	Doctoral Thesis

東京科学大学
INSTITUTE OF SCIENCE TOKYO

工学院
SCHOOL OF ENGINEERING

電気電子コース
COURSE OF ELECTRICAL AND ELECTRONIC ENGINEERING

STUDY ON OPERATION AND CONTROL OF ISOLATED BIDIRECTIONAL DC-DC CONVERTER WITH CASCADED CONVERTERS FOR BATTERY ENERGY STORAGE SYSTEMS

DOCTORAL THESIS

STUDENT	SUPERVISOR
	Associated Professor
Tian Luo	Makoto Hagiwara

30th/January/2025

Foreword

Before delving into this dissertation, I would like to share a few thoughts with you. As written on the cover page, this is a doctoral thesis about DC-DC power converters. If you are searching for research in this field, I am truly honored that this work might serve as a valuable reference for you. If your interests lie elsewhere, I am equally grateful that you have found your way to my research and are taking the time to read this foreword.

I do not refer to any technical knowledge or specific expertise, but rather a mindset—a way of approaching life and thinking problems in this foreword. I hope this can really help you and be a reference to your work and life.

First, embrace your present circumstances with a positive outlook, whatever the challenges you are facing. Perhaps, like me in 2024, you are overwhelmed by the demands of pursuing a degree. Maybe you are feeling dejected after a stern critique from your supervisors last week. You might be anxious about not getting your dream job offer or frustrated that the experimental setup you spent months designing has failed to work as expected. When these moments arise, set aside your work (unless tomorrow is the deadline!) and step out of your office or home. Spend an entire day breathing in fresh air and reconnecting with the world outside. Remember, as long as you keep moving forward, things will improve. Suffering is not a prerequisite for solving problems, but a good night's sleep often is.

Additionally, cherish the people around you—your friends, family, and supervisors. Their contributions to your journey are not limited to material support; they enrich your heart and soul, shaping the unique individual you are today.

Finally, do not take all the ideas presented in this thesis at face value. Even if you feel uncertain, approach everything with a critical mindset. I once published an article in one of the most esteemed journals in our field with an error in a formula, and the reviewers did not catch it. Regrettably, even after I discovered the mistake, I could no longer revise it. This serves as a reminder: you should never place blind trust in "authority," whether it is historical figures or your supervisors. It is up to you to discern what is right and wrong through your own reasoning. If you find yourself questioning a particular formula or explanation, trust yourself rather than what you see or hear.

Abstract

This dissertation presents a study on a three-phase isolated bidirectional DC-DC power converter based on three-phase dual-active-bridge (TP-DAB) converter and multilevel cascaded converters. The proposed converter is suitable for battery energy storage systems.

In the first part, a three-phase cascaded converters DC-DC converter using cascaded choppers, Yn-Y transformer, and neutral point wire is introduced (Chapter 3). Compared with the TP-DAB converter, it has advantages such as low RMS current, low peak current, and high conversion efficiency especially under light-load conditions. In addition, an improvement method applying variable duty ratios to the two three-phase bridges in the proposed converter is discussed (Chapter 4). The variable-duty method can almost eliminate the zero-sequence current component and then further reduce the RMS and peak currents possibly flowing in the circuit. All the verifications of this part are based on mathematical calculations and downscale experimental results.

Furthermore, the cascaded converters DC-DC converters can be categorized into four types based on the presence or absence of a neutral point wire of the Yn-Y transformer and the type of cascaded converters used. The first part of this dissertation discusses the simplest, basic type cascaded converters DC-DC converter. However, the basic type suffers from overmodulation issues, which limit the voltage conversion ratio and output current. In another part of this dissertation (Chapter 5), other types of three-phase cascaded converter DC-DC converters will be discussed. These converters utilize floating voltage, full-bridge converters, or both to overcome overmodulation issues, thereby eliminating the limitations on the voltage conversion ratio and current. Finally, this dissertation provides a cost index approach to evaluate the remaining three types of converters.

Abbreviations

AC	Alternating Current
CC	Cascaded Choppers
CFB	Cascaded Full-Bridge
DAB	Dual Active Bridge
DC	Direct Current
DPS	Dual Phase Shift
DSP	Digital Signal Processor
EPS	Extended Phase Shift
ESS	Energy Storage System
EV	Electric Vehicle
FB	Full Bridge
FPGA	Field Programmable Gate Array
HB	Half Bridge
HVDC	High Voltage Direct Current
IGBT	Insulated-Gate Bipolar Transistor
KVL	Kirchhoff's Voltage Law
LVDC	Low Voltage Direct Current
MMC	Modular Multilevel Converter
MOSFET	Metal-Oxide-Semiconductor Field-Effect Transistor
MPPT	Maximum Power Point Track
NNPW	None-Neutral-Point-Wire Type
NPC	Neutra-Point-Clamped
NPW	Neutral-Point-Wire Type
PCS	Power Conversion System
PI	Proportional-Integral
PLL	Phase-Locked Loops
PS-PWM	Phase Shifted Pulse Width Modulation
PV	Photovoltaic
PWM	Pulse Width Modulation

RES	Renewable Energy Source
RMS	Root Mean Square
SoC	State of Charge
SP	Single-Phase
SPS	Single Phase Shift
STATCOM	Static Synchronous Compensator
TP	Three-Phase
TPS	Triple Phase Shift
ZCS	Zero Current Switching
ZVS	Zero Voltage Switching

NOMENCLATURE

V_{dc1}	DC Input Voltage
V_{dc2}	DC Output Voltage
$i_{\mathrm{u1,\ v1,\ w1}}$	Phase Current of Each Phase in Primary Side
$i_{\mathrm{u2,\ v2,\ w2}}$	Phase Current of Each Phase in Secondary Side
${i_{\mathrm{u1}}}^{*}$	Desired Current of U-Phase
${i_{\mathrm{u1}}}^{**}$	Compensated Reference of ${i_{\mathrm{u1}}}^{*}$ for Control System
i_{dc1}	DC Input Current
i_{dc2}	DC Output Current
i_{L}	Inductor Current of Single-Phase DAB Converter
γ	Voltage Conversion Ratio
n	Windings Turns Ratio of Transformer
N	Quantity of Cascaded Choppers per Phase
$v_{\mathrm{au,\ av,\ aw}}$	Output Voltages of Auxiliary Converters
$v_{\mathrm{cu}x,\ \mathrm{cv}x,\ \mathrm{cw}x}$	DC-Capacitor Voltages for Cascaded Choppers
${V_{\mathrm{c}}}^{*}$	Command Value of $v_{\mathrm{cu}x,\ \mathrm{cv}x,\ \mathrm{cw}x}$
$v_{\mathrm{tu1,\ tv1,\ tw1}}$	Transformer Voltages of Each Phase in Primary Side
$v_{\mathrm{tu2,\ tv2,\ tw2}}$	Transformer Voltages of Each Phase in Secondary Side
$v_{\mathrm{Mu1,\ Mv1,\ Mw1}}$	Output Voltage of Main Converter 1 in Each Phase
$v_{\mathrm{Mu2,\ Mv2,\ Mw2}}$	Output Voltage of Main Converter 2 in Each Phase
$v_{\mathrm{Lu,\ Lv,\ Lw}}$	Voltage of Series Inductor in Each Phase
η	Conversion Efficiency
f_{s1}	Switching Frequency of Main Converters
f_{s2}	Switching Frequency of Cascaded Choppers
T_{s1}	Switching Period of Main Converters
T_{s1}	Switching Period of Auxiliary Converters
T_{d}	Deadtime of Auxiliary Converters
ω_{s1}	Angular Frequency of f_{s1}
ω_{s2}	Angular Frequency of f_{s2}

Q_x	Active Power Devices in Main Converters
$\mathrm{Q}_{\mathrm{a}x}$	Active Power Devices in Cascaded Converters
$\mathrm{S}_{\mathrm{Q}x}$	Gate Logic Value for Indicated Power Device Q_x
$v_{\mathrm{du,\ dv,\ dw}}$	Compensation Voltages for Dead Time in Each Phase
$(v_{\mathrm{au,\ av,\ aw}})_x$	Equivalent Values to ($v_{\mathrm{Mu1,\ Mv1,\ Mw1}}$-$v_{\mathrm{tu1,\ tv1,\ tw1}}$)
$(v_{\mathrm{au,\ av,\ aw}})_y$	Equivalent Values to (-$v_{\mathrm{Lu,\ Lv,\ Lw}}$)
d_1	Duty Ratio of Main Converter 1
d_2	Duty Ratio of Main Converter 2
$d_{\mathrm{u}x,\ \mathrm{v}x,\ \mathrm{w}x,}$	Duty Ratio of the x^{th} Chopper in Each Phase
$i_{\mathrm{ac\_u,\ v,\ w}}$	AC Component of $i_{\mathrm{u1,\ v1,\ w1}}$
$i_{\mathrm{ac\_u,\ v,\ w}}{}^{*}$	Reference AC Component of $i_{\mathrm{u1,\ v1,\ w1}}$
I_{ac}	Amplitude of $i_{\mathrm{ac\_u,\ v,\ w}}$
I_{max}	Maximum I_{ac} without Overmodulation
$I_{\mathrm{ac}}{}^{*}$	Command Value of I_{ac}
I_{dc}	Value of DC Component of $i_{\mathrm{u1,\ v1,\ w1}}$
i_n	Zero Sequence Current
K_{P}	Proportional Coefficient of P Control in Current Controller
P_{in}	Input Power of Converter
P_{o}	Output Power of Converter
P_{e}	Rated Power
P_{max}	Maximum Output Power without Overmodulation
$P_{\mathrm{a\_au}}$	Active Power of U-Phase Auxiliary Converter
I_{peak}	Peak Current of Phase Currents $i_{\mathrm{u1,\ v1,\ w1}}$
I_{RMS}	RMS Current of Phase Currents $i_{\mathrm{u1,\ v1,\ w1}}$
L_{k}	Leakage Inductance of Transformer in Each Phase
L_{s}	Inductance of Series Inductor in Each Phase
L	Total Series Inductance (Including L_{s} and L_{k})
C_{in}	Input Capacitance
C_{o}	Output Capacitance
C_{a}	DC-Capacitance of Each Cascaded Chopper
δ	Radian
t	Time
M_{I}	Modulation Index

M_{IU}	Modulation Index for U-Phase Auxiliary Converter
ϕ	Phase Shift Angle
Θ_{peak}	Reduction Rate of Peak Current
Θ_{rms}	Reduction Rate of RMS Current
S	Apparent Power
Q	Reactive Power
P	Active Power
D	Distortion Power
PF	Displacement Power Factor
PF_{ot}	Total Power Factor

OUTLINE

Chapter 1 INTRODUCTION

1.1 Research Background

1.1.1 Industrial Revolutions and Electrification

The development of human society is closely linked to the evolution of energy forms. Several centuries ago, the primary energy source for human society was manual labor. During this time, large-scale activities were challenging to undertake, which is why The Pyramids were considered one of “ancient wonders”. In 1760, the onset of the First Industrial Revolution marked the beginning of the transition from traditional agrarian society to the industrial age. From this point, the primary energy source shifted from manual labor to mechanical energy. Mechanical energy, being a more powerful source, replaced manual labor and significantly advanced society's economy, transportation, and agriculture. However, the achievements of the First Industrial Revolution were not without flaws; it faced three major issues:

- Mechanical energy is primarily obtained through the process of “resource”-“combustion”-“heating”-“pressurization”-“drive” (“RCHPD”). The inefficient energy production methods may lead to potential resource shortages in human society
- Mechanical energy is a difficult-to-control form of energy.
- The processes of "combustion" and "heating" are unavoidable and pose environmental hazards.

In fact, although mechanical energy, represented by steam engines, did indeed elevate the level of industrialization, the energy efficiency at that time was very low. For example, even the best steam engines in history achieving an efficiency

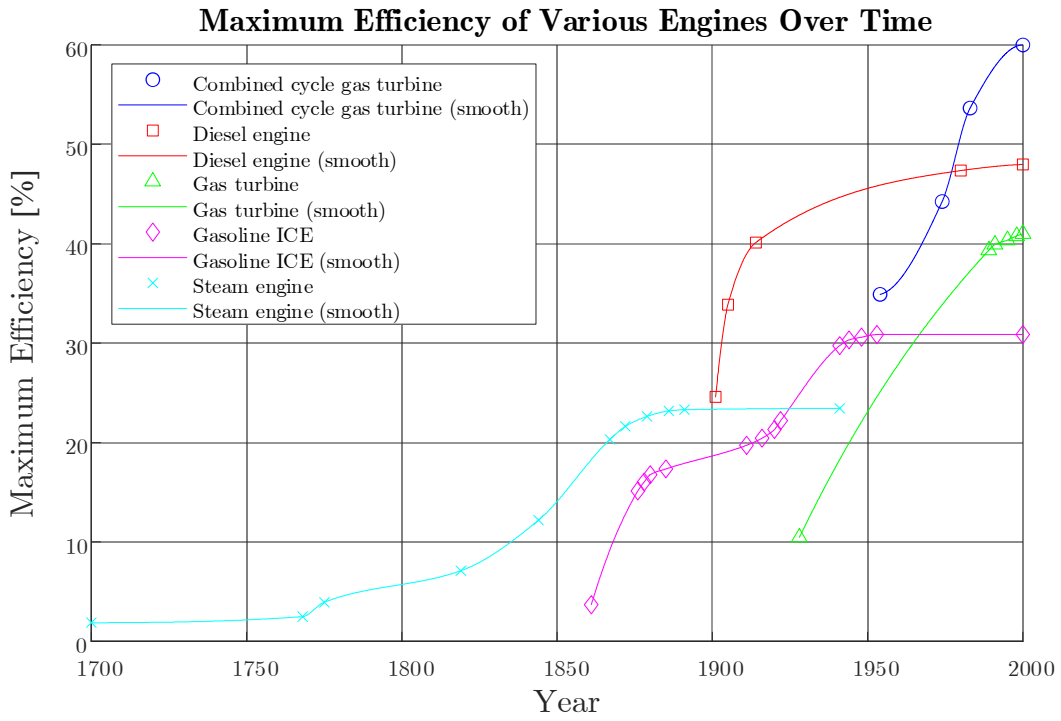

Figure 1-1 Maximum efficiencies of engines and turbines, 1700–2000 [1].

* ICE: internal combustion engine

of no more than 25% as shown in Figure 1-1 [1].

However, humanity did not stop there. In 1870, the Second Industrial Revolution began. Compared to the First Industrial Revolution, the forms of energy in society changed once again. In 1878, Joseph Wilson Swan patented the first incandescent light bulb, an event that marked the official entry of human society into the electrical age [2]. Compared to mechanical energy, electricity was safer and easier to control. Additionally, the ability to quickly transmit made electricity a primary energy source for human society, leading to its widespread adoption around the world.

Electricity, as an almost perfect "energy", has nearly revolutionized human society, providing power for various applications such as lighting, computing, and healthcare. However, there is a significant issue: controllable electricity for humans is not naturally occurring. Collecting natural electricity (like lightning) to power human needs is nearly impossible. Until recently, humans primarily generated electricity through combustion-based technologies, which are quite similar to steam engines. Therefore, although electricity appears very clean and efficient, this perception is largely due to focusing on the consumption of elec-

tricity while ignoring the inefficiencies of its generation. Furthermore, as previously mentioned, traditional fossil-fuel-based power generation methods still cannot avoid the "RCHPD" process. This is why, even though the Second Industrial Revolution greatly increased human productivity, “resources” have remained an unavoidable issue.

1.1.2 Resource Scarcity and Environmental Issues

As we mentioned above, “resources bring electricity, and electricity brings development.” It was published by China's National Energy Administration that the per capita residential electricity consumption in China increased from 500 kWh to 1000 kWh from 2013 to 2023 [3]; additionally, in 2023, China's total electricity demand reached 9224.1 TWh [4], accounting for approximately one-third of the world's total electricity demand (29471 TWh) [5]. It can clearly be seen, societal development reflects the substantial energy demand, as well as the corresponding resource demand. However, the distribution of resources on the earth is highly “unequal,” leading to constant conflicts and wars over resources [6][7][8]. According to the annual survey report [9], fossil fuel power plants remain the dominant energy source over the world until 2023. Resources used as fuel, such as coal, oil, and natural gas, are generally considered non-renewable; besides, they have other industrial values (such as chemicals and materials) beyond the use as energy sources. Therefore, it can be conducted that energy shortages are a foreseeable societal issue in near future.

In addition to thermal power generation, humans have experimented with other methods of producing electricity, such as nuclear power plants and hydroelectric stations [10][11]. These methods do not require large amounts of non-renewable resources; however, they pose significant potential environmental risks. For instance, the Fukushima Daiichi nuclear disaster in 2011 highlighted the severe consequences of nuclear power failures, resulting in massive radioactive contamination and long-term evacuations [12]. Similarly, the Chernobyl disaster in 1986 remains a stark reminder of the catastrophic risks associated with nuclear power, leading to widespread health and environmental impacts [14][15]. Furthermore, large hydroelectric projects like the Three Gorges Dam have been

associated with significant environmental and social impacts, including displacement, increased flood risks, and reduced biodiversity [15]. Another longstanding issue is global climate change [16][17]. Large amounts of greenhouse gases, particularly carbon dioxide, are being released into the atmosphere primarily due to the essential "combustion" process in thermal power generation. Climate change has caused significant economic losses and social disruption globally. Despite the rapid development of carbon capture and storage technologies that have somewhat mitigated the trend of climate change [18][19], reducing the reliance on thermal power plants remains central to addressing global warming.

Thus, even though the Second Industrial Revolution greatly improved human productivity, society now faces new challenges such as resource allocation and environmental degradation. The next energy revolution is urgently needed.

1.1.3 RES

In 1839 the photovoltaic effect was first observed; then in 1983, the world's first PV power station was built, with a capacity of 5.2 MW [20]. On the other hand, the 1973 oil crisis significantly forced the United States' government approach to the involvement of wind energy research and development. From 1973 to 1986, the commercial wind turbines market evolved from domestic and agricultural (1-25 kW) to utility interconnected wind farm applications (50-600 kW).

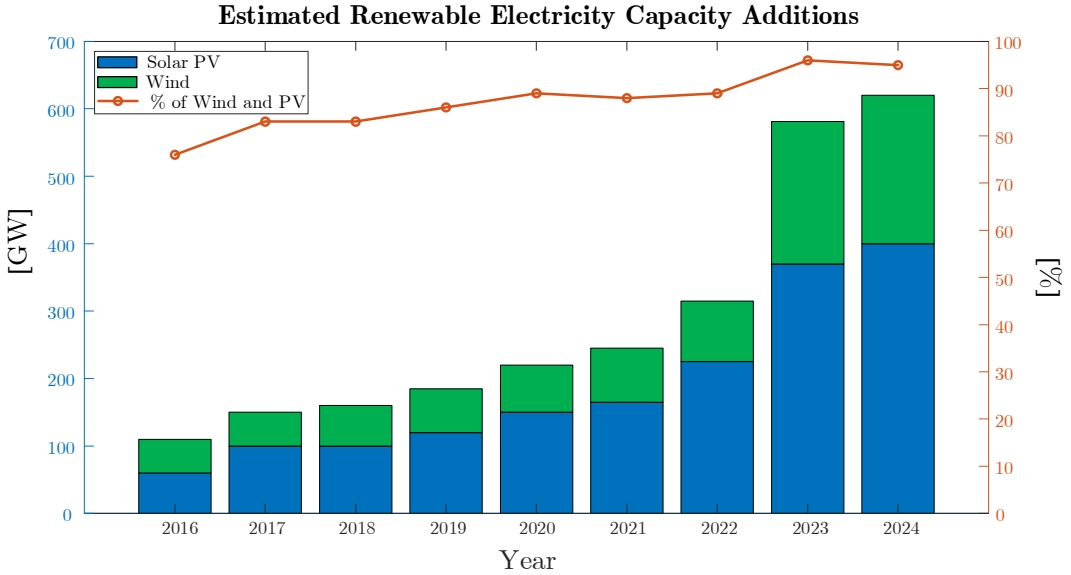

Figure 1-2 Estimated renewable electricity capacity addition per year [24].

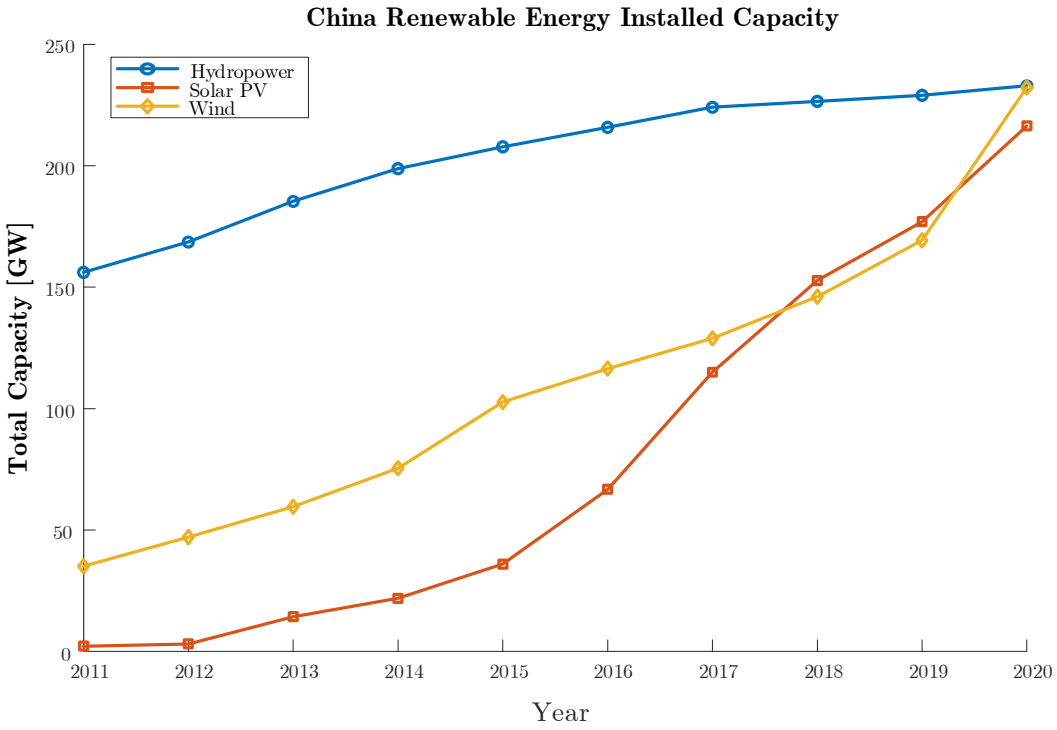

Figure 1-3 Totally Installed RES Capacity in China [28].

This period is considered a milestone in the history of wind energy [21]. These moments signal the potential for a new energy revolution.

Compared with the conventional fossil fuel power plants, wind and photovoltaic power generation processes are entirely different. Unlike the RCHPD process in thermal power plants, wind or photovoltaic power generation is a "resource"-"physical or chemical transformation"-"drive" process. Although the efficiency of this process is also not very high [22], it has the following advantages:

- There is no combustion process, so it does not produce any greenhouse or toxic gases, causing minimal environmental impact.
- The "resources" required for wind and photovoltaic power generation are not like those non-renewable fossil fuels but rather a form of "natural force". This "natural force" has vast reserves and does not belong to any person, country, or organization, thus avoiding conflicts and disputes. This can help prevent tragedies like the Gulf War, which was triggered by the competition for resources.

As we mentioned previously, although resources for hydroelectric and nuclear power are also renewable, they pose potential environmental and ecological

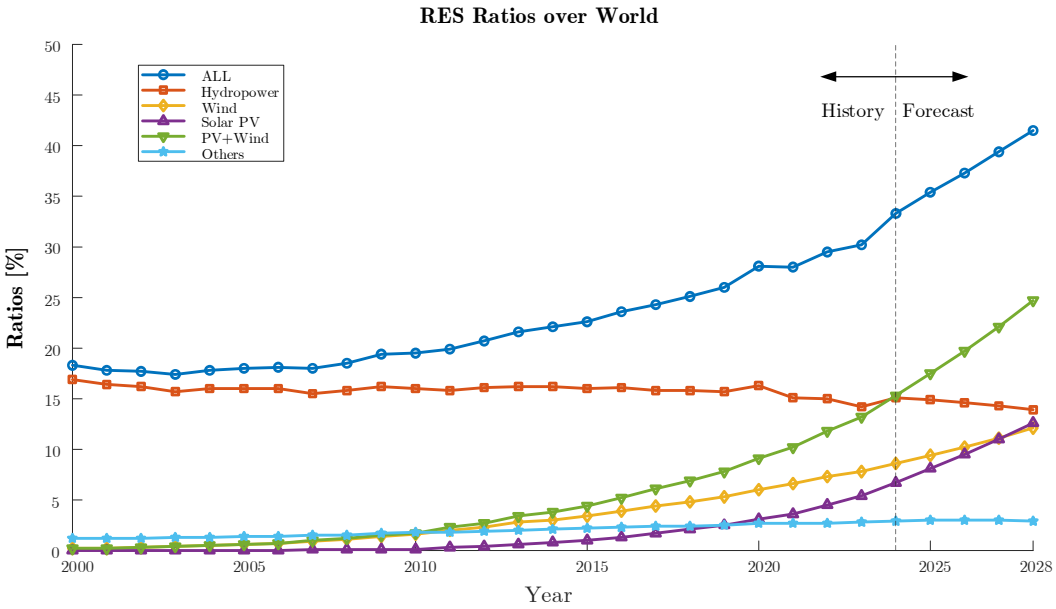

Figure 1-4 RES ratios over world [24].

hazards. Therefore, wind and photovoltaic power can be considered truly clean and green RES, as the most promising energy forms to lead the next societal revolution [23].

The discussion in this dissertation is mainly based on the RESs of PV and wind power. For convenience, RES indicates PV and wind power hereafter.

1.1.4 Power Grid Resilience and ESS

Since the 21th century, human society has increasingly focused on the development of PV and wind power. Especially after 2010, the installed capacity of RES in various countries has grown explosively. According to the statistics, by 2023, the newly installed RES capacity worldwide was approximately 507 GW, with PV and wind power accounting for about 95% of this capacity, as shown in Figure 1-2 [24] .

Due to the rapid development of photovoltaic and wind power, a significant amount of RES has been integrated into the grid. Globally, as of 2023, the world's total electricity generation was 30,000 TWh, with PV and wind power generating a total of 3935 TWh, accounting for 13.4% (3422 TWh, 11.9% in 2022) [5]. China's growth in this sector has been particularly remarkable. By 2023, China's total installed power generation capacity reached 3.01 TW [26], with solar and wind power contributing 1.1 TW [27], exceeding 33% of the total

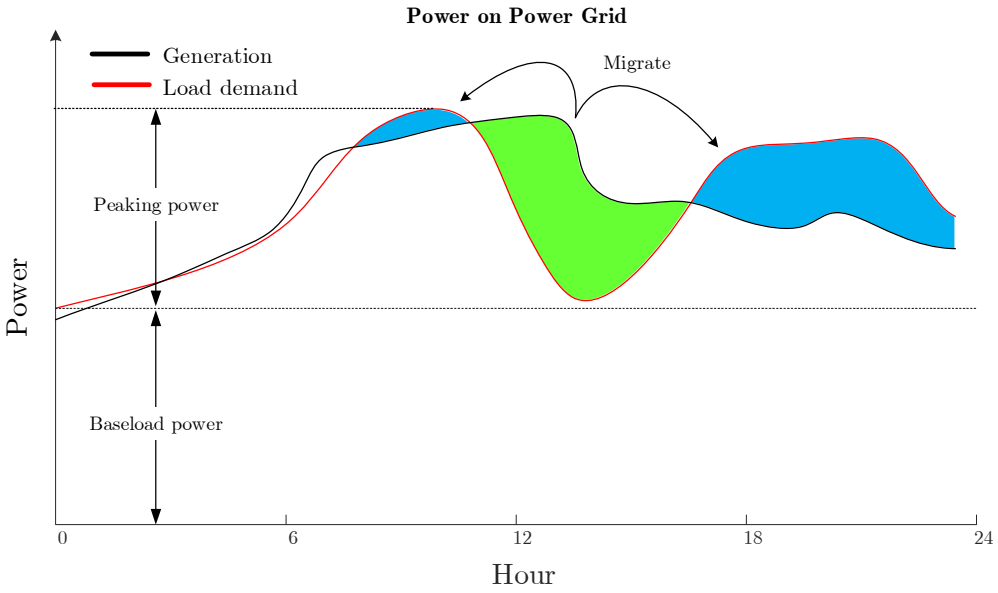

Figure 1-5 Electricity power curve during the day of a hypothetical city.

capacity. Figure 1-3, based on data released by the State Grid Corporation of China, shows the total installed capacity of the three energy forms in China [28]; Figure 1-4 shows the ratios of RES capacity over the world [24]. According to these data (historical and forecast), it is evident that not only China, but also the world is gradually moving away from environmentally harmful hydroelectric power and is committed to developing photovoltaic and wind power [29].

It is reasonable to believe that there will be more and more renewable energy sources (RES) installed and integrated into the grid in the future. However, the penetration of renewable energy resources (RES) is decreasing the resilience of current power grid due to their intermittent nature [30][31]. In addition, the growth of RES is decreasing the inertia of our power grid, because the RES is based on inverters instead of rotating generators [32][33][34]. Thus, the power grid could be unstable and uneconomic if no measures are taken.

“Why the power grid resilience is so important?” To explain it, the concepts of “baseload power” and “peaking power” are necessary. The power grid is a very special and fragile system that can only function properly when the input power (generation) equals the output power (load). Whether the input exceeds the output or vice versa, the power grid faces potential risks. However, the load on the grid is often not constant; it is a fluctuating curve [35]. The lowest point on this curve is known as "baseload power," representing the daily power demand of people's lives and the minimum power requirement of the grid. This curve

also has a peak power value, which is often much higher than the baseload power. Although peak power usually lasts for a short duration, the grid, as a balanced system, still needs to consider meeting this temporary demand. The power used to reach the peak is referred to as "peaking power.". Typically, baseload power is provided by more stable sources such as fossil fuels, nuclear, and hydropower, while peaking power is supplied by RES. Figure 1-5 shows the electricity power curve of a hypothetical city that heavily relies on PV during the day. As shown, from 0 AM to 8 AM, the load demand is low because most people are resting, keeping the system in a balanced state. From 8 AM to 11 AM, due to the morning rush, the electricity demand reaches peak, causing the grid to be in an overloaded state. From 11 AM to 5 PM, the demand decreases, and the grid experiences a surplus of electricity. After 5 PM, the second rush hour and increased recreational activities lead to another spike in demand, again putting the grid in an overloaded state. Since PV can only generate electricity during the daytime (8 AM to 5 PM), the power grid of this city experiences a significant surplus of electricity during the day and an overloaded state in the morning and evening, which is highly unhealthy.

For example, in Japan, in October 2018, some PV generation in the Kyushu region was required to stop by the power company due to excess generation [36]. Similarly, in June 2023, PV and wind power generation in the Kansai region were halted for the same reason [37]. However, in August 2023, in the Tokyo region, Tokyo Electric Power Company urged residents to conserve electricity [38]. According to its official website, Tokyo's reserve margin for peak load reached a low of only 6% twice in August 2023 [39].

Meanwhile in Taiwan, the government has clearly stated its policy of phasing out nuclear power and increasing the proportion of RES [40][41]. However, the 2021 blackout in Kaohsiung dealt a significant blow to society [42][43]. Although the Kaohsiung blackout might not be directly related to the cancellation of nuclear power, it could imply that baseload power requirements are not being met. Additionally, due to the instability of RES, it may not be able to compensate for any shortfall in baseload power promptly, leading to grid overloads. Therefore, if grid stability is not prioritized, incidents like the Kaohsiung blackout must occur again in the future (2022 Hsinta Power Plant outage [44]).

In summary, the large-scale integration of RES into the power grid can lead

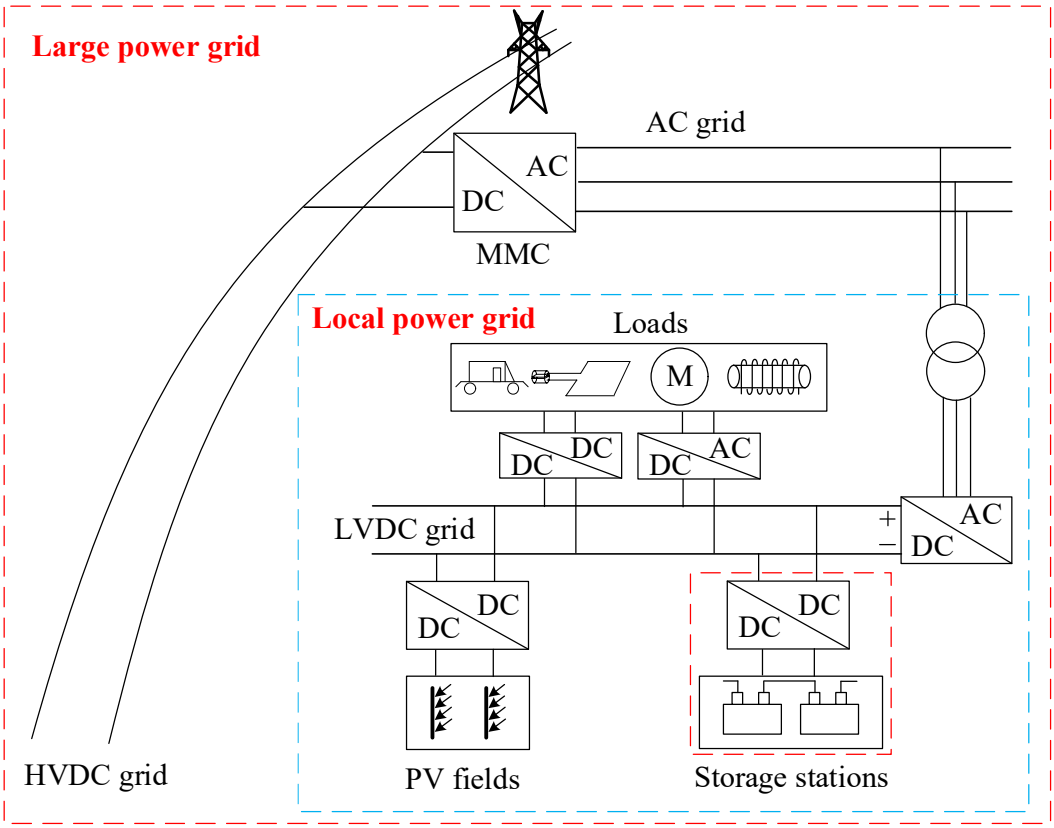

Figure 1-6 ESS in local power grid.

to several potential issues and risks:

- **Insufficient Power Generation at Night or During Calm Periods**: Since RES like solar and wind power depend on environmental conditions, solar power generation stops at night, and wind power can be unreliable during calm weather. This can lead to insufficient power generation and low electricity reserves, impacting the baseload power supply [45][46].
- **Overgeneration and Negative Electricity Prices**: During periods of high RES output, such as sunny or windy days, there can be an overproduction of electricity. This surplus can cause market prices to drop significantly, sometimes even turning negative [47].
- **Grid Stability and Reliability**: The intermittent nature and low inertia of RES can cause frequent fluctuations in the grid. This instability makes it challenging to maintain a consistent and reliable power supply, as RES cannot always respond quickly enough to changes in demand [48].

To address these issues, it is necessary to equip RES with corresponding

capacities of ESS [49][50][51][52]. Figure 1-5 shows a solution for that hypothetical city with ESS. By using ESS, excess electricity generated from 11 AM to 5 PM is stored to avoid low price and waste. Then, the stored electricity is released from 8 AM to 11 AM and from 5 PM to 12 PM. It is evident that integrating ESS and planning power reserves effectively can mitigate the potential risks posed by RES to the grid.

ESS typically involves a quantity of batteries that can convert electrical energy into chemical energy for storage. Moreover, recent research suggests that supercapacitors, which can directly store electrical energy, might become the next generation of energy storage media [53][54]. There have been numerous studies on ESS, all indicating that ESS can enhance grid stability and stabilize the electricity market [55]. The Chinese government has also introduced policies requiring that new RES installations must be equipped with ESS equivalent to 5%-20% of their capacity before they can be integrated into the grid [56]; there is another fact that the total installed ESS in China, until July, 2024, has been reported as 44.44 GW (99.06 GWh) [57]. Therefore, it can be said that a variety of centralized, distributed and equivalent ESS will continue increasing and play a crucial role in the future power grid [58]. This dissertation mainly focuses on issues of the battery-based ESS.

In this context, a high-performance power conversion system can increase the energy utilization and ensure the stored energy can be released correctly to rectify the fluctuation in power grids [59][60][61]. For example, an MMC for ESS was proposed in [61], which can simultaneously provide an active and reactive power compensation to the power grid, thereby improving the system resilience. As a result, it is evident that a high-performance power conversion system can effectively elevate the power grid stability. A high-performance power conversion system features:

- Efficient energy conversion;
- Rapid demand response;
- Excellent peaking shaving ability and stability;

on the other hand, a high-performance power conversion system can also facilitate the development and installation of ESS, consequently further enhancing the reliability and resilience of power grids integrated with a mount of RES.

1.2 Research Objectives: DC-DC for ESS in LVDC Grids

Figure 1-6 shows a schematic of a future power grid, which includes a large grid with HVDC transmission lines and AC transmission lines, as well as a local grid with LVDC distribution lines, PV fields, and local loads. In the local grid, ESS plays a critical role. It stabilizes the local LVDC grid and mitigates the impact on the larger grid during periods of insufficient PV generation or sudden increases in local load demand. Figure 1-7 depicts a microgrid, which can operate independently of the larger grid but can also connect to it when necessary. ESS is equally crucial in microgrids; it ensures stability during standalone operation and maintains power quality when integrated with the large grid.

Increasing research suggests that using DC as the electricity carrier for local grids and microgrids may be more advantageous [62][63][64][65]. Compared to AC, DC offers several benefits due to the absence of PLL and harmonic distortion issues. These advantages include the elimination of the skin effect, higher transmission efficiency, and greater flexibility in distributed power systems. In

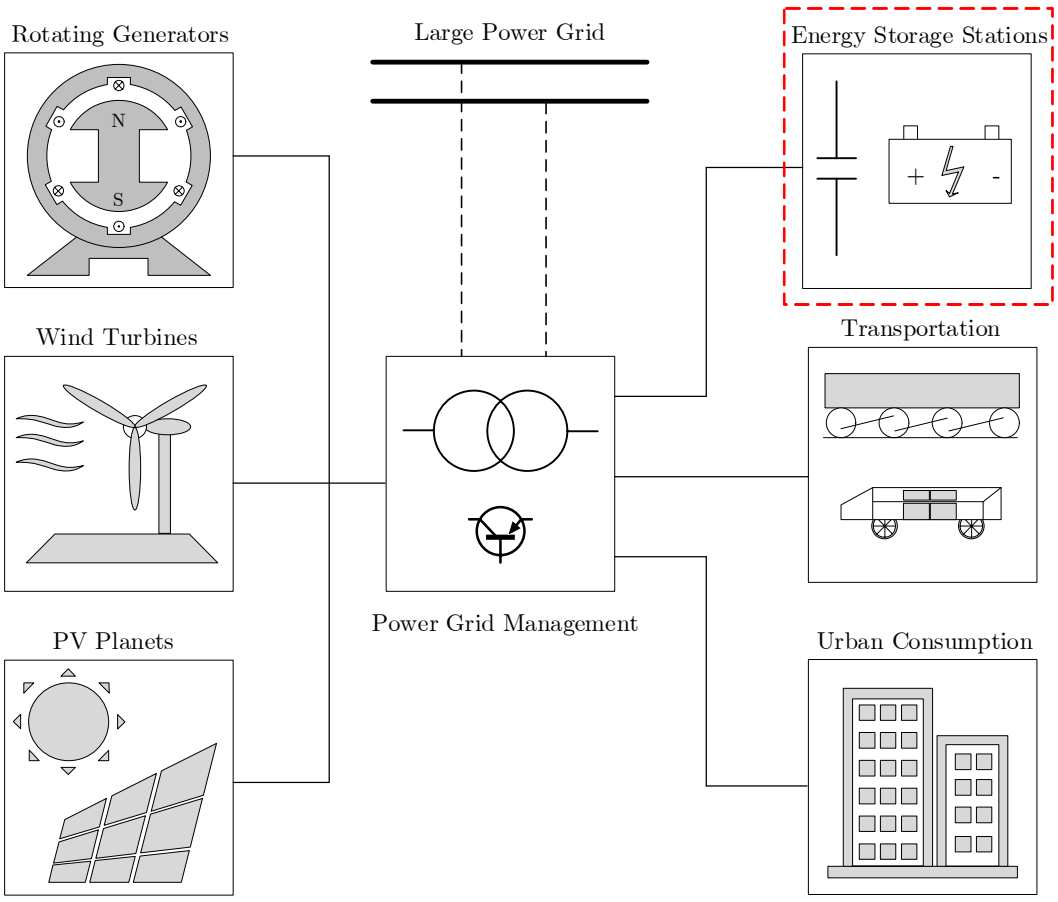

Figure 1-7 Microgrid.

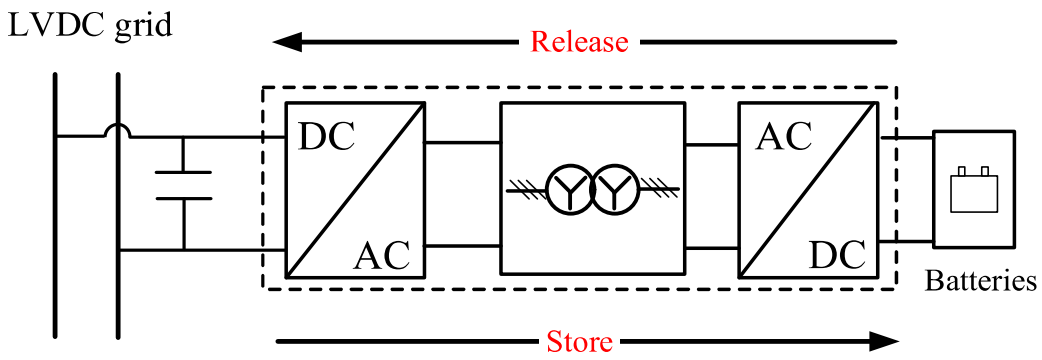

Figure 1-8 Bidirectional isolated DC-DC converter for ESS in LVDC grid.

fact, numerous studies indicate that DC might be more conducive to the integration of RES and the formation of distributed grids than AC [66][67][68][69][70]. Additionally, the voltage levels in local grids and microgrids are typically below several kilovolts, making the integration of ESS in LVDC grids a popular topic in recent years.

As previously mentioned, the primary focus of this dissertation is the DC-DC PCS for ESS in LVDC grids. Figure 1-8 illustrates a bidirectional isolated DC-DC converter used for ESS in a LVDC grid. This converter connects to the LVDC grid and storage batteries. When there is surplus power generation in the grid, this converter can store the electrical energy in the batteries. Conversely, when the load increases, this converter can release the stored energy from the batteries back into the grid. Besides, the converter shown in Figure 1-8 is a three-phase transformer-isolated bidirectional DC-DC converter, typically suitable for several-kilovolts hundreds-kilowatts ESS. This converter uses a transformer for galvanic isolation, ensuring the safety of both the energy storage station and the grid. Compared to single-phase structures, the three-phase structure offers greater capacity and compatibility. Moreover, increasing the capacity in LVDC grids is straightforward, as multiple units can be paralleled without the need for PLL synchronization.

Nowadays, various types of bidirectional DC-DC converters have been proposed and studied, each with their own advantages and disadvantages. Among them, the DAB converter is a widely used type of "Figure 1-8" converter, known for its simple structure, low cost, and high efficiency. However, the DAB converter also has some drawbacks, such as lower efficiency at light loads and when the voltage conversion ratio deviates from one.

The main work presented in this dissertation can be summarized as the

proposal of a new bidirectional isolated DC-DC converter improved from the DAB converter. This new converter retains the structure shown in Figure 1-8 and is suitable for ESS in LVDC grids, while can offer better performance under certain conditions compared to traditional DAB converters. Meanwhile, this dissertation provides the details of the proposed DC-DC converter, including its circuit topology, the structure of auxiliary converter, operating principles, the initial charge of the auxiliary converter, the improvement method using variable duty ratios, and the discussion of neutral point wire.

1.3 Outline of This Dissertation

The main body of this dissertation is divided into **Six Chapters**. The Chapters of the dissertation deal with the main ideas of the research efforts. A list of publications and reference bibliography follows the last Chapter.

Chapter 1 provides a background introduction for the entire dissertation. It reviews the history of energy, mainly focusing on the transitions from the First Industrial Revolution to the modern, highlighting the significant changes in energy forms. From a historical perspective, it is "electricity" that truly transformed societal structures and enabled significant progress. As human society advances, the demand for electricity continues to rise. Traditional power generation methods (fossil-fuel, nuclear, hydropower) consume resources or harm the environment, thus environmentally friendly RES such as PV and wind power are gaining importance. However, the integration of these RES into the power grid introduces potential risks, while installing more ESS helps stabilize the grid. This dissertation focuses on a new bidirectional isolated DC-DC converter designed for energy storage stations in local LVDC grids or microgrids.

Chapter 2 provides a literature review of bidirectional isolated DC-DC converters. The DAB converter is a well-known and widely used type of bidirectional isolated DC-DC converter. However, it has drawbacks such as high reactive power losses under light load and narrow range of voltage conversion ratio. This Chapter reviews the fundamentals of DAB converters and discusses the advantages and disadvantages of conventional DAB converters and resonant DAB converters. Then, it proposes a derived circuit based on the conventional DAB converter topology, using multilevel cascaded choppers to improve performance. Finally, the classification for the proposed cascaded converters DC-DC

converters is introduced.

Chapter 3 mainly focuses on the most basic cascaded converter - the cascaded choppers DC-DC converter with neutral point wire, called as NPW-CC DC-DC converter. This Chapter explains the main operating principles and equation derivations of the proposed CC DC-DC converter. Comprehensive comparisons between the conventional TP-DAB converter in terms of RMS current, peak current, and conversion efficiency are carried out. Finally, the NPW-CC DC-DC converter is experimentally validated by a 150 V, 2.5 kW prototype.

Chapter 4 addresses an issue in the NPW-CC DC-DC converter: zero-sequence current. This target is achieved by applying variable duty cycle in the converters. This method can theoretically make the zero-sequence current equal to zero, and subsequently further reduce the RMS and peak currents. This Chapter also includes experimental results for feasibility verifications and zero-sequence current reduction effect.

Chapter 5 discusses another issue of the NPW-CC DC-DC converter. This problem may cause overmodulation of the auxiliary converter, limiting the capacity and making the NPW-CC DC-DC impossible for high step-up applications. This Chapter carries out a detailed review for other types of cascaded-converters DC-DC converter that can overcome the overmodulation concern. The operating principles of the cascaded choppers DC-DC converter without neutral point wire (called NNPW-CC converter) are introduced in this Chapter. Furthermore, this Chapter also discusses the advantages and disadvantages between all types of cascaded-converters DC-DC converters.

Chapter 6 summarizes the entire dissertation. In addition, this Chapter gives a brief discussion of the issue of optimal switching frequency and outlines work directions for convenience in subsequent research.

Chapter 2 Literature Review

2.1 Isolated Bidirectional DC-DC Converters for ESS

The rapid expansion of RES and ESS has facilitated the development of power conversion systems with galvanic isolation, bidirectional power transmission, and large capacity. To establish connections between the dc grids and storage stations, DC-DC converters play a crucial role [71][72][73][74].

Isolated bidirectional DC-DC converters are increasingly important in the integration of ESS within future power grids [75][76]. These converters not only provide crucial galvanic isolation, ensuring safety and preventing electrical faults from propagating across different parts of the system, but they also enable bidirectional power flow, which is essential for dynamic energy management. In a grid that is becoming more reliant on RES, which are inherently variable, the ability to store energy when supply exceeds demand and to release it when demand is high is critical. Bidirectional DC-DC converters facilitate this process by allowing energy to flow both into and out of storage systems seamlessly. This capability ensures that ESS can respond quickly to fluctuations in energy supply and demand, contributing to grid stability. Furthermore, the flexibility offered by isolated converters in terms of voltage conversion and system integration is vital as the grid incorporates a wider range of energy sources and storage technologies. The converters' ability to maintain high efficiency and reliability, even when managing bidirectional power flow, makes them indispensable in ensuring that future grids can operate effectively and securely.

In summary, the combination of galvanic isolation, bidirectional energy flow management, and high efficiency positions isolated DC-DC converters as a cornerstone technology for the future of energy storage and grid management.

Figure 1-8 in the previous section illustrates a typical scheme of a bidirectional dc-dc power converter for ESS in LVDC grids, with galvanic isolation provided by a low/middle-frequency three-phase transformer. In general, both ends of a bidirectional DC-DC converter are power sources (or grids). The power

can be transmitted between the dc grids and the batteries according to real-time power generation and consumption requirements. In fact, many DC-DC converters incorporate a structure similar to that shown in Figure 1-8, e.g., bidirectional full-bridge converters, bidirectional flyback converters, and Cuk converters, etc. [77][78][79]. Among these, the DAB converter and its derived circuits are the most frequently mentioned types of bidirectional isolated converters. The following of this dissertation begins by discussing the advantages and disadvantages of the DAB converter and will then propose a new solution based on it.

2.2 DAB Converters

2.2.1 Single-Phase (SP) DAB Converters

The SP-DAB converter was first published on *IEEE* in 1991 [86], though it likely had been invented earlier. In fact, NASA had reported a 50 kW SP-DAB converter in 1989, achieving a relatively high power density of 0.2-0.3 kW/kg [87]. Nowadays, the SP-DAB converter is a widely researched and utilized DC-DC converter for EV, ESS, and grid applications, well known for its controllable output power, high efficiency, ZVS, high power density, bidirectional power transfer, and electrical isolation. Compared to traditional Buck/Boost choppers, the SP-DAB converter operates at a higher frequency and conducts power through pure AC current. As a result, the SP-DAB converter requires smaller inductance in its circuitry [88].

Figure 2-1 shows the typical circuit configuration of the SP-DAB converter, where IGBTs are used as power devices in it. As can be seen, the structure of the SP-DAB is very simple, consisting of only eight power switches, one inductor, and one transformer. Unlike other DC-DC converters, the SP-DAB converter generates current by controlling the voltage difference between the left and right bridge arms of the transformer. This voltage difference is typically achieved through phase-shift modulation or duty cycle modulation (or a combination modulation of both). Therefore, it is important to note that the SP-DAB converter supports various modulation methods, such as the well-known SPS modulation, DPS modulation, EPS modulation, TPS modulation, and other optimal

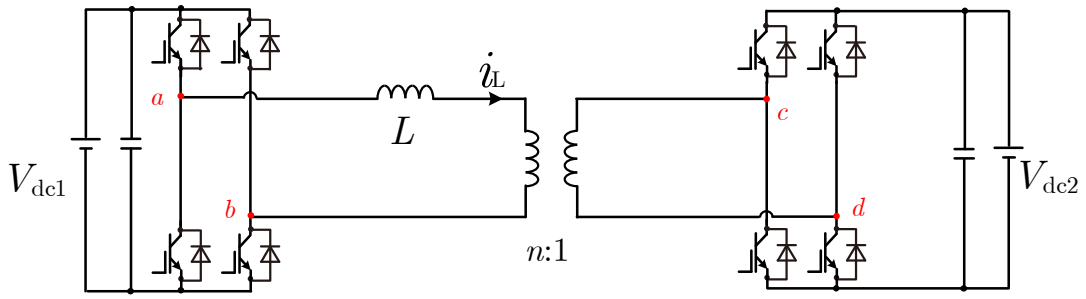

Figure 2-1 Conventional circuit configuration of SP-DAB converter (using IGBTs).

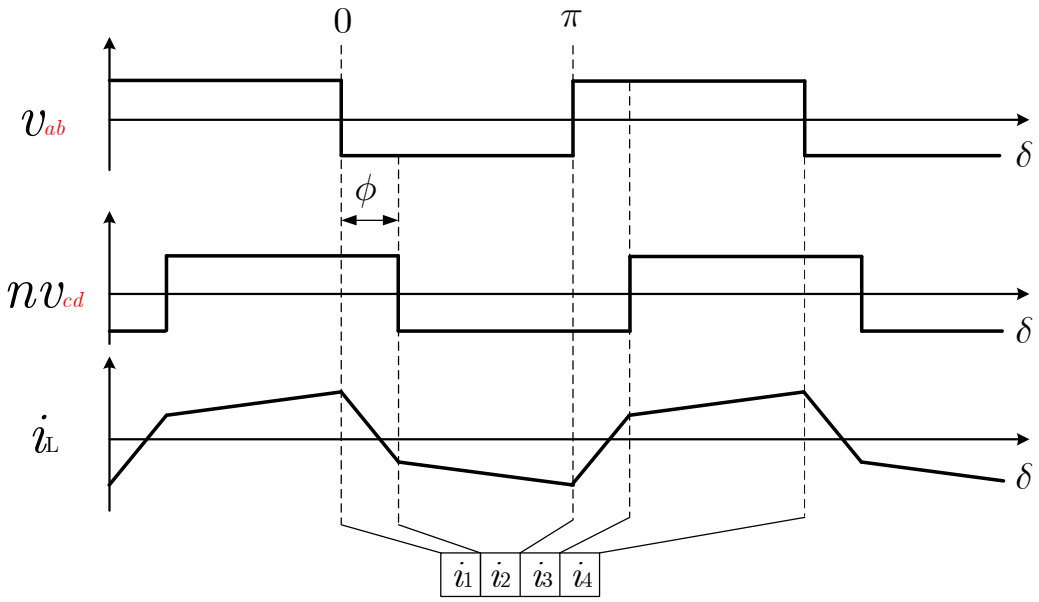

Figure 2-2 Key waveforms of conventional SP-DAB converter (using SPS), when $0 \leq \phi \leq \pi/2$.

modulation techniques. Figure 2-2 illustrates the key waveforms of the SP-DAB converter using SPS modulation. Obviously, it is evident that the SP-DAB converter generates current by creating a voltage across the inductor through phase shift. As discussed in the literature [79], the transferred power of the SP-DAB converter is positively correlated with the phase shift angle (ϕ). However, due to the phase shift (i.e., the voltage difference between the two sides of the transformer), the SP-DAB converter inevitably faces the following issues, regardless of the modulation method used:

- When the phase shift angle is small (light load conditions), the circuit can still generate currents (particularly when $V_{dc1} \neq n V_{dc2}$). However, the currents are mostly reactive (i.e., they do not contribute to power transfer).

- The circuit lacks compensation methods, making it difficult to avoid harmonic components.
- ZVS may not be achieved when $V_{dc1} \neq n V_{dc2}$ and when light-load, resulting in high switching power losses to the converter.

Although the above issues can be mitigated by using more complex modulation methods, they cannot be entirely resolved due to the inherent limitations of the SP-DAB circuit structure [80][81][82]. For example, DPS is a modulation method that utilizes two phase shift angles [80]. It can extend the ZVS range of the SP-DAB converter while reducing the peak current in the circuit. However, significant reactive current and harmonic components still persist in the circuit, which increases the RMS current and results in higher conduction losses. Furthermore, the introduction of additional parameters through complex modulation methods such as DPS and TPS can lead to degraded transient performance, increased peak values, biassed current, and potential saturation risks to the transformer [83][84][85]. These added complexities may cause instability or unexpected behavior (such as current and voltage spikes) in the converter, thereby posing concerns for the overall system.

*The Doctoral Student in Fujita Lab, **Kaiji Hazawa**, majors in the transient performance of SP-DAB converter using hybrid modulation. If you have any interest in it, please refer to his research documents.

2.2.2 Three-Phase (TP) DAB Converters

The TP-DAB converter was also first presented on *IEEE*, in 1991 [86]. In fact, it may have appeared possibly earlier than 1989 [89], but it is difficult to verify. The three-phase circuit topologies are adopted to meet the growing demands of renewable energy generation and ESS, owing to its higher power capacity and integration compared to the SP-DAB converter (3 times power with 12 power devices vs 1 time power with 8 power devices). The circuit topology of the conventional TP-DAB converter is shown in Figure 2-3, where only two TP bridges and one TP transformer are utilized. Over the years, there are a quantity of research regarding the TP-DAB converter have been done and published [90]-[104].

Although the TP-DAB converter and the SP-DAB converter have a similar

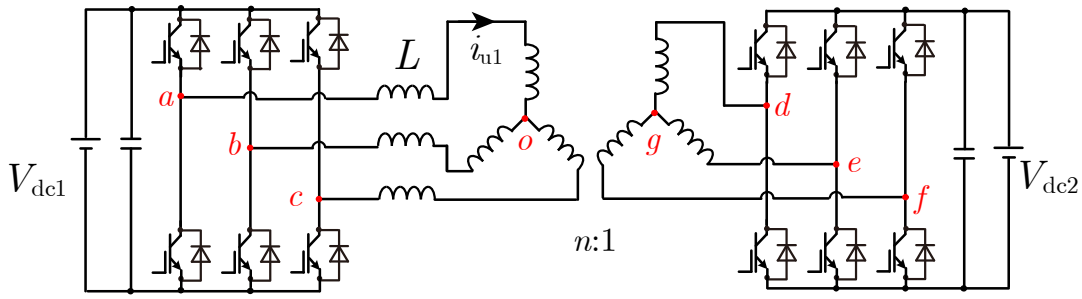

Figure 2-3 Conventional circuit configuration of TP-DAB converter (using IGBTs).

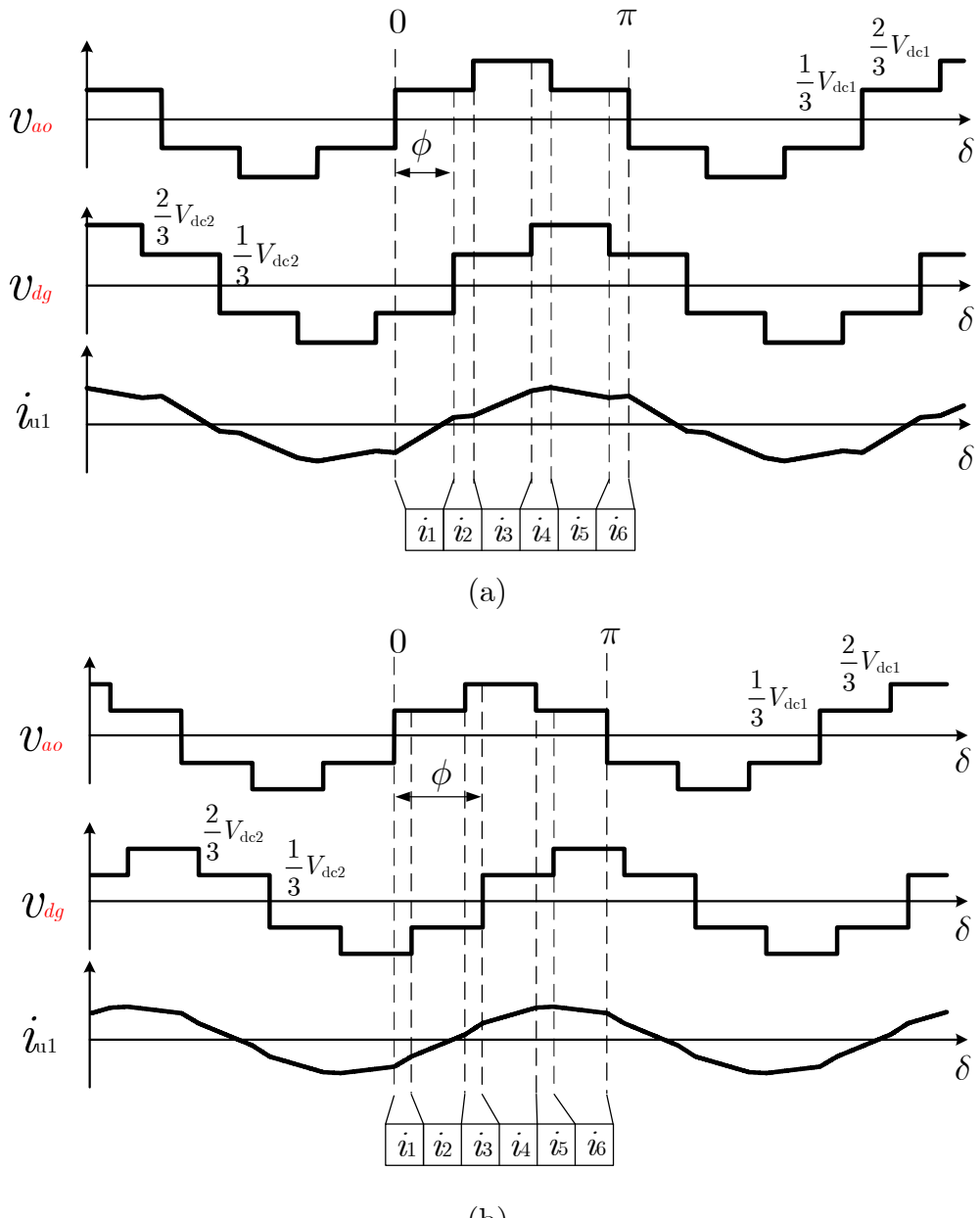

Figure 2-4 Key waveforms of conventional TP-DAB converter (using SPS) (a) when $0 \le \phi \le \pi/3$; (b) when $\pi/3 < \phi \le 2\pi/3$.

structure, they still differ in operating principles. Figure 2-4 illustrates the key waveforms of the TP-DAB converter using SPS modulation. Specifically, Figure 2-4 (a) shows the waveforms when $0 \leq \phi \leq \pi/3$, while Figure 2-4 (b) displays the waveforms when $\pi/3 < \phi \leq 2\pi/3$. Both SP-DAB converters and TP-DAB converters are attractive solutions for battery charge and grid interface applications [103][104]. Nevertheless, they have some differences as follows:

- TP-DAB converter has higher capacity and integration;
- TP-DAB converter does not have third harmonics, resulting in a current waveform closer to a sinusoidal shape;
- TP-DAB converter presents lower peak and RMS values, but only with SPS;
- TP-DAB converter has smaller voltage and current ripples [104];
- SP-DAB converter has wider ZVS range [104].

Furthermore, the SP-DAB has many multi-degree-of-freedom modulation and hybrid modulation, e.g., DPS and TPS, which may help improve the converter performance of SP-DAB converters. Despite, implementing these on the TP-DAB is more challenging due to its more complex structure. Although some scholars are still making attempts, e.g., literature [100] introduces a novel asymmetrical phase shifted square wave modulation and succeeds to extend the soft switching range when the transformer impedances are unbalanced. However, the modulation methods available for the TP-DAB are significantly fewer than those for the SP-DAB. Recent research indicates that SPS remains the most mainstream modulation method for TP-DAB converters [96][97][98][99].

In addition to the typical TP-DAB converter of Figure 2-3, lots of derived circuit and improved control methods based on the TP-DAB converter have been proposed and studied [91][100][101][102][103]. They provide a range of functionalities, such as higher voltage withstand capability, lower peak currents, or a wider ZVS range. For example, literature [102] mentions some circuits of the TP-DAB converter, derived from NPC converter, T-type converter, MMC, and etc., which can increase the voltage level and can widen the application range.

These enhancements make TP-DAB-based circuits versatile in addressing specific application requirements, further expanding their utility in different

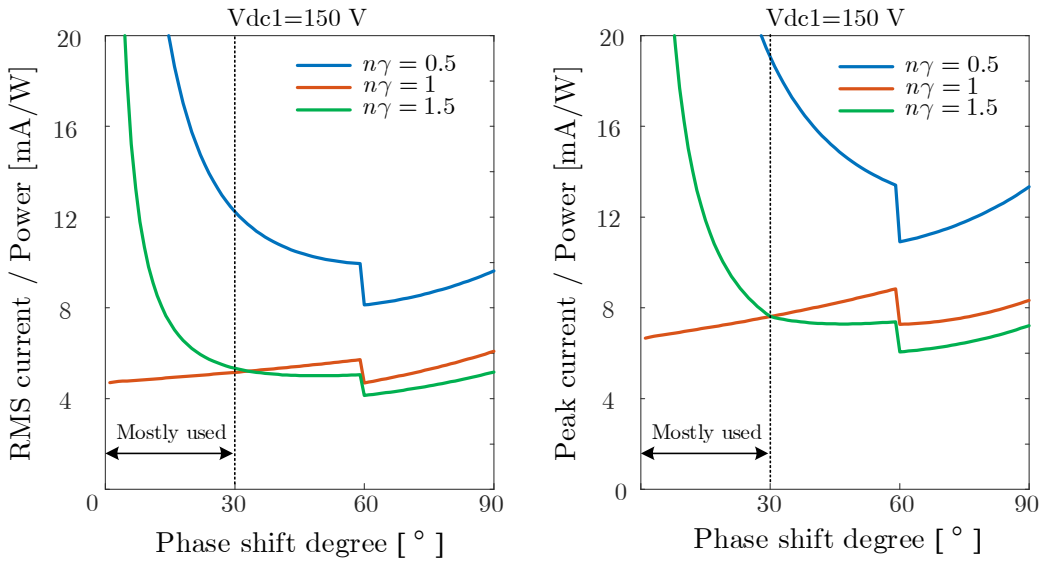

Figure 2-5 Normalized RMS and peak currents of TP-DAB converter for 1-W active power (using SPS), when $V_{dc1} = 150$ V.

power conversion scenarios. Nevertheless, the SP-DAB converter shown in Figure 2-2 and the TP-DAB converter shown in Figure 2-3, particularly those using SPS modulation, remain the dominant solutions in the field. In summary, for low-power, high-frequency, and highly integrated applications, the SP-DAB converter is clearly the better choice. On the other hand, the TP-DAB converter is more suitable for high-power, low-frequency, and long-duration applications. Additionally, due to the smaller voltage and current ripple in TP-DAB converters, they can help extend the lifespan of energy storage batteries. For systems that require high stability and long-term operation, the TP-DAB converter may also be the better option.

Due to the background of this dissertation is large-capacity grid-tied ESS, thus, the focus is on the TP-DAB converter.

2.2.3 Issues of Conventional DAB Converters

Despite the many advantages of DAB converters (including both SP-DAB converters and TP-DAB converters), no converter is without drawbacks. The DAB converter also faces several issues [105][106][107][108][109]. In this context, this dissertation primarily discusses and attempts to address a significant issue of the TP-DAB converter:

- when the voltage conversion ratio is not equal to one or when the phase

shift angle (ϕ) is relatively small (i.e., under light load), the TP-DAB converter requires very high currents to transmit power.

Figure 2-5 shows how much RMS and peak currents are needed for transmitting 1-W active power in a TP-DAB converter under different phase shift angle, when the DC input voltage is 150 V. The y-axis is normalized for eliminating the disturbance from parameters. When the voltage conversion ratio is equal to one, the TP-DAB converter needs low RMS and peak current for 1-W active power, just like well-known. However, when the voltage conversion ratio is not one, the TP-DAB converter needs a very high RMS and peak current to transmit 1, particularly under light-load condition. This limitation restricts the application range of the TP-DAB converter, and additional DC link circuits are often used at both ends of the TP-DAB to stabilize and regulate the voltage conversion ratio. This problem is caused by reactive and distortion power present in the circuit when the voltage conversion ratio is not one or under light load conditions. These factors increase the RMS and peak currents. To better understand the subsequent content, a brief introduction of the composition of AC power is provided here. Please note that all of this part is based on the IEEE standard [110].

Assuming the current and voltage can be represented by the following equations:

$$v = \sum_{k=0} v_{kf_r} \ , \tag{2.1}$$

$$i = \sum_{g=0} i_{gf_r} \ , \tag{2.2}$$

where v_{f_r} and i_{f_r} represent the fundamental components; v_0 and i_0 (when k=0, g=0) represents the DC components; rest of v_{kf_r} and i_{gf_r} (when k≠0, g≠0) represent the harmonic components.

Typically, AC power (apparent power) consists of three components: active power, reactive power, and distortion power. Their fundamental relationship is as follows:

$$S^2 = \sum P_{kg}^2 + \sum Q_{kg}^2 + \sum D_{kg}^2 \ . \tag{2.3}$$

In (2.3), S indicates the total apparent power; P_{kg} indicates the active power caused by k^{th} voltage and g^{th} current; Q_{kg} indicates the reactive power caused by k^{th} voltage and g^{th} current; D_{kg} indicates the distortion power caused by k^{th} voltage and g^{th} current.

Apparent power is determined by the product of RMS values of v and i:

$$S = v_{RMS} \times i_{RMS}\,, \tag{2.4}$$

Active power is solely determined by the load (no loss considered), representing the total power consumed. The equation for active power is:

$$P = \sum_{\substack{k=0\\g=0\\k=g}} P_{kg} = \sum_{\substack{k=0\\g=0\\k=g}} \int v_{kf_r} i_{gf_r} dt\,, \tag{2.5}$$

When $k \neq g$, the corresponding integral term must be equal to zero. Thus, only same-frequency components (including DC) can produce active power. There is another representation of active power using RMS values as

$$P = \sum_{\substack{k=0\\g=0\\k=g}} P_{kg} = v_{0,RMS} \times i_{0,RMS} + \sum_{\substack{k=1\\g=1\\k=g}} v_{kf_r,RMS} \times i_{gf_r,RMS} \times \cos\sigma_k\,, \tag{2.6}$$

where σ_k is the corresponding phase difference between the same-frequency components of v_{kf_r} and i_{gf_r}.

Reactive power represents the energy exchange of same-frequency components within various energy storage elements in the system. Reactive power does not flow to the load. Reactive power cannot be expressed by integral, and the equation is:

$$Q = \sum_{\substack{k=1\\g=1\\k=g}} Q_{kg} = \sum_{\substack{k=1\\g=1\\k=g}} v_{kf_r,RMS} \times i_{gf_r,RMS} \times \sin\sigma_k\,. \tag{2.7}$$

Distortion power represents the energy exchange of different-frequency components within various energy storage elements in the system. Distortion power does not flow to the load. Distortion power cannot also be expressed by integral, and the equation is:

$$D_{kg|k\neq g} = v_{kf_r,RMS} \times i_{gf_r,RMS}\,. \tag{2.8}$$

In the *IEEE* standard, the non-active power N is used to denote the sum of reactive power and distortion power, which is given by

$$N = \sqrt{S^2 - \sum P^2} = \sqrt{\sum Q^2 + \sum D^2}\,. \tag{2.9}$$

In (2.6), $\cos\sigma_k$ represents the power factor (PF), which indicates the proportion of active power at a specific frequency. The power factor for the fundamental components $\cos\sigma_1$ is defined as the fundamental power factor (or displacement power factor), which is given by

$$\mathrm{PF}_1 = \cos\sigma_1 = \frac{P_1}{S_1} = \frac{\dfrac{1}{T_{s1}}\int v_{fr} i_{fr} dt}{v_{fr,RMS} \times i_{fr,RMS}}\,. \tag{2.10}$$

Additionally, the total power factor (PF_{ot}) is used to reflect the total effective

work of the system. the total power factor is given by

$$\mathrm{PF}_{ot} = \frac{P}{S} = \frac{P}{\sqrt{\sum {P_{kg}}^2 + \sum {Q_{kg}}^2 + \sum {D_{kg}}^2}}. \tag{2.11}$$

Generally, a higher PF_{ot} indicates better system performance. However, this is not absolute. In power electronics technology, some control may intentionally reduce the total power factor to achieve other objectives, such as injecting harmonics to reduce peak current.

2.2.4 Resonant DAB Converters

As previously mentioned, the performance of DAB converters is notably poor under light load conditions due to harmonics and reactive power losses. As mentioned previously, numerous studies have attempted to address the issues of DAB converters. For instance, circuit resonance is a commonly used technique to eliminate harmonics and improve the power factor. Additionally, the resonant circuit introduces a new degree of control-frequency, which significantly increases the flexibility of the converter. Furthermore, resonant DAB converters typically have a wider ZVS range.

Many studies have applied circuit resonance to SP-DAB [111][112][113][114][115][116] converters, as well as to TP-DAB converters [117][118][119][120]. The performance of resonant converters is mostly determined by the structure of the resonant tank. Nowadays, resonant technology has become quite advanced and various composite resonant circuits have been developed and researched, such as *LLC*, *LCCL*, *CLLC*, and Dual-*LCC* configurations. By adding a proper resonant circuit to the DAB converter, the converter can achieve minimal RMS current (approaching a sinusoidal waveform), thereby reducing conduction losses. For example, literature [117] mentioned a *LCL* TP-DAB converter, which can significantly decrease the conduction loss and increase the conversion efficiency, especially under higher conversion ratio. Similarly, literature [120] firstly introduces a tank-reconfigurable resonant TP-DAB converter. It can operate either as a TP-DAB resonant immittance converter [119] or a TP-DAB series resonant converter. This characteristic allows the converter to have wider ZVS range and lower conduction loss.

Although resonant DAB converters can improve the performance of conventional DAB converters to some extent, they still face some challenges. First, because the inductors (L) and capacitors (C) of the resonant circuit are passive components, power regulation may be difficult. The traditional approach is to adjust the duty cycle or phase shift. However, adjusting the duty cycle can increase circulating current, leading to higher losses. Similarly, phase shift inevitably results in low power factors on the primary and secondary sides. Moreover, resonant converters are highly sensitive to frequency, requiring careful consideration of the switching frequency, quality factor of resonant circuit, and higher-order harmonic components during the design stage. As a result, the design process for resonant converters is more complex compared to traditional converters.

2.3 Requirements of Wider Voltage Conversion Ratio Range and Higher Overall Efficiency

The previous sections introduced a typical bidirectional isolated DC-DC converter: the TP-DAB converter. Its basic principles, advantages and disadvantages, and some of its derivative circuits were also discussed. However, the TP-DAB converter has certain limitations, which restrict its application in ESS. As previously mentioned, neither the TP-DAB converter nor its derivative circuits can perfectly solve the issues of low efficiency under light loads and a narrow voltage conversion range. Generally, TP-DAB converters are often paired with controllable AC-DC converters or DC link circuits and specific transformers with matching turns ratios, so that the circuit operates under ideal conditions (i.e., the product of voltage conversion ratio and windings turns ratio is equal to one). However, such configurations also increase costs and reduce flexibility.

Without the assistance of a DC link or other controllable circuits, the TP-DAB converter suffers from increased losses. However, voltage fluctuations are commonly encountered. For instance, the voltage in battery-based ESS is not stable. Currently, two types of batteries—lithium-ion and lithium iron phosphate, are most likely to be used in ESS. The voltage of these batteries varies with the SoC. According to literature [122], the voltage of a nominal 3.7 V

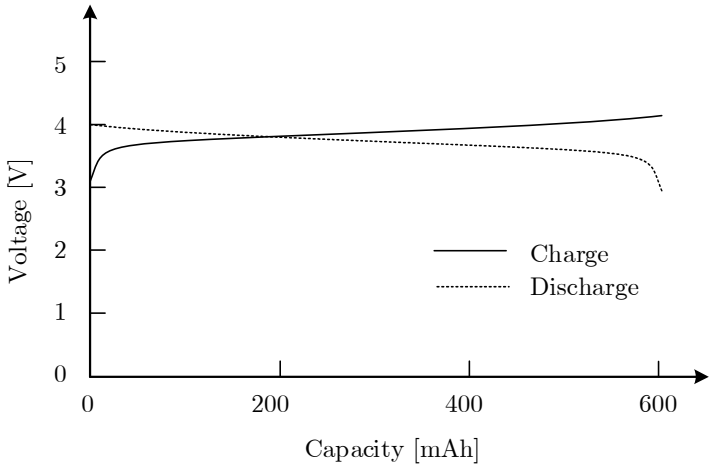

Figure 2-6 Q-V characteristic of a specific lithium-ion battery [122].

lithium-ion battery can range from 3 V to 4 V depending on the SoC (–19% to +8%) as shown in Figure 2-6. Literature [123] indicates that the voltage of a nominal 3.2V lithium iron phosphate battery can range from 2.5 V to 3.5 V depending on the SoC (–22% to +9%).

Moreover, besides SoC affecting battery voltage, battery aging also impacts battery pack voltage. Literature [124] compares the voltage curves of degraded and new batteries, showing that the voltage range of a nominal 3.7 V lithium-ion battery changed from (2.7 – 4.2 V) to (3.1 – 4.2 V) due to degradation, demonstrating that battery aging widens the voltage fluctuation range.

In addition to battery pack voltage fluctuations, the grid voltage is also not a stable value. For example, onboard energy storage systems for trains [125] often face voltage fluctuations on both the battery and grid sides. Literature [126] discusses the voltage fluctuation of the 1.5 kV DC grid used in Japan's railways, which typically ranges from 870 V to 1780 V, and describes a flywheel compensation device that stabilizes grid voltage to (1130 V to 1700 V). Similarly, other studies, such as [127], present an energy storage system that uses regenerative power to improve railway grid voltage, applied to the tram system in Kagoshima of Japan. This tram system operates on a 600 V DC grid, with grid voltage fluctuating between 360 V and 750 V. The energy storage system uses nominal 302 V lithium-ion batteries, with voltage fluctuations between 244 V and 344 V.

There are also other reasons causing unstable voltage in DC grids. For example, the output voltage of PV systems is not constant. Additionally, since PV systems require MPPT control to ensure maximum power output, the voltage

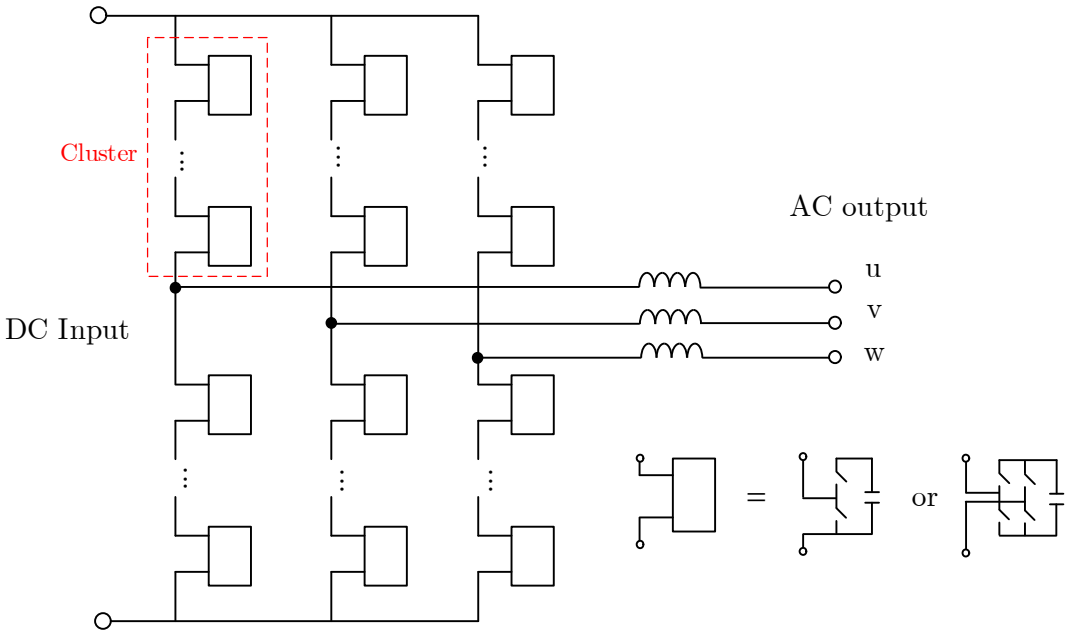

Figure 2-7 A kind of MMC (DC-AC) and cascaded converters.

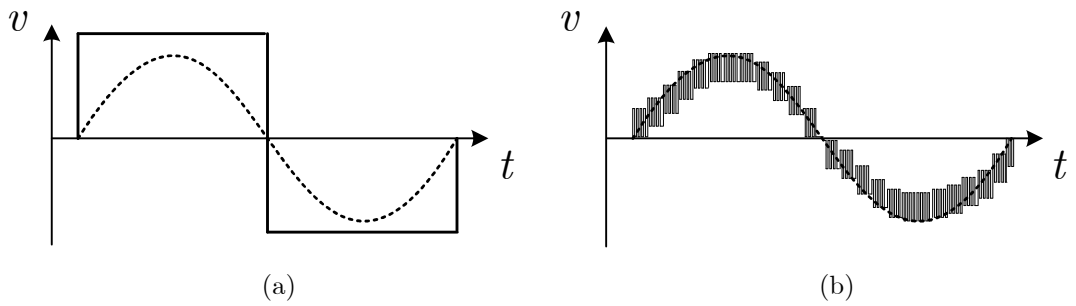

Figure 2-8 Voltage waveforms of (a) conventional two-level inverter, and (b) MMC.

they supply to the grid is typically influenced by the load size and solar irradiance. By applying MPPT, the output voltage of a commercially available single PV cell is 0.5 – 0.6 V (some high-voltage PV cell may be 0.5 – 0.7 V [128]), which causes the voltage of the DC grid (or the DC bus) to vary. This effect is particularly evident in small-capacity microgrids.

It can be concluded that converters designed for battery-based ESS may face significant voltage ratio fluctuations. Besides, since battery charging and discharging are prolonged processes (not completed instantly or in a short time), the overall efficiency of the converter across a range of loads (from light to heavy) is also a critical performance index. Therefore, without the support of additional controllable circuits, e.g., DC links mentioned previously, the conventional TP-DAB converter is highly sensitive to voltage fluctuations. This sensitivity potentially reduces its overall efficiency, making it challenging for the TP-DAB converter to be suitable for battery-based ESS applications.

2.4 MMC and Cascaded Converters

MMC is a kind of power converter using cascaded converters, firstly reported in 1995 and published in 1997 on *IEEE* [129][130]. The MMC has since become a significant innovation in power electronics [131][132], particularly in HVDC transmission systems and medium-voltage drives due to its modularity, scalability, and high efficiency.

Figure 2-7 shows a kind of typical MMC (DC-AC). In general, MMC employs plural half bridge converters (choppers) or full bridge converters as "unit converters". These cells are cascaded into a "cluster" like shown in Figure 2-7, where all of them can be controlled independently [133]. The cluster allows MMC to generate a multilevel voltage. In addition, the MMC can obtain a higher equivalent operational frequency by applying phase-shifted PWM to each cell of the cluster, subsequently obtaining better control performance and reducing the harmonics. Figure 2-8 (a) and (b) show the output voltage waveforms of a conventional two-level inverter and an MMC, respectively. It can be seen that, obviously, the MMC outputs a voltage waveform that has lower high-frequency harmonic components and is closer to a pure sinusoidal. MMC technology has been widely applied to various applications to improve system performance. For instance, STATCOM is a classic example of an MMC [134][135][136]. It is commonly used to connect to the power grid to improve power quality by providing reactive power compensation and harmonic mitigation.

As mentioned previously, MMCs possess the capability for multi-level output and high-frequency operation. This capability is achieved by connecting multiple unit converters in series. Consequently, some applications use these "clusters" separately in the circuit rather than constructing a complete MMC [125][137][138][139]. These clusters are also called cascaded converters. By integrating cascaded converters as auxiliary converters, circuit performance aspects of the main converter can be improved. Besides, since these cascaded converters are active components, this approach offers greater flexibility and controllability compared to those passive methods like resonance. For instance, literature [137] proposes a three-phase DC-AC converter using cascaded choppers for PV grid connection. This converter provides benefits such as low harmonics, reduced

RMS and peak currents, and partial ZCS. Similarly, literature [138] introduces a DC-DC converter for onboard battery applications that significantly reduces current ripple using cascaded choppers. Following the research work of [138], literature [125] replaces the cascaded choppers with a single full-bridge converter, further reducing cost and losses. Additionally, literature [139] discusses the possibility of applying different voltage levels to cascaded choppers, which decreases power losses but reduces the output voltage range.

2.5 Conclusion

2.5.1 Cascaded-Converters DC-DC Converters

The previous sections have outlined the development history and operating principles of the TP-DAB converter, as well as its issues. Meanwhile, the conventional TP-DAB converter is difficult to meet those requirements of ESS (e.g., the TP-DAB converter presents high RMS and peak currents under light load condition, while it presents low conversion efficiency when battery voltage or grid voltage changes). To address these issues, the resonant TP-DAB converter, which utilizes passive components, was proposed. Compared to conventional TP-DAB converters, resonant TP-DAB converters feature lower harmonic distortion, leading to reduced RMS and peak currents. However, resonant TP-DAB converters still rely on phase-shift control, which means a definite reactive power on the primary and secondary sides, consequently causing reactive power losses on at least one side of the converter. Additionally, resonant TP-DAB converters are highly sensitive to circuit parameters such as switching frequency and quality factor, making converter design more complex.

To overcome the aforementioned challenges, this dissertation proposes a novel DC-DC converter suitable for ESS in DC grids, utilizing cascaded converters. Figure 2-9 illustrates the circuit scheme of this new converter, which combines the TP-DAB converter with cascaded converters. This novel converter aims to leverage the high-frequency and multilevel output characteristics of cascaded converters to improve the circuit performance, especially in terms of the power factor and conversion efficiency under light-load conditions. This circuit has the advantage of being fully controllable without requiring phase shift to

control output power. Additionally, this converter presents lower RMS and peak currents compared with the TP-DAB converter, particularly when the voltage conversion ratio is non-one. This novel converter is envisioned for several-kilo-volts-hundreds-kilowatts ESS applications.

2.5.2 Classification of Cascaded-Converters DC-DC Converters

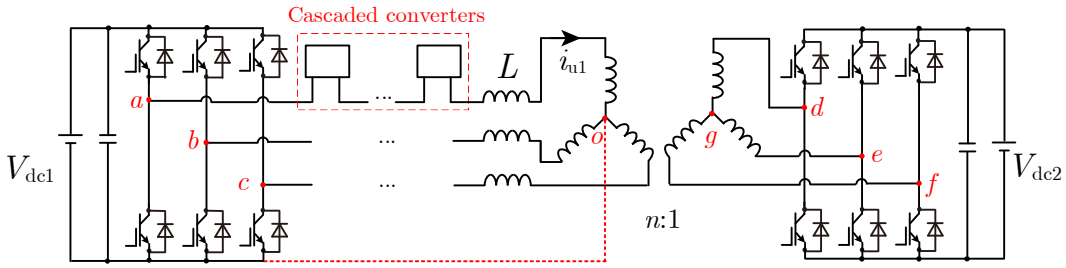

Figure 2-9 Novel DC-DC converter combined with DAB converter and cascaded converters.

The cascaded-converters DC-DC converters can be classified with four combinations according to the type of cascaded converters and the neutral point wire in the primary side.

①. Using cascaded choppers and having neutral point wire;

②. Using cascaded full-bridges and having neutral point wire;

③. Using cascaded choppers and not having neutral point wire;

④. Using cascaded full-bridges and not having neutral point wire.

Each type of cascaded-converters DC-DC converter has unique characteristics. For convenience, abbreviations are used in this dissertation to represent the four combinations as follows:

⑤. NPW-CC type ;

⑥. NPW-CF type;

⑦. NNPW-CC type;

⑧. NNPW-CF type.

The naming convention is an acronym, for example, the neutral point wire type cascaded choppers DC-DC converter is abbreviated as NPW-CC DC-DC converter. Terms of ①–④ correspond to terms of ⑤–⑧ in order, respectively. Among the four combinations, the term of ① (or term ⑤) is referred to the most basic type and it is also the main research object of this dissertation. Chapter 3 and Chapter 4 will focus on the NPW-CC DC-DC converter. However,

the NPW-CC DC-DC converter has one significant issue, which will be discussed in Chapter 5 and other types of cascaded-converters DC-DC converters will be also compared in Chapter 5.

Chapter 3 NPW-CC DC-DC Converter

3.1 Circuit Topology

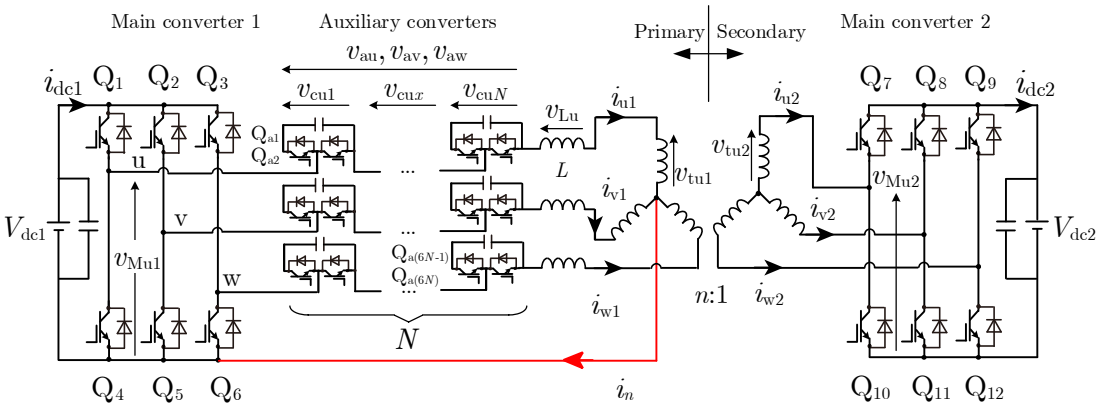

Figure 3-1 Circuit configuration of the NPW-CC DC-DC converter with a Yn-Y transformer (using IGBTs).

The circuit configuration of the proposed DC-DC converter using IGBTs as power devices is shown in Figure 3-1. The converter is isolated by a three-phase three-limb Yn-Y transformer with a voltage ratio of n. For convenience, the left part of the converter is hereafter defined as the primary side while the right part of the converter is defined as the secondary side. A three-limb core is employed in the transformer, where a zero-sequence current is allowed to flow in the primary windings of the transformer. However, the zero-sequence current produces little effect on the flux inside the core because the three-limb core exhibits infinite magnetic resistance for the zero-sequence current ideally [143].

There are two three-phase full bridges configured in the primary and secondary sides of the circuit to connect to the DC power source; the main converter 1 (Q_1–Q_6) and the main converter 2 (Q_7–Q_{12}). In Figure 3-1, the auxiliary converter comprises multiple cascaded bidirectional choppers, which are series-connected between each phase of the main converter 1 and the corresponding windings of the transformer. N is the quantity of the cascaded choppers of the auxiliary converter in each phase. While the subsequent explanation presumes $N = 3$, the operating principles and control methods remain applicable to cases

involving any cascade quantity. Although some research have attempted to reduce the number of cascaded converters [125][142], this dissertation does not discuss the optimal quantity of cascaded converters. Inductance L indicates the total inductance for each phase in the primary side, including leakage inductance of the transformer and series-connected inductor.

In this dissertation, the converter shown in Figure 3-1, which uses cascaded bidirectional choppers, will be referred to as the CC DC-DC converter. Similarly, converters using cascaded full-bridge inverters will be referred to as CFB DC-DC converters. Besides, since this converter has a neutral point, to differentiate it from converters without a neutral point (which will be discussed later), this type of converter is referred to as the NPW type converter, while the converter without a neutral point is referred to as the NNPW type converter. Based on the above naming convention, different converters can be distinguished. For example, the converter shown in Figure 3-1 can be referred to as the NPW-CC DC-DC converter.

3.2 Operating Principles and Equations

Operations in Main Converters

The switching frequency of the main converters is f_{s1}, and all the power devices operate with a fixed duty ratio of 0.5. In addition, each power device of the main converter 1 operates synchronously with the corresponding power device of the main converter 2. Specifically, the following relationship holds in the logic signals of the u-phase power devices:

$$\begin{cases} S_{Q1} = S_{Q7} = \overline{S}_{Q4} = \overline{S}_{Q10} = 1 \ (0 \le t < 0.5T_{s1}) \\ S_{Q1} = S_{Q7} = \overline{S}_{Q4} = \overline{S}_{Q10} = 0 \ (0.5T_{s1} \le t < T_{s1}), \end{cases} \tag{3.1}$$

where T_{s1} is the switching period of the main converters, while S_{Q1}, S_{Q4}, S_{Q7} and S_{Q10} denote the gate logic signals of Q_1, Q_4, Q_7 and Q_{10}, respectively. The power devices of the main converters in v-phase (Q_2, Q_5, Q_8 and Q_{11}) and w-phase (Q_3, Q_6, Q_9 and Q_{12}) follow the similar logics, while a phase difference of 120° exists in each phase. Since u, v, and w phases adopt identical control strategies, only u-phase circuit is adequate to explain the operating principles (only u-phase will be discussed in follows).

It is worth noting that the NPW-CC DC-DC converter does not require

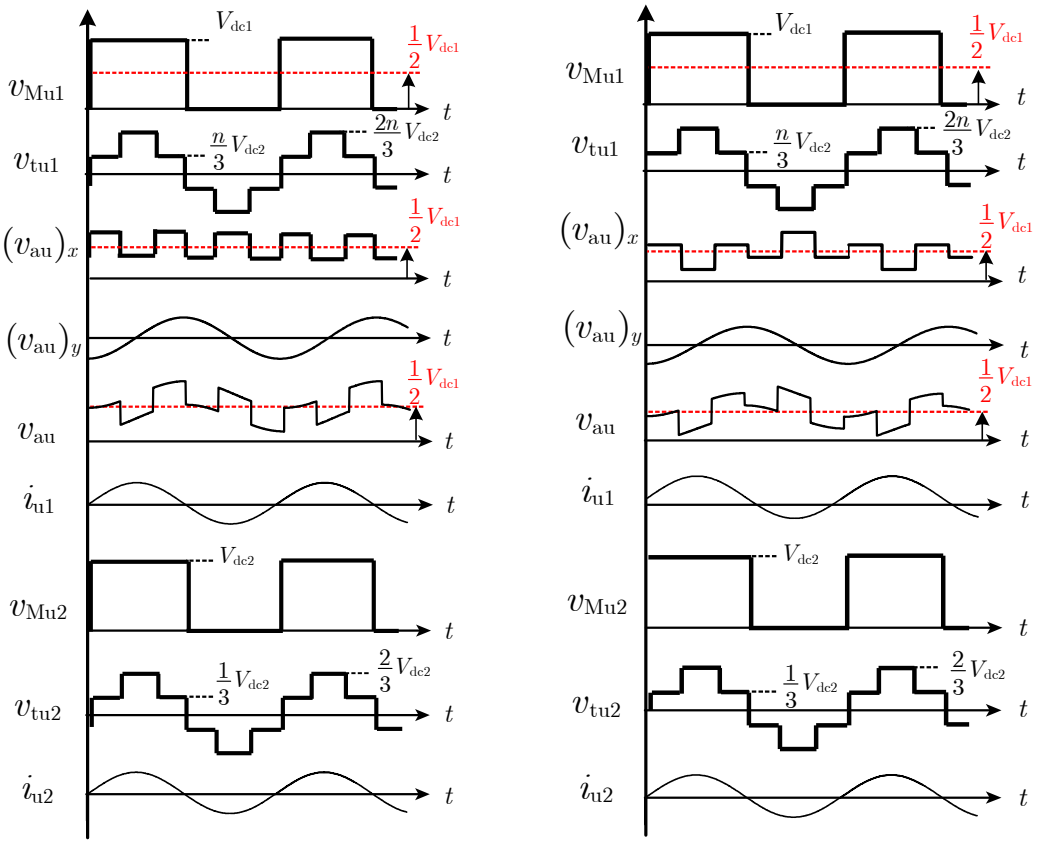

Figure 3-2 Ideal operating waveforms. (a) when $n\gamma = 1$; (b) when $n\gamma > 1$.

phase shift to control current and power, which is clearly reflected in (3.1). As a result, this converter can achieve zero reactive power on both the primary and secondary sides simultaneously, unlike the TP-DAB converter.

Operations in Auxiliary Converters

For convenience, the cascaded converters will be referred to as the auxiliary converters in subsequent discussions. The basic operation of the auxiliary converter is similar to that of a multilevel converter, with a switching frequency of f_{s2}, which is much higher than f_{s1}. The auxiliary converter employs PS-PWM, where the carrier waves for each cell in u-phase are phase-shifted by $360/N$ degrees relative to each other. This results in a higher effective frequency ($=Nf_{s2}$), leading to improved current control performance. It should be noted that this Chapter does not discuss the effects of switching-frequency ripple, and ideal waveforms presented will not include switching-frequency ripple.

Basic Operations, Equivalent Circuits and Equations

Firstly, the two main converters (i.e., main converter 1 and main converter 2) use the same gate signals, producing the same square wave with a 50% duty

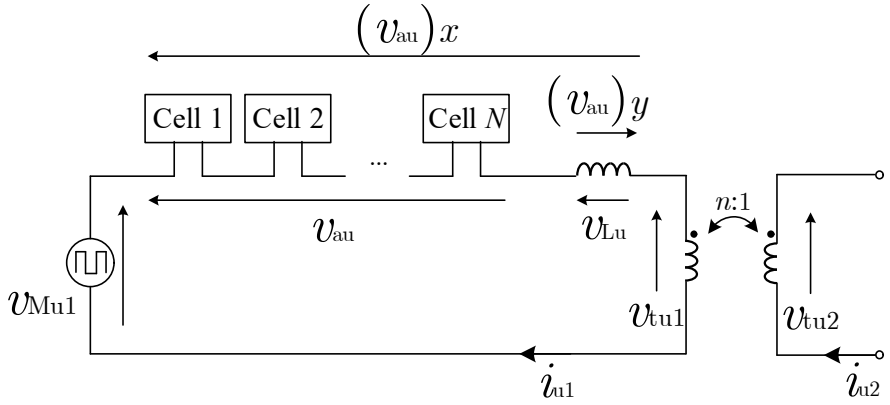

Figure 3-3 Simplified circuit of NPW-CC DC-DC converter seen from primary side.

cycle, where v_{Mu1} and v_{Mu2}.can be expressed as

$$\begin{cases} v_{\mathrm{Mu1}} = V_{\mathrm{dc1}}\mathrm{S_{Q1}} \\ v_{\mathrm{Mu2}} = V_{\mathrm{dc2}}\mathrm{S_{Q7}} = V_{\mathrm{dc2}}\mathrm{S_{Q1}} \,. \end{cases} \tag{3.2}$$

Besides, since the transformer is Y-connected (star connection), the voltage of the transformer secondary winding can be derived as:

$$v_{\mathrm{tu2}} = V_{\mathrm{dc2}}\left(\frac{2}{3}\mathrm{S_{Q7}} - \frac{1}{3}\mathrm{S_{Q8}} - \frac{1}{3}\mathrm{S_{Q9}}\right). \tag{3.3}$$

Subsequently, the voltage the transformer primary winding can also be obtained as:

$$v_{\mathrm{tu1}} = nv_{\mathrm{tu2}} = nV_{\mathrm{dc2}}\left(\frac{2}{3}\mathrm{S_{Q7}} - \frac{1}{3}\mathrm{S_{Q8}} - \frac{1}{3}\mathrm{S_{Q9}}\right). \tag{3.4}$$

For convenience, a coefficient is used to denote the voltage conversion ratio as:

$$\gamma = \frac{V_{\mathrm{dc2}}}{V_{\mathrm{dc1}}}. \tag{3.5}$$

Hence, (3.4) can be rewritten by

$$v_{\mathrm{tu1}} = n\gamma V_{\mathrm{dc1}}\left(\frac{2}{3}\mathrm{S_{Q7}} - \frac{1}{3}\mathrm{S_{Q8}} - \frac{1}{3}\mathrm{S_{Q9}}\right). \tag{3.6}$$

Figure 3-2 (a) and (b) show the ideal waveforms for the NPW-CC DC-DC converter when $n\gamma$=1 and when $n\gamma$>1, respectively. It should be noted that, when the duty cycles of the main converters are fixed at 0.5, the voltage waveform of the transformer winding is a standard six-step square wave just like displayed in Figure 3-2. The aforementioned equations effectively transform the secondary side into an equivalent voltage source on the primary side. By doing this, the equivalent circuit of u-phase can be drawn, as shown in Figure 3-3.

The KVL equation of the Figure 3-3 circuit can be given by

$$v_{\mathrm{Mu1}} = v_{\mathrm{tu1}} + v_{\mathrm{au}} + v_{\mathrm{Lu}} \,, \tag{3.7}$$

or

$$v_{\mathrm{au}} = v_{\mathrm{Mu1}} - v_{\mathrm{tu1}} - v_{\mathrm{Lu}}\,. \tag{3.8}$$

v_{au} in (3.8) is divided into two parts as

$$v_{\mathrm{au}} = \left(v_{\mathrm{au}}\right)_x + \left(v_{\mathrm{au}}\right)_y, \tag{3.9}$$

where

$$\begin{cases} \left(v_{\mathrm{au}}\right)_x = v_{\mathrm{Mu1}} - v_{\mathrm{tu1}} \\ \left(v_{\mathrm{au}}\right)_y = -v_{\mathrm{Lu}} \end{cases}. \tag{3.10}$$

Obviously, since duty cycles for the main converters are fixed, $(v_{\mathrm{au}})_x$ is also a fixed waveform only determined by V_{dc1} and $n\gamma$, which can be expressed by

$$\left(v_{\mathrm{au}}\right)_x = v_{\mathrm{Mu1}} - v_{\mathrm{tu1}} = V_{\mathrm{dc1}}\left(\frac{3-2n\gamma}{3}\mathrm{S_{Q7}} - \frac{n\gamma}{3}\mathrm{S_{Q8}} - \frac{n\gamma}{3}\mathrm{S_{Q9}}\right). \tag{3.11}$$

On the other hand, $(v_{\mathrm{au}})_y$ represents the current control effect in the auxiliary converter (i.e., the inductor voltage), which can be expressed by

$$\left(v_{\mathrm{au}}\right)_y = -v_{\mathrm{Lu}} = -L\frac{di_{\mathrm{u1}}}{dt}. \tag{3.12}$$

The proposed converter can theoretically generate any desired inductor current waveform via controlling the auxiliary converter. In this dissertation, to avoid reactive and harmonic currents, the current is set to be a sinusoidal wave that is in phase with v_{Mu1} and v_{Mu2} (also in phase with v_{tu1} and v_{tu2}). However, it should be noted that this current may contain a DC component, which is equal to zero only when $n\gamma$=1 (i.e., when V_{dc1}=nV_{dc2}). The u-phase currents are given by

$$\begin{aligned} i_{\mathrm{u1}} &= I_{\mathrm{ac}}\sin\omega_{\mathrm{s1}}t + I_{\mathrm{dc}} \\ i_{\mathrm{u2}} &= nI_{\mathrm{ac}}\sin\omega_{\mathrm{s1}}t \end{aligned}. \tag{3.13}$$

Meanwhile, the non-zero zero-sequence current does not influence the transformer operation, since the three-limb transformer has high magnetic resistance to the zero-sequence currents [143].

3.3 DC Zero-Sequence Current and Power Equations

As previously mentioned, the phase current may contain a zero-sequence component. This section will explain the origin of the zero-sequence component and the power transmission equation of the converter.

Figure 3-4 shows the simplified circuit of auxiliary converters, where its voltage and current are presented. Thus, the active power of auxiliary converter

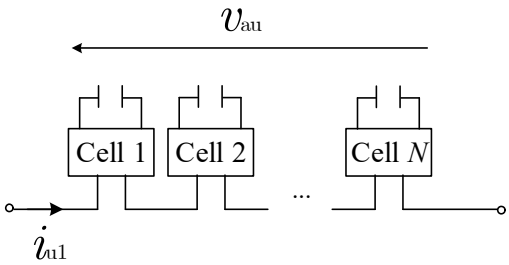

Figure 3-4 Auxiliar converter constructed by cascaded converters.

can be given by

$$P_{a\_au} = \frac{1}{T_{s1}} \int_0^{T_{s1}} i_{u1} v_{au} dt \,. \tag{3.14}$$

v_{au} has been given by Eqs. (3.9)-(3.12), and it contains a non-zero fundamental component (f_{s1}) when $n\gamma \neq 1$. Besides, zero-sequence current is generally defined as the average of the three-phase currents. Typically, there are two scenarios in which zero-sequence current may exist in a circuit:

- When there is a three-phase imbalance;
- When there is a common component among the three phases that cannot be canceled out.

Since this dissertation does not discuss the issue of three-phase imbalance, the zero-sequence current must arise from a common component shared among the three phases. According to Fourier series, a periodic waveform contains harmonics that are integer multiples of the fundamental frequency. Among these components, the 0^{th} (i.e., DC component) and 3^{rd} (i.e., 3^{rd}, 6^{th}, 9^{th}, etc.) harmonics are common components. In fact, 3^{rd} harmonics current injection is a widely used technique for reducing peak current in three-phase system [144][145]. However, generating 3^{rd} harmonic current requires higher-frequency operation, which increases the burden on the power switching devices. Therefore, DC zero-sequence current is a better selection for the NPW-CC DC-DC converter.

Assume that i_{u1} consists of a sinusoidal component and an DC component expressed as (3.13). Then, since the auxiliary converter is composed entirely of passive components (no power source contained), non-zero active power implies a charging or discharging process (increasing or decreasing DC capacitor voltage). Therefore, to maintain a stable DC capacitor voltage in the auxiliary converter, it is necessary to ensure that the active power in the auxiliary converter equals to zero. That means

$$
\begin{aligned}
P_{\text{a\_au}} &= \frac{1}{T_{\text{s1}}}\int_0^{T_{\text{s1}}} i_{\text{u1}} v_{\text{au}} dt \\
&= \frac{1}{T_{\text{s1}}}\int_0^{T_{\text{s1}}} \left(v_{\text{Mu1}} - v_{\text{tu1}}\right) i_{\text{u1}} dt \\
&= \frac{1}{T_{\text{s1}}}\left\{\int_0^{T_{\text{s1}}} v_{\text{Mu1}} i_{\text{u1}} dt - \int_0^{T_{\text{s1}}} v_{\text{tu1}} i_{\text{u1}} dt\right\} \\
&= \frac{1}{T_{\text{s1}}}\left\{\int_0^{T_{\text{s1}}} v_{\text{Mu1}} i_{\text{u1}} dt - \int_0^{T_{\text{s1}}} v_{\text{tu2}} i_{\text{u2}} dt\right\} \\
&= \frac{1}{T_{\text{s1}}}\left\{\int_0^{T_{\text{s1}}} v_{\text{Mu1}} i_{\text{u1}} dt - \int_0^{T_{\text{s1}}} v_{\text{Mu2}} i_{\text{u2}} dt\right\} = 0
\end{aligned} \tag{3.15}
$$

Substituting (3.1), (3.2), and (3.13) into (3.15), the solution of DC current I_{dc} can be yielded as

$$
I_{\text{dc}} = I_{\text{ac}} \frac{2}{\pi}(n\gamma - 1) \tag{3.16}
$$

This equation explains that there is no DC current included in i_{u1} when $n\gamma = 1$. On the contrary, a DC current is superimposed on i_{u1} when $n\gamma \neq 1$ and it becomes larger as $n\gamma$ deviates from one. The zero-sequence current (or the neutral current) i_n can be given by $i_n = i_{\text{u1}} + i_{\text{v1}} + i_{\text{w1}}$. The ac components included in i_{u1}, i_{v1}, and i_{w1} are canceled each other out and only the DC component is contained in i_{n}. From the symmetry of the circuit operation, i_{v1} and i_{w1} produce the same DC current as i_{u1} expressed by (3.16). Hence, the ideal neutral current i_n can be given by

$$
i_n = I_n = 3I_{\text{dc}} = I_{\text{ac}} \frac{6}{\pi}(n\gamma - 1) \tag{3.17}
$$

At this point, the complete current equation for the converter has been derived as follows

$$
\begin{aligned}
i_{\text{u1}} &= I_{\text{ac}} \left[\sin \omega_{\text{s1}} t + \frac{2}{\pi}(n\gamma - 1)\right] \\
i_{\text{u2}} &= n I_{\text{ac}} \sin \omega_{\text{s1}} t
\end{aligned} \tag{3.18}
$$

Meanwhile, the total theoretical transmitted power of the NPW-CC DC-DC converter with fixed duty cycle ratios in main converters can be calculated as

$$
P_{\text{o}} = 3 \times \frac{1}{T_{\text{s1}}}\int_0^{T_{\text{s1}}} i_{\text{u1}} v_{\text{Mu1}} dt = \frac{3n\gamma V_{\text{dc1}}}{\pi} I_{\text{ac}} \tag{3.19}
$$

3.4 Control System

This section explains how the NPW-CC DC-DC converter controls the power flow through the auxiliary converter. For ease of explanation, the quantity of

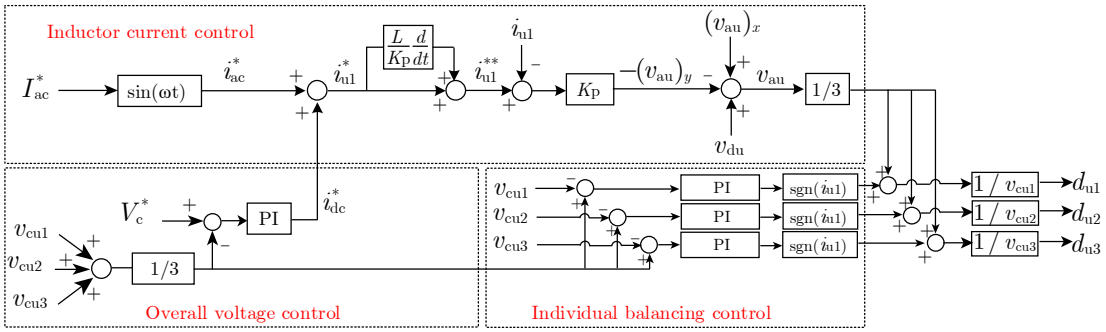

Figure 3-5 Block diagram for power-flow control in u-phase auxiliary converter.

cascaded choppers is set to three (N=3). Figure 3-5 shows the block diagram of the control system for the auxiliary converter in u-phase. As displayed in Figure 3-5, the control system of the NPW-CC DC-DC converter can be divided into three main parts:

- Current control,
- Overall voltage control,
- Individual balancing control.

In the power flow control including inductor current control and DC-capacitor voltage control, the main converters 1 and 2 operate with a fixed duty ratio of 0.5 and no control is applied to them. Hence, the power-flow control is achieved by the auxiliary converters. On the other hand, the inductor current control and the DC-capacitor voltage control of each phase are independent so that only the u-phase auxiliary converter control is discussed in the following.

Current Control

The inductor current i_{u1} contains the DC and AC components as shown in (3.18). In Figure 3-5, the reference for the desired u-phase inductor current (i_{u1}^*) is also divided into the AC component and the DC component, which is expressed by

$$i_{u1}^* = i_{ac}^* + i_{dc}^* , \tag{3.20}$$

where i_{ac}^* and i_{dc}^* represent the AC and DC components of i_{u1}^*, respectively. In (3.20), i_{ac}^* is set to generate a sinusoidal inductor current that is in phase with the fundamental component of v_{Mu1} and v_{tu1} as shown in Figure 2-2. However, the amplitude drop and phase delay occur between the control signal and the actual inductor current when the conventional P control is applied. Considering a simplified control system without any compensation as shown in

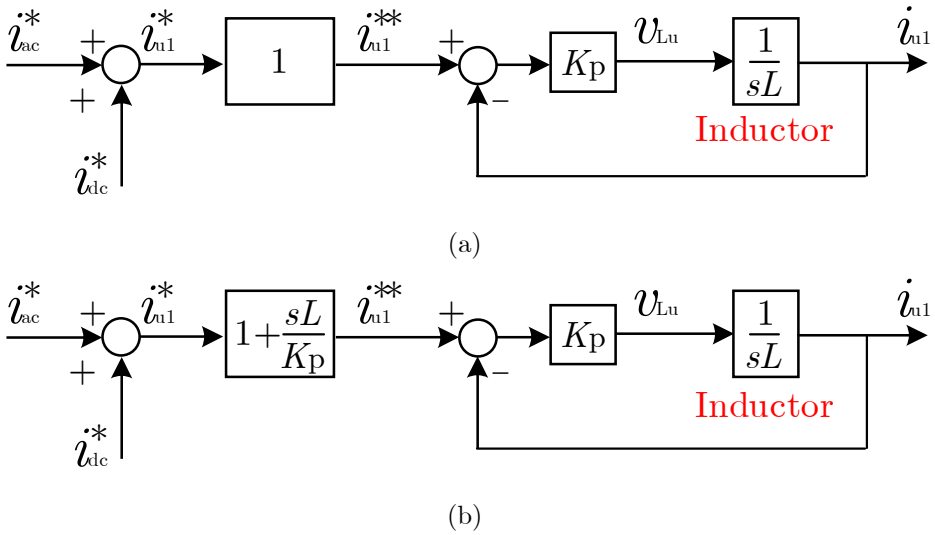

Figure 3-6 Simplified current feedback control system. (a) without feedforward compensation; (b) with feedforward compensation.

Figure 3-6 (a). The Laplace Transformation of this control system can be expressed as

$$i_{u1}(s) = \frac{K_p}{K_p + sL} i_{u1}^{**}(s) = \frac{K_p}{K_p + sL} i_{u1}^{*}(s). \tag{3.21}$$

It can be known from the above equation, i_{u1} cannot be controlled to equal to the reference current (i_{u1}^{*}) with only P controller. To solve this problem, a feedforward compensation method as shown in Figure 3-6 (b) is applied to i_{u1}^{*} which can be given by

$$i_{u1}(s) = \frac{K_p}{K_p + sL} i_{u1}^{**}(s) = \frac{K_p}{K_p + sL}\left[\frac{K_p + sL}{K_p} i_{u1}^{*}(s)\right], \tag{3.22}$$

where K_p is the proportional gain of the P controller in the inductor current control. If the a current as the waveform given by (3.18) is desired to flowing in the u-phase circuit, the reference input for the feedback current control (i_{u1}^{**}) with compensation should be as

$$i_{u1}^{**} = \left(1 + \frac{L}{K_p}\frac{d}{dt}\right) i_{u1}^{*} = I_{ac}^{*}\left\{\left[\sin\omega_{s1}t + i_{dc}^{*}\right] + \left[\frac{\omega_{s1}L}{K_p}\cos\omega_{s1}t + \frac{d}{dt} i_{dc}^{*}\right]\right\}. \tag{3.23}$$

It should be noted that i_{u1}^{**} is not the final desired inductor current, while it is just the reference input for the current feedback control system. Finaly, the inductor current i_{u1} should be equal to i_{u1}^{*}. The first term on the right-hand side in (3.22) denotes the desired inductor current while the second term is used for the amplitude and phase compensations. Meanwhile, i_{dc}^{*} is the DC current determined by the feedback control of the DC-capacitor voltages, which has

been explained in the previous section. Since it is basically a constant during steady-state, its derivative should be zero. However, it is important to note that during transient-state, the value of i_{dc}^{*} may change, so the compensation term of this part is also required for the control.

Furthermore, to improve the current control, v_{du} is added for the deadtime voltage compensation, which is given by

$$v_{\mathrm{du}} = -\mathrm{sgn}(i_{\mathrm{u1}})\frac{T_d}{T_{\mathrm{s2}}}V_{\mathrm{c}}^{*} = -\mathrm{sgn}(i_{\mathrm{u1}})T_d f_{\mathrm{s2}}V_{\mathrm{c}}^{*}, \tag{3.24}$$

where T_d and T_{s2} represent the dead time and the switching period of the auxiliary converters, respectively. Moreover, $\mathrm{sgn}(i_{\mathrm{u1}})$ is the signum function of i_{u1} which is equal to $+1$ when $i_{\mathrm{u1}} > 0$ and -1 when $i_{\mathrm{u1}} \leq 0$.

Overall Voltage Control

The DC-capacitor voltage control is divided into overall voltage control and individual balancing control as shown in Figure 3-5. The primary objective of the overall voltage control is to regulate the arithmetic average value of the DC-capacitor voltages in each chopper while simultaneously maintaining it at the desired value V_{c}^{*}. As analyzed in Section 3.3, the DC current is used to keep the overall DC-capacitor voltages in each auxiliary converter (or can say each cluster). Thus, this aim can be achieved by adjusting the DC component of the inductor current. Firstly, the arithmetic average value of the DC-capacitor voltages in each auxiliary converter is calculated. Subsequently, the reference value of the DC component (i.e., i_{dc}^{*}) is produced by the feedback control.

The overall voltage control produces a DC current which should be ideally equal to I_{dc} if transformer and inductor losses are negligible. Therefore, $\left|i_{\mathrm{dc}}^{*}\right|$ will be slightly larger than $\left|I_{\mathrm{dc}}\right|$ due to the practical power loss. As mentioned above, the zero-sequence current does not cause magnetic saturation to the three-limb core as the zero-sequence flux circulates through the air gap outside the core.

Individual Balancing Voltage Control

The aim of the individual balancing control is to balance the DC-capacitor voltage of each chopper to the arithmetic average value regulated by the overall voltage control. The input of the PI controller is the difference between the arithmetic average value of the DC-capacitor voltages and the real-time detected

value of each DC-capacitor voltage. On the other hand, the polarity of the output of the PI controller is changed according to the signum function of i_{u1}. The joint control containing the overall voltage control and the individual balancing control ensures that each DC-capacitor voltage is maintained at V_c^*.

Finally, the sum of the output used for the current and voltage controls is normalized by the corresponding DC-capacitor voltage and the duty ratio of each chopper (i.e., d_{u1}, d_{u2}, and d_{u3}) is produced as shown in Figure 3-5.

It should be noted that the DC voltage for each cascaded chopper (V_c^*) is set to the same value in this paper to simplify the control system. However, the proposed converter can also operate with unequal DC voltages in the auxiliary converter. Although it may be possible to reduce the power losses in the cascaded choppers using different DC voltages, the voltage balancing control and overall voltage control may be more complicated [139]. Hence, the same V_c^* is considered in this dissertation.

3.5 Initial Charge for Auxiliary Converters

The DC-capacitors of the auxiliary converters should be pre-charged before entering the operation, which is called as initial charge. The initial charge is achieved using the primary DC voltage source V_{dc1}. Figure 3-7 shows the basic principles of the initial charge. The initial charge is achieved by adjusting the duty ratio of Q_1, Q_2, and Q_3, while other power devices of the main converters (Q_4-Q_{12}) are always off during the initial charge (i.e., the low-side of main converter 1 and the secondary side is open). The cascaded choppers of the auxiliary converters are divided into three groups *A*, *B,* and *C* (since *N*=3) and the initial charge is carried out in order of $A \rightarrow B \rightarrow C$. The choppers in the same group are charged simultaneously. For example, Figure 3-7(a) shows the case when the DC-capacitors in group *A* are charged. The choppers in that group operate in a charge mode, i.e., the high-side devices of those choppers are always on and the corresponding low-side devices are always off as shown in Figure 3-7(b). Meanwhile, the choppers in other groups (*B* and *C*) operate in a short mode, which means that the low-side devices are always on while the high-side devices are always off as shown in Figure 3-7(c). The charging currents of phases u, v, and w converge at the neutral point of the transformer and return to the DC input source V_{dc1} through the neutral power wire. Similar to zero-sequence

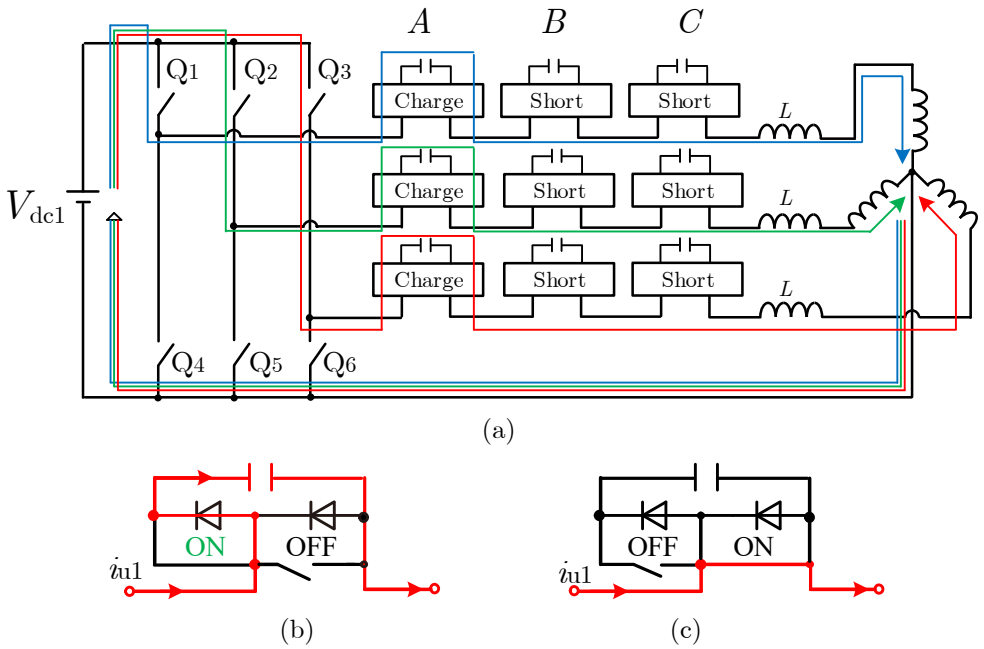

Figure 3-7 Operating principles for initial charge (a) Simplified circuit; (b) charge mode for choppers; (c) short mode for choppers.

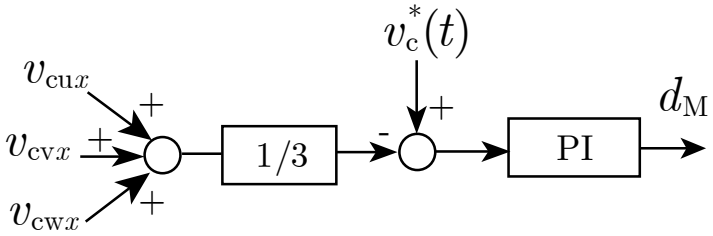

Figure 3-8 Control block diagram for initial charge. ($x = 1, 2, 3$).

current, additionally, this charging current does not cause core saturation in the transformer, as mentioned previously.

Furthermore, Figure 3-8 shows the control block diagram for the initial charge, where the feedback control is utilized. For instance, as Figure 3-7(a), when the DC-capacitors of the group A are charged, the arithmetic average value of the DC-capacitor voltages $(v_{cu1} + v_{cv1} + v_{cw1})/3$ is calculated. Then, the duty ratio d_M which is common to Q_1, Q_2, and Q_3 is determined by the PI controller. Moreover, in Figure 3-8, $v_c^*(t)$ is the reference value of DC-capacitor voltages, which is considered a ramp function in this dissertation as

$$v_c^*(t) = \frac{V_c^*}{T_c} t \,, \tag{3.25}$$

where V_c^* is the final targeted DC-capacitor voltage and also the reference value for normal operations, while T_c is the expected charge time for each group. This ramp function is used to limit the charge speed and to avoid overshoot voltages in DC-capacitors. After the completion of the initial charge

for the auxiliary converters, the NPW-CC DC-DC converter enters the normal operations and the control method is switched to the power flow control discussed in Section 3.4.

3.6 Analysis and Comparison with TP-DAB Converter

As previously mentioned, the main purpose of the proposed NPW-CC DC-DC converter is to achieve lower RMS and peak currents compared with the TP-DAB converter. This section shows a comprehensive comparison in terms of RMS and peak currents.

RMS and Peak Currents of NPW-CC DC-DC Converter

The inductor current of the NPW-CC DC-DC converter is a composite waveform of both AC and DC components, and its detailed equation has already been derived as shown in (3.18). Furthermore, the equation of transmitted power of the NPW-CC DC-DC converter is also shown as (3.19). Hence, first of all, the relation between P_{o} and I_{ac} can be obtained as

$$I_{\mathrm{ac}} = \frac{\pi}{3n\gamma V_{\mathrm{dc1}}} P_o = \frac{\pi}{3V_{\mathrm{dc2}}} P_o \,. \tag{3.26}$$

Subsequently, the inductor current can be written as a function of power and $n\gamma$ as

$$i_{\mathrm{u1}}\left(P_{\mathrm{o}},\ n\gamma\right) = \frac{\pi}{3n\gamma V_{\mathrm{dc1}}} P_o \left[\sin(\omega t) + \frac{2}{\pi}(n\gamma - 1)\right]. \tag{3.27}$$

Finally, the theoretical inductor RMS and peak currents can be calculated as:

$$\begin{cases} I_{\mathrm{rms}}\left(P_{\mathrm{o}},\ n\gamma\right) = \sqrt{\dfrac{1}{T_{s1}}\displaystyle\int_0^{T_{s1}} (i_{\mathrm{u1}})^2 dt} = \dfrac{\sqrt{4\pi(n\gamma-1)^2 + \dfrac{1}{2}\pi^2}}{3n\gamma V_{\mathrm{dc1}}} P_o \\ I_{\mathrm{peak}}\left(P_{\mathrm{o}},\ n\gamma\right) = \dfrac{\pi}{3n\gamma V_{\mathrm{dc1}}}\left[1 + \left|\dfrac{2}{\pi}(n\gamma - 1)\right|\right] P_o \end{cases} . \tag{3.28}$$

RMS and Peak Currents of TP-DAB Converter

The inductor current of the TP-DAB converter is a pure AC current. The detailed inductor current equations are given in Appendix I. Based on the contents in Appendix I, the RMS and peak currents of the TP-DAB converter can be obtained as

$$\begin{cases} I_{\mathrm{rms}}\left(P_{\mathrm{o}},\ n\gamma\right) = \sqrt{\dfrac{1}{\pi}\displaystyle\int_0^{\pi} (i_{\mathrm{u1}})^2 dt} \\ I_{\mathrm{peak}}\left(P_{\mathrm{o}},\ n\gamma\right) = \max\left\{i_1,\ i_2,\ i_3,\ i_4,\ i_5,\ i_6\right\}. \end{cases} \tag{3.29}$$

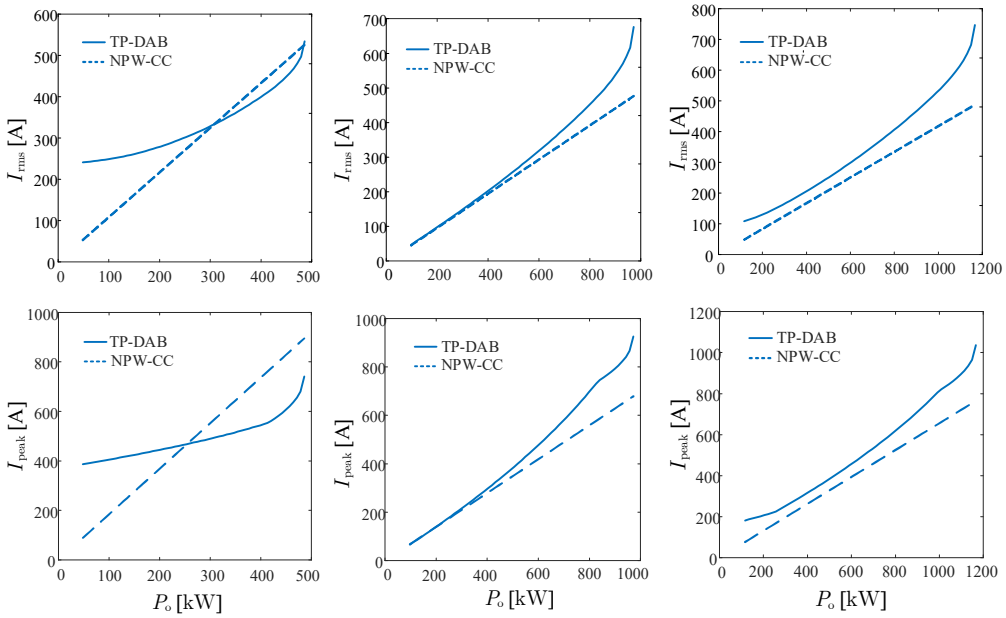

Figure 3-9 Comparison of RMS and peak currents under different output power. (a) when $n\gamma = 0.5$; (b) when $n\gamma = 1$; (c) when $n\gamma = 1.2$.

Comparison in Terms of RMS and Peak Currents

This dissertation compares the inductor RMS and peak currents of the NPW-CC DC-DC converter and the TP-DAB converter under three conditions: $n\gamma < 1$, $n\gamma = 1$, and $n\gamma > 1$. Since continuous plots are difficult to obtain, this dissertation only demonstrates three typical cases of $n\gamma = 0.5$, 1, and 1.2.

To ensure a fair comparison, the circuit parameters for both converters are set as follows:

- Both converters use the same switching frequency of 450 Hz (f_{s1}) for the three-phase bridges.
- Both converters use the same series inductance of 0.5 mH (L), and the same input DC voltage of 1.5 kV (V_{dc1}).

Figure 3-9 shows the comparisons in terms of RMS and peak currents under different output power. It can be observed that when $n\gamma \geq 1$, the NPW-CC DC-DC converter exhibits lower RMS and peak currents. This is because the NPW-CC DC-DC converter does not use phase shifting to control the current, giving it the advantages of zero reactive current and zero harmonic current. On the other hand, when $n\gamma < 1$, the NPW-CC DC-DC converter presents lower RMS and peak currents under light load conditions, while the TP-DAB converter presents lower RMS and peak currents under heavy load conditions. This

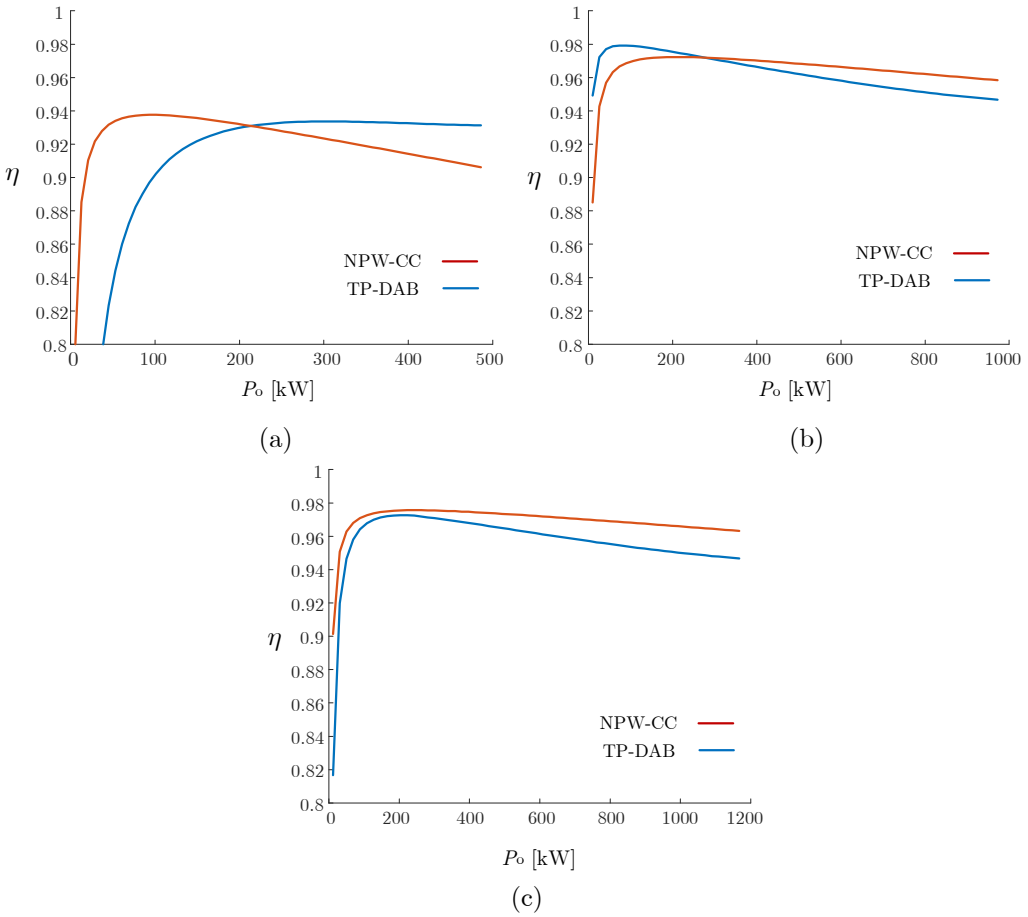

Figure 3-10 Comparison of conversion efficiency under different output power. (a) when $n\gamma = 0.5$; (b) when $n\gamma = 1$; (c) when $n\gamma = 1.2$.

is because the TP-DAB converter outputs almost no active power under light load (i.e., most of the current is reactive component), while the current in the NPW-CC DC-DC converter has a linear relationship with the load. However, due to the presence of a certain proportion of zero-sequence current in the NPW-CC DC-DC converter, it loses its advantage compared to the TP-DAB converter under heavy loads.

Comparison in Terms of Conversion Efficiency

This section carries out a comparison in terms of conversion efficiency between the NPW-CC DC-DC converter and the TP-DAB converter. To evaluate the conversion efficiency, IGBT modules (1MBI1000UG-330, 3.3 kV, 1 kA) from Fuji Electric and IGBT modules (CM1000DX-24T, 1.2 kV, 1 kA) from Mitsubishi Electric are used for main converters and auxiliary converters, respectively. Furthermore, following conditions are added additionally:

- No iron losses occur in inductors and transformer.
- Switching frequency of auxiliary converters is set to 3.6 kHz (f_{s2}), but

switching ripples are not considered.

- 30 mΩ resistance is considered in each primary side, as copper losses.
- V_c^* is set to 0.5 kV, and N is set to 3.

Under these conditions, Figure 3-10(a)–(c) compare the conversion efficiencies when $n\gamma = 0.5$, 1, and 1.2, respectively. From these figures, the preliminary conclusions can be drawn:

1) When $n\gamma < 1$, the NPW-CC converter has higher efficiency at light loads, while the TP-DAB converter presents higher efficiency at heavy loads. This is because the TP-DAB converter experiences significant reactive current at light loads, while the NPW-CC has large zero-sequence current at heavy loads.
2) When $n\gamma = 1$, the NPW-CC DC-DC converter does not need any zero-sequence current, while the TP-DAB converter also experiences very small reactive currents even at light loads (i.e., when ϕ is small). Nevertheless, the TP-DAB converter has higher efficiency at light loads, whereas the NPW-CC DC-DC converter has higher efficiency at heavy loads. This is because the NPW-CC DC-DC converter has more power components, although it has almost the same current as the TP-DAB converter at light loads as shown in Figure 3-9(b). With load increasing (i.e., ϕ increasing), the reactive current of the TP-DAB converter also rises, causing the NPW-CC DC-DC converter to surpass the TP-DAB converter in this case.
3) When $n\gamma > 1$, despite the NPW-CC DC-DC converter having more components than the TP-DAB converter, the absence of reactive and harmonic currents results in lower conduction losses, making the NPW-CC DC-DC converter superior to the TP-DAB converter.

3.7 Experimental Verification

This section demonstrates the validity of the proposed NPW-CC DC-DC converter using a 150 V, 2.5 kW experimental prototype as shown in Figure 3-11. In the downscaled setup, IGBT modules (2MBI150U2A-060, 600 V, 150 A) from Fuji Electric and discrete MOSFETs (FDH44N50, 500 V, 44 A) from Onsemi were utilized to constitute the main converters and the auxiliary converters, respectively. The control system is implemented by a DSP using TMS320C6678

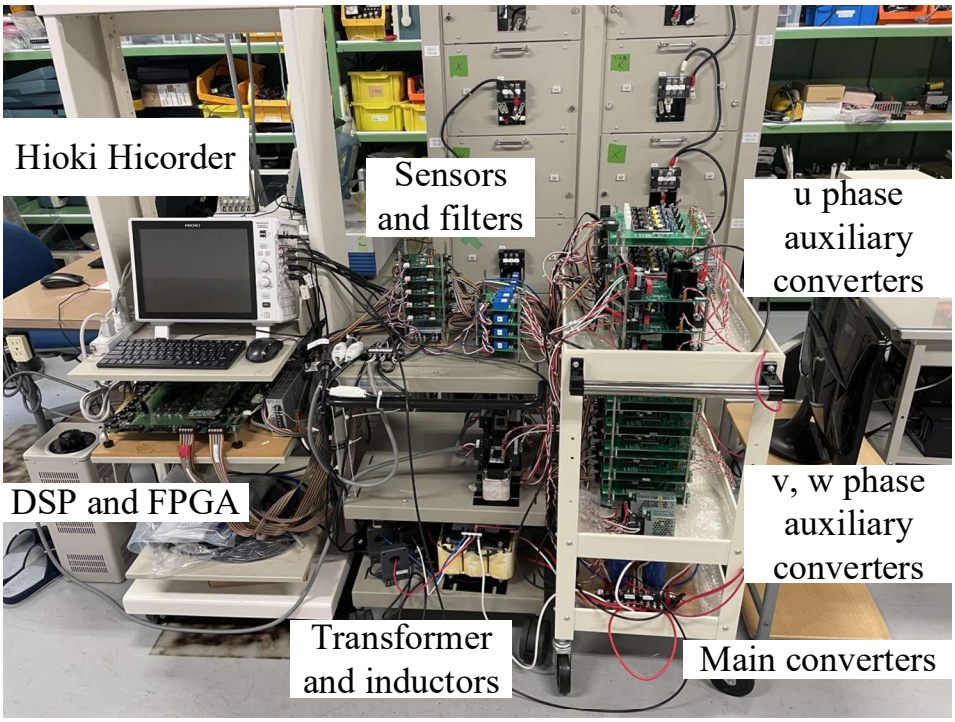

Figure 3-11 Exterior of experimental prototype.

from Texas Instruments and an FPGA using Cyclone IV from Intel. All the voltage and current waveforms were recorded using Hioki Memory Hicoder MR6000.

TABLE I shows the circuit parameters set for the experiments. The cascade quantity (N) is set to 3; the switching frequencies of the main converters and the choppers are set to 450 Hz (f_{s1}) and 7.2 kHz (f_{s2}), respectively. The PS-PWM is applied to the auxiliary converters so that the equivalent switching frequency of the auxiliary converter in each phase is 21.6 kHz ($=Nf_{s2}$). The operating frequency of the three-phase transformer is 450 Hz, while the windings turns ratio is set to $n = 1$. Moreover, the leakage inductance of the transformer in each phase is measured as 0.047 mH (L_k), and a series inductor of 0.18 mH (L_s) is used in each phase (i.e., total inductance $L = 0.23$ mH).

Initial Charge

The DC-capacitors of the auxiliary converters need to be pre-charged to the rated value of V_c^* before the operation and this can be achieved using the input voltage source, V_{dc1}. The charging method has been introduced in Section 3.5. Specifically, the DC-capacitors are changed from zero to the rated value under a ramp function given by (3.25). In this experiment, V_c^* was set to 55 V, and T_c was set to 200 ms. Figure 3-12 shows the voltage waveforms during the initial

TABLE I
TX AND RX COIL SPECIFICATIONS

Parameter Name	Symbol	Specification
INPUT DC VOLTAGE	V_{dc1}	120–150 V
OUTPUT DC VOLTAGE	V_{dc2}	120–150 V
CASCADE QUANTITY	N	3
Switching frequency of main converters	f_{s1}	450 Hz
Switching frequency of choppers	f_{s2}	7.2 kHz
Windings turns ratio	n	1
Total inductance	L	0.23 mH
Input capacitance	C_{in}	6600 uF
Output capacitance	C_{in}	6600 uF
Capacitance in each chopper	C_a	2000 uF
Rated Power	P_e	2.5 kW

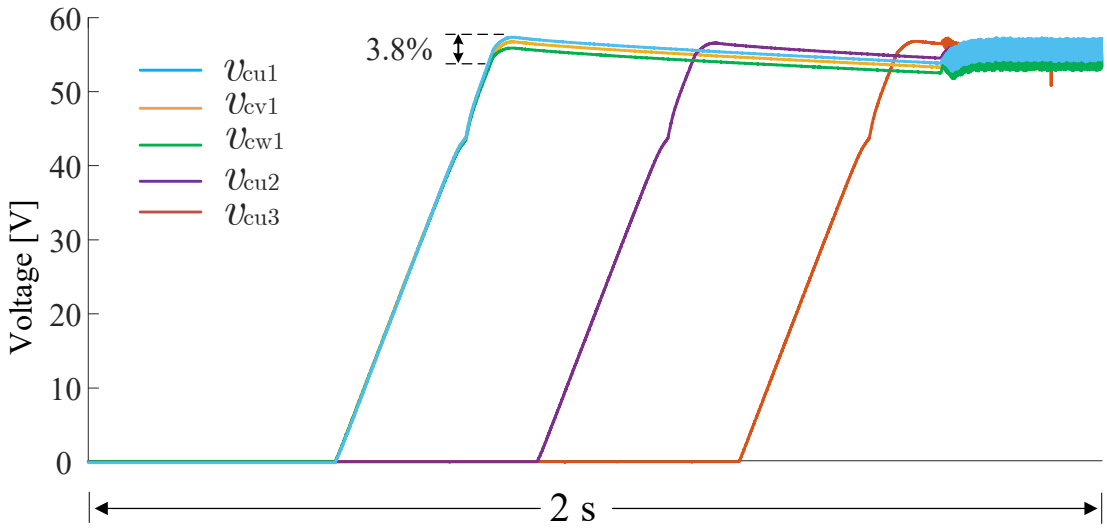

Figure 3-12 Experimental DC-capacitor voltage waveforms under initial charge.

charge, where it was implemented in order of A, B, C, which corresponds to $v_{cu1,cv1,cw1}$, v_{cu2}, and v_{cu3} in Figure 3-12. Each charging process was completed within 250 ms and the observed voltage overshoot was only 3.8%.

After the completion of the initial charge, the converter moves to the normal operation as displayed in Figure 3-12. In normal operations, ripple components are superimposed on the DC-capacitor voltages, which will be discussed in the following section.

Steady-State Experiments

Figure 3-13 shows the steady-state experimental waveforms when the power is transferred from the primary side to the secondary side. In the experiment of

Figure 3-13, V_{dc1} was set to 150 V; V_{dc2} was set to 130 V; V_c^* was set to 55 V; I_{ac}^* was set to +20 A, which is simultaneously applied to u/v/w phase.

The voltage waveforms of the DC capacitors in the auxiliary converters are kept at 55 V with a slight voltage ripple. This ripple is a result of the overall voltage control provided by Figure 3-5, which only ensures the one-period average value maintained at V_c^*, rather than the instantaneous value. Meanwhile, the amplitude of the voltage ripple is proportional to the inductor current, which can also be elucidated by (3.15). In addition, the phase difference of 120° exists in the AC components of each-phase DC-capacitor voltage (e.g., v_{cu1}, v_{cv1}, and v_{cw1}), which corresponds to the phase currents

On the other hand, it can be observed that the AC components both in the primary side currents (i.e., $i_{u1,v1,w1}$) and secondary side currents (i.e., $i_{u2,v2,w2}$) are sinusoidal and their amplitudes are 20 A. Meanwhile, the fundamental-frequency AC components of i_{u1} is in phase with v_{Mu1} and v_{tu1} as described in Section 3.2, leading to the mentioned zero-reactive-power operation.

Figure 3-14 shows the steady-state experimental waveforms when the power is transferred from the secondary side to the primary side. V_{dc2} was set to 140 V and I_{ac}^* was set to -15 A. The sinusoidal AC inductor current with an amplitude of 15 A is confirmed; however, i_{u1} is out of phase with v_{Mu1} and v_{tu1}, which means that the direction of power transmission is reversed. The DC voltage of the DC-capacitors in the auxiliary converters are also kept at 55 V.

To further verify the feasibility of the proposed system, the equivalent mode experiment and the experiment of $n\gamma > 1$ were also carried out. Figure 3-15 shows the steady-state experimental waveforms in equivalent mode when V_{dc1} was set to 140 V; V_{dc2} was set to 140 V; and I_{ac}^* was set to +20 A. Figure 3-16 shows the steady-state experimental waveforms of $n\gamma > 1$ when V_{dc1} was set to 140 V; V_{dc2} was set to 150 V; and I_{ac}^* was set to 15 A. In both experiments of Figure 3-15 and Figure 3-16, V_c^* was set to a constant value of 55 V. The sinusoidal currents are observed both in the primary side and the secondary side. Furthermore, the DC-capacitor voltages are always kept at 55 V, accompanied by a voltage ripple. Notably, the phase of the voltage ripple lags the corresponding current by 90°, while the amplitude of it is proportional to I_{ac}^*. In all of the steady-state experiments, the waveforms of v_{Mu1} and v_{tu1} basically match the simulated waveforms shown in Figure 2-4. However, there are

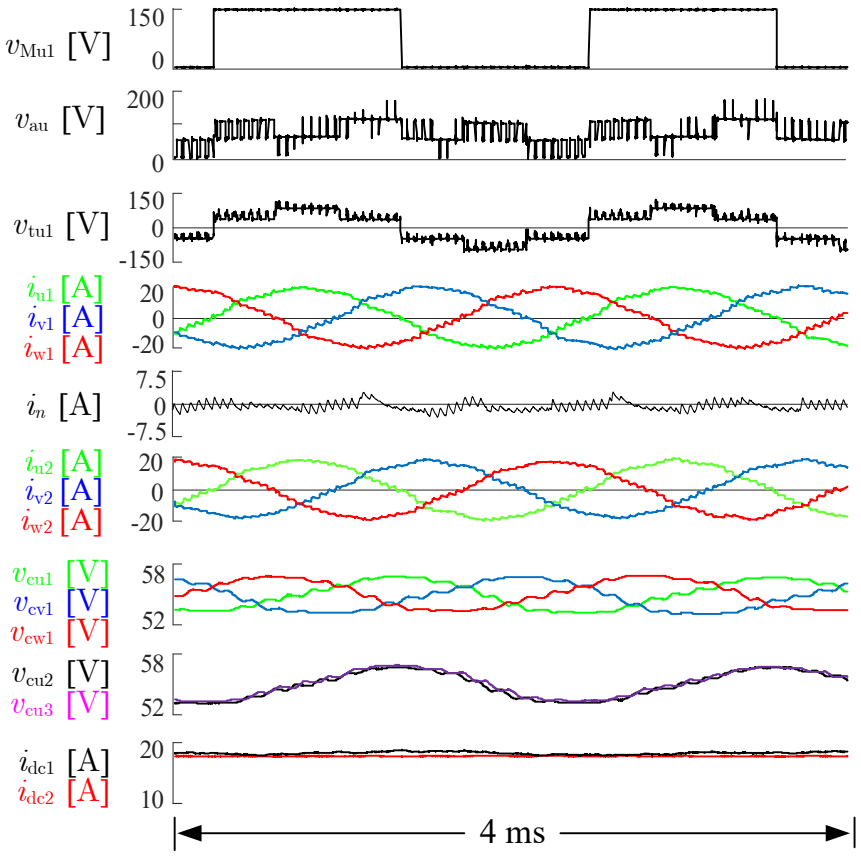

Figure 3-13 Steady-state experimental waveforms when V_{dc1}=150 V, V_{dc2}=130 V, I^*_{ac}=+20 A.

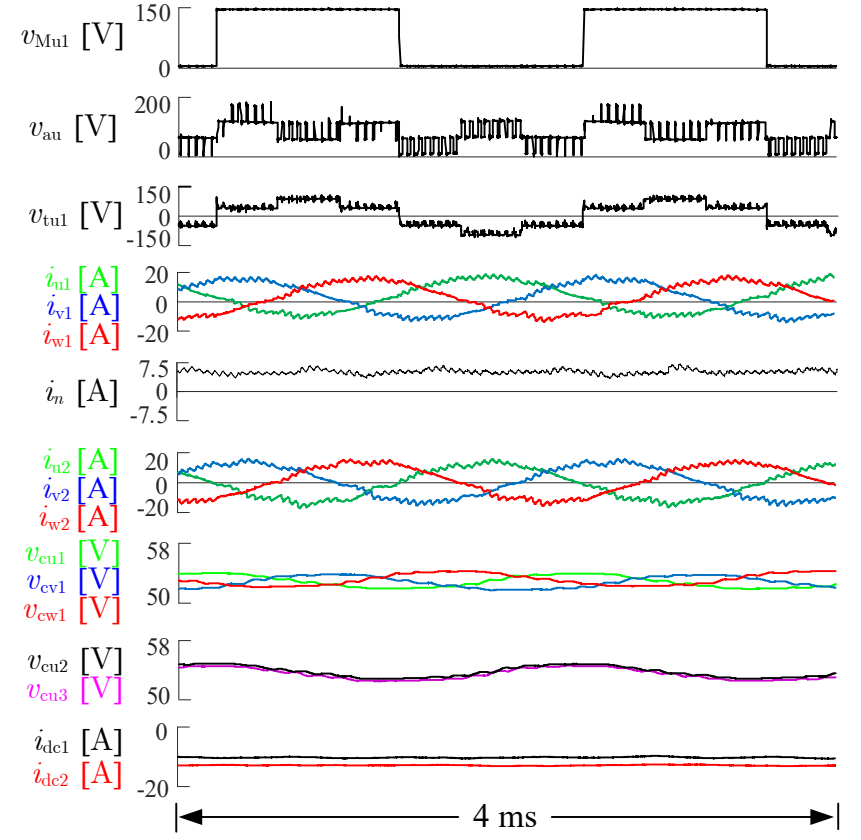

Figure 3-14 Steady-state experimental waveforms when V_{dc1}=150 V, V_{dc2}=140 V, I^*_{ac}=-15 A.

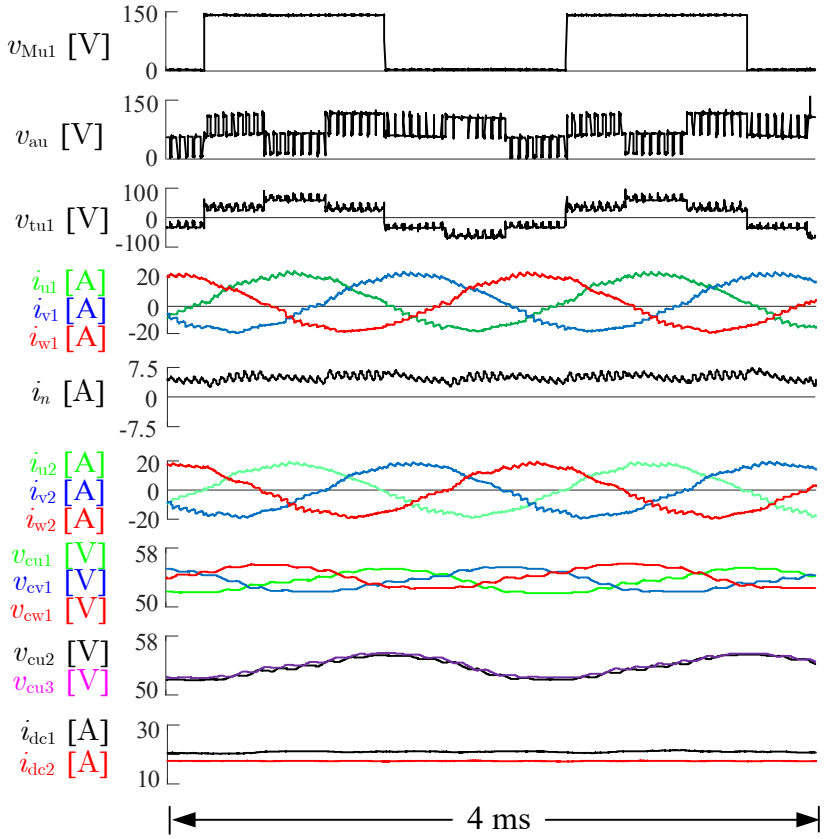

Figure 3-15 Steady-state experimental waveforms when V_{dc1}=140 V, V_{dc2}=140 V, I_{ac}^{*}=+20 A.

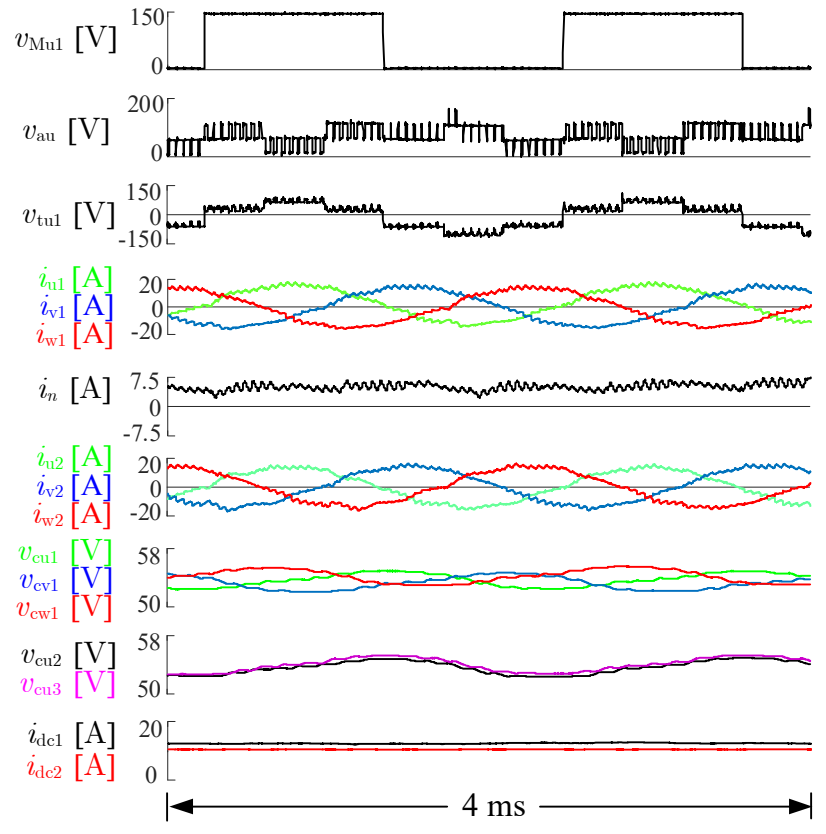

Figure 3-16 Steady-state experimental waveforms when V_{dc1}=140 V, V_{dc2}=150 V, I_{ac}^{*}=+15 A.

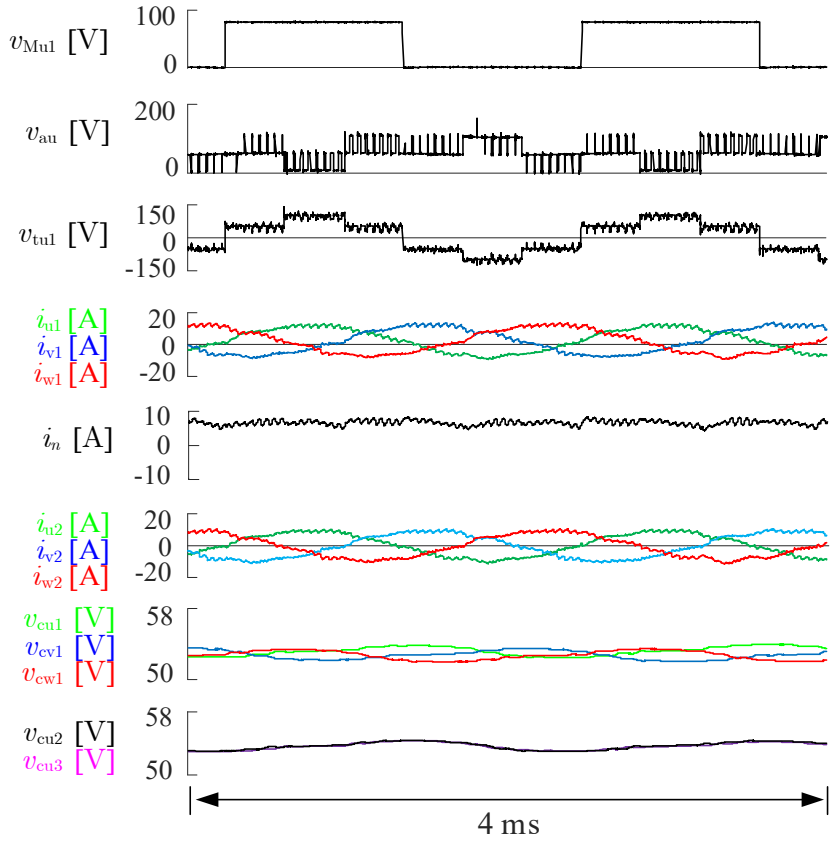

Figure 3-17 Steady-state experimental waveforms when V_{dc1}=120 V, V_{dc2}=150 V, I^*_{ac}=+10 A.

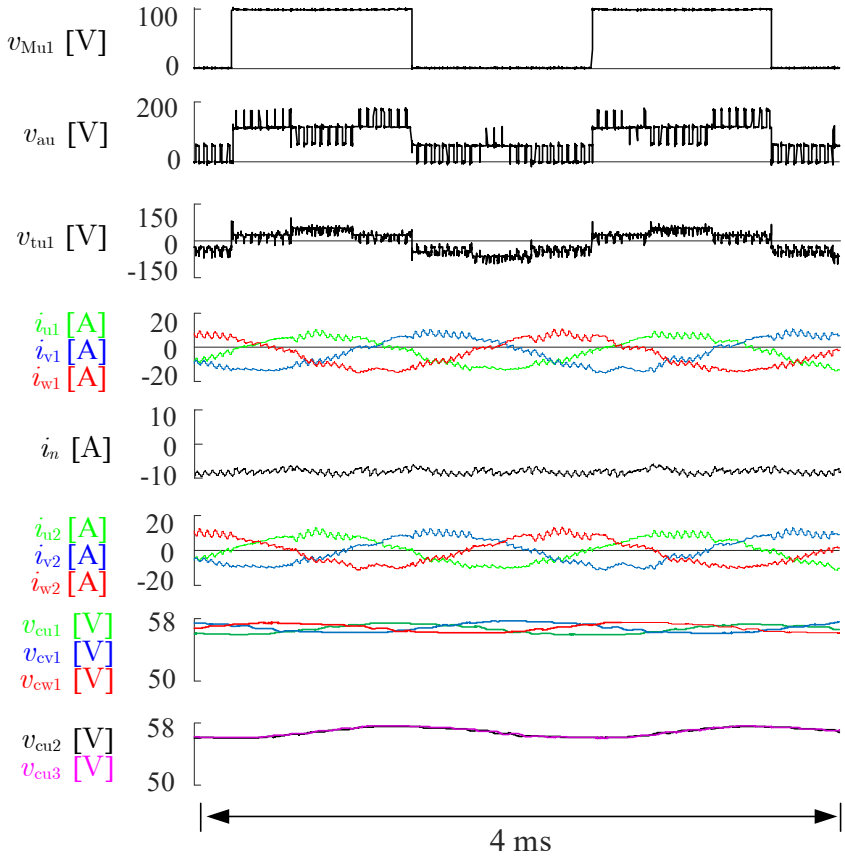

Figure 3-18 Steady-state experimental waveforms when V_{dc1}=150 V, V_{dc2}=75 V, I^*_{ac}=+10 A.

high-frequency switching-ripple components superimposed on the experimental waveform of v_{tu1} while the theoretical v_{tu1} does not contain switching-ripple components. The reason is that the theoretical waveforms are introduced based on the ideal transformer without the leakage inductance while the actual transformer contains the leakage inductance. On the other hand, the switching-ripple voltages are superimposed on v_{au} in all the steady-state experimental waveforms. However, the switching-ripple currents on i_{u1}, i_{v1}, and i_{w1} are negligible since the high-frequency voltages (i.e., 21.6 kHz components) are filtered by the reactor L.

Furthermore, i_{u1}, i_{v1}, i_{w1}, and i_n also contain DC components. The steady-state experimental waveforms show that a DC current of -0.28 A is present in i_n of Figure 3-13; a DC current of +5.18 A is present in i_n of Figure 3-14; a DC current of +4.95 A is present in i_n of Figure 3-15; and a DC current of +5.05 A is present in i_n of Figure 3-16. These differences can be explained by the fact that the transformer losses are not considered in the theoretical analysis.

Finally, to test the validity of the proposed converter under border operating range (i.e., border $n\gamma$), two additional steady-state experiments were carried out, where $n\gamma$ is set to 1.25 (V_{dc1} = 120 V, V_{dc2} = 150 V) in Figure 3-17, and 0.5 (V_{dc1} = 150 V and V_{dc2} = 75 V) in Figure 3-18. According to (3.17), the converter will produce a large DC current in each phase and neutral point when $n\gamma$ is far from one. It can be observed that very similar performance is obtained just like other steady-state experiments shown in Figure 3-17. In addition, a DC current of +8.47 A is contained in the neutral point in Figure 3-17, and a DC current of -9.56 A is contained in the neutral point in Figure 3-18, which proves that a border $n\gamma$ certainly makes a larger DC current.

Transient-State Experiments

Figure 3-19 shows the transient-state experimental waveforms with the conditions when V_{dc1} = 150 V and V_{dc2} = 130 V. The DC-capacitor voltage, V_c^*, was set to 55 V and I_{ac}^* was changed from +15 A to -15 A at 0.03 s using a ramp function. After that, the gradual amplitude changes of i_{u2}, i_{v2}, and i_{w2} were observed from 0.02 s to 0.17 s, which means that the entire transient state was completed within 150 ms. In this transient-state experiment, the current direction was changed around 0.1 s. Therefore, the polarities of input and output

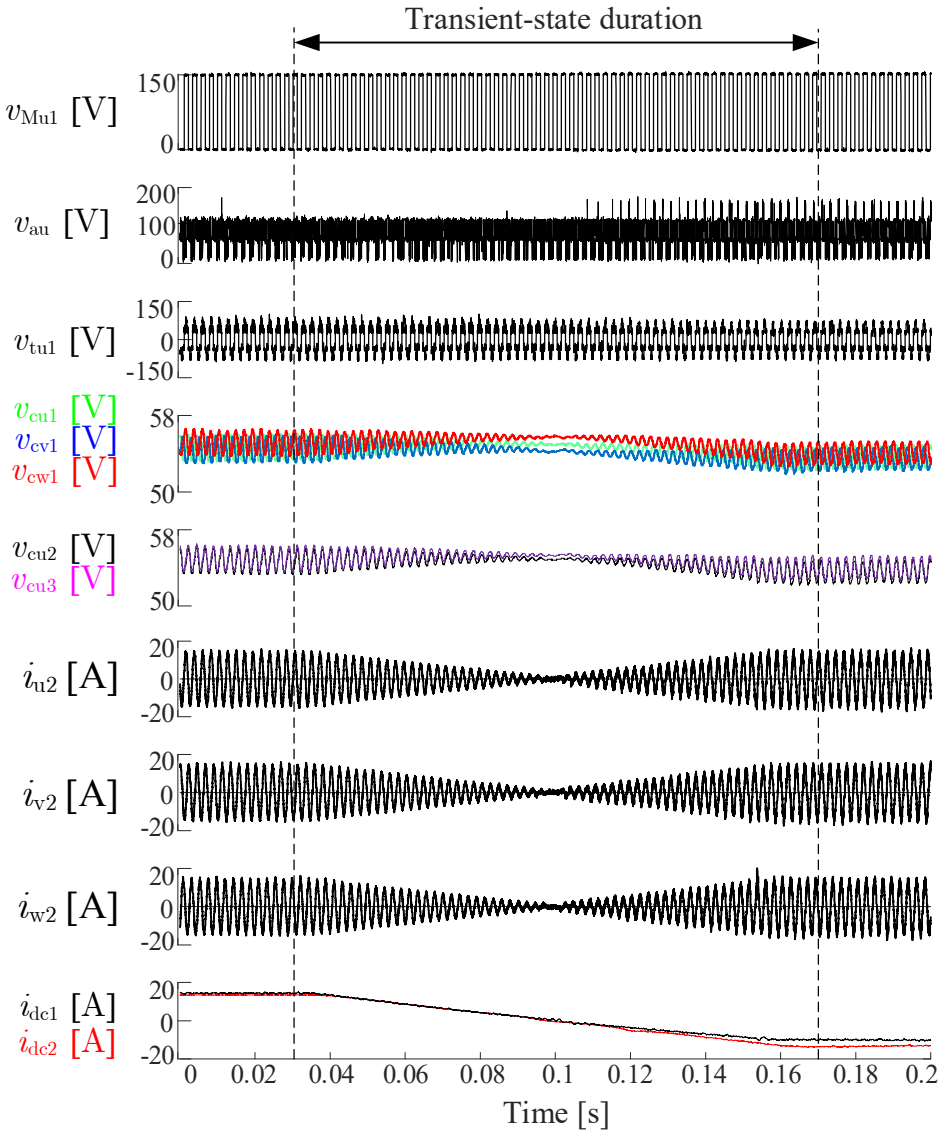

Figure 3-19 Transient-state experimental waveforms when I_{ac}^{*} is changed from +15 A to -15 A at 0.03 s.

currents (i.e., i_{dc1} and i_{dc2}) were also changed at the same time.

With the effect of the control strategy introduced in Section 3.4, the amplitude of inductor current in each phase are regulated from +15 A to -15 A with good accuracy. On the other hand, the DC-capacitor voltages, e.g., v_{cu1}, v_{cu2}, v_{cu3}, v_{cv1}, and v_{cw1}. recorded in Figure 3-19 are always kept at 55 V throughout the entire transient state, which further proves the validity of the Figure 3-5 control method. In addition, no overshoot voltage or overshoot current are observed in Figure 3-19.

Conversion Efficiency

The conversion efficiency has been also calculated using the measured input

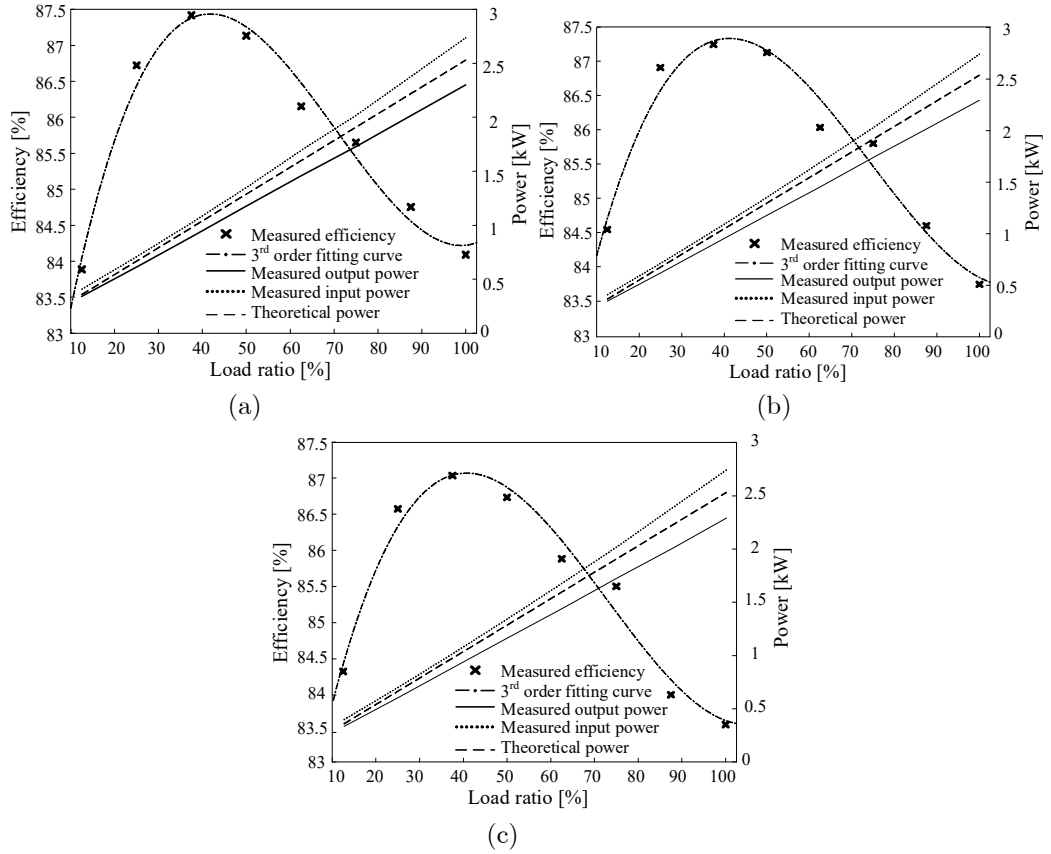

Figure 3-20 Measured efficiency curves in the experiments. (a) $V_{dc1}=150$ V, $V_{dc2}=130$ V. (b) $V_{dc1}=130$ V, $V_{dc2}=130$ V. (c) $V_{dc1}=120$ V, $V_{dc2}=130$ V

power and output power in the experiments. Figure 3-20(a), (b), and (c) illustrate the experimentally measured efficiencies with their corresponding 3rd order fitting curves for $n\gamma<1$, $n\gamma=1$, and $n\gamma>1$, respectively. To ensure the consistency of the experimental results, the output power was constrained to a fixed range by setting V_{dc2} to a constant value (= 130 V). while the dc input voltage (i.e., V_{dc1}) was changed to accommodate different $n\gamma$. As specified in TABLE I, the rated output power was set at 2.5 kW which corresponds an I_{ac}^{*} value of +20 A.

Figure 3-20 demonstrates that the conversion efficiency decreases if the $n\gamma$ goes higher. The reason can be considered as follows: The converter produced almost a zero DC current in Figure 3-13 (when $V_{dc1}=150$ V, $V_{dc2}=130$ V, $I_{ac}^{*}=+20$ A); it means the power loss in the transformer canceled the negative DC current of (3.16). On the other hand, the DC current could not been canceled when $n\gamma=1$ and was even increased when $n\gamma>1$, like shown as Figure 3-15 and Figure 3-17. Consequently, the Figure 3-20(a) case has the lowest RMS

current and conduction power losses, while the Figure 3-20(c) case has the highest RMS current and conduction power losses.

The experimentally measured efficiency is not so satisfactory because of the following several reasons:

- The quantity of cascaded choppers (N) has not been optimized.
- The switching frequency of the auxiliary converters has also not been optimized.
- The voltage and current are much lower than the real application. As a result, the power modules and the transformer cannot work in the best state.

3.8 Conclusion

This Chapter has introduced a novel DC-DC converter suitable for local LVDC grids, called NPW-CC DC-DC converter. This isolated three-phase DC-DC converter features inherent zero-reactive-power operation using auxiliary cascaded choppers. The converter is isolated by a Yn-Y three-phase transformer and the electric power can be transferred bidirectionally. With the help of inherent zero-reactive-power operation, the proposed converter effectively reduces the RMS and peak currents compared with the TP-DAB converter in a wide range of voltage conversion ratio. Accordingly, the conduction losses and wire copper losses can be deceased. The improved overall conversion efficiency is also confirmed via the evaluated model.

A 150 V, 2.5 kW downscaled prototype has been constructed, and both steady-state and transient-state experiments have been conducted to verify the feasibility of the NPW-CC DC-DC converter.

Chapter 4 NPW-CC DC-DC Converter with Variable Duty Ratios

In the previous Chapter, a kind of cascaded converters DC-DC converter, NPW-CC DC-DC converter, has been introduced. The NPW-CC DC-DC converter presents the advantage of lower RMS and peak currents over the TP-DAB converter. However, there is still one issue left: large DC zero-sequence current flows in the primary side and potentially increase the RMS and peak currents, when $n\gamma$ is far from one. This section discusses the origin of the DC zero-sequence current and proposes a method to reduce the DC zero-sequence current.

4.1 Issue of DC Zero-sequence Currents

In the previous section 3.2, the basic operating principles of NPW-CC DC-DC converter have been introduced. Meanwhile, the DC zero-sequence current has been firstly mentioned in section 3.3. When the inductor current i_{u1} is set as a sinusoidal waveform, the DC current flowing in each phase has been given by (3.16), while the DC zero-sequence current of has been calculated as (3.17). Although this DC zero-sequence current does not affect the operation of the transformer, it may increase the RMS and peak values of each-phase inductor current. As a result, the NPW-CC DC-DC converter has higher RMS and peak currents than the TP-DAB converter under heavy-load condition in Figure 3-9(a). Similarly, the NPW-CC DC-DC converter presents a lower conversion efficiency than the TP-DAB converter in Figure 3-10(a) because of the same reason.

4.2 Origin of DC Currents

In section 3.3, the DC current in each phase is calculated by setting the

power of the auxiliary converters to be equal to zero. This section will take a different perspective to attempt to explain the essential cause of the DC current. It can be explained using the power equation. If no power losses are considered, the following power equation must hold:

$$\frac{1}{T_{s1}}\int_0^{T_{s1}} v_{Mu1} i_{u1} dt = \frac{1}{T_{s1}}\int_0^{T_{s1}} v_{tu1} i_{u1} dt = \frac{1}{T_{s1}}\int_0^{T_{s1}} v_{Mu2} i_{u2} dt\,. \tag{4.1}$$

The left, center, and right terms of (4.1) represent the active power of the u-phase main converter 1, u-phase transformer, and the u-phase main converter 2, respectively. It should be noted that the currents i_{u1} and i_{u2} are still set to be sinusoidal waveforms as (3.13). At the same time, since v_{Mu1} and v_{Mu2} are synchronized with a fixed duty of 0.5, they can be given by using (3.1) and (3.2) as

$$v_{Mu1} = \frac{1}{\gamma} v_{Mu2} = \begin{cases} V_{dc1} & 0 \le t < 0.5T_{s1} \\ 0 & 0.5T_{s1} \le t < T_{s1} \end{cases}. \tag{4.2}$$

Substituting (3.13) and (4.2) into (4.1), the following equation can be obtained:

$$\frac{1}{T_{s1}}\int_0^{\frac{T_{s1}}{2}} V_{dc1} I_{dc} dt + \frac{I_{ac}}{T_{s1}}\int_0^{\frac{T_{s1}}{2}} V_{dc1} \sin\left(\frac{T_{s1}}{2\pi} t\right) dt = \frac{nI_{ac}}{T_{s1}}\int_0^{\frac{T_{s1}}{2}} V_{dc2} \sin\left(\frac{T_{s1}}{2\pi} t\right) dt\,. \tag{4.3}$$

In (4.3), the first term on the left is the power generated from DC components; the second term on the left is the power generated from AC components. The DC current flowing in u-phase inductor can be derived by solving the above equation (the result is given by (3.16)). Move the second term on the left side to the right side, the equation is re-written as

$$\frac{1}{T_{s1}}\int_0^{\frac{T_{s1}}{2}} V_{dc1} I_{dc} dt = \frac{(n\gamma - 1) I_{ac}}{T_{s1}}\int_0^{\frac{T_{s1}}{2}} V_{dc1} \sin\left(\frac{T_{s1}}{2\pi} t\right) dt\,. \tag{4.4}$$

(4.4) implies that the essential cause of requiring a DC current is the difference on power generated from AC fundamental components. Thus, in fact, it is adequate to only focus on the DC components and AC fundamental components of v_{Mu1}, v_{tu1}, and v_{Mu2}. When duty is fixed at 0.5, the Fourier expansion formulas of v_{Mu1}, v_{tu1}, and v_{Mu2} are given by

$$v_{Mu1} = \frac{1}{2} V_{dc1} + \frac{2V_{dc1}}{\pi} \sin(\omega t) + \ldots, \tag{4.5}$$

$$v_{tu1} = n v_{tu2} = \frac{2n\gamma V_{dc1}}{\pi} \sin(\omega t) + \ldots, \tag{4.6}$$

$$v_{Mu2} = \frac{1}{2} \gamma V_{dc1} + \frac{2\gamma V_{dc1}}{\pi} \sin(\omega t) + \ldots. \tag{4.7}$$

Other harmonic components can be ignored here because they do not produce any active power. It can be seen that v_{Mu1} has a different AC fundamental

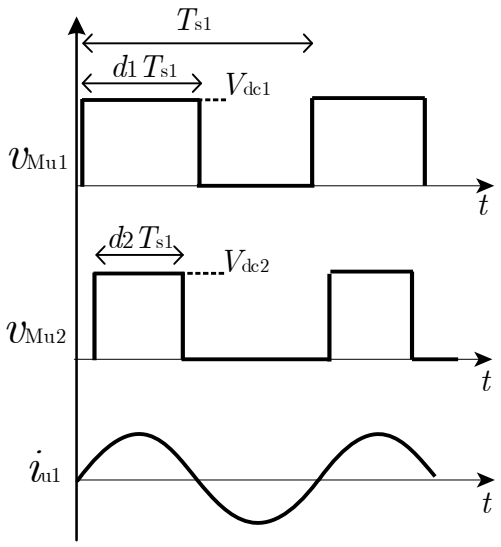

Figure 4-1 Key waveforms using variable duty ratios.

component from v_{tu1} (as well as the AC fundamental component of nv_{Mu2}) when $n\gamma \neq 1$, which causes the DC current.

4.3 DC Currents Reduction Using Variable Duty Ratios

According to the analysis in previous section, it is known that the dc current origins from the imbalance of the AC fundamental components between v_{Mu1} and v_{tu1} (or nv_{Mu2}). Hence, it implies that this issue can be solved by applying variable duty ratios to the main converters. Assuming the duty ratio of the main converter 1 equal to d_1 and the duty ratio of the main converter 2 equal to d_2, but their gate signals (e.g., S_{Q1} and S_{Q7}) should be still in phase with each other, as shown in Figure 4-1. In this context, the Fourier series of v_{Mu1}, v_{tu1}, and v_{Mu2} can be given by

$$v_{Mu1} = d_1 V_{dc1} + \frac{V_{dc1}}{\pi}[1 - \cos(2d_1\pi)]\sin(\omega t) + \ldots., \tag{4.8}$$

$$v_{tu1} = nv_{tu2} = \frac{n\gamma V_{dc1}}{\pi}[1 - \cos(2d_2\pi)]\sin(\omega t) + \ldots., \tag{4.9}$$

$$v_{Mu2} = d_2\gamma V_{dc1} + \frac{n\gamma V_{dc1}}{\pi}[1 - \cos(2d_2\pi)]\sin(\omega t) + \ldots. \tag{4.10}$$

It is simple to eliminate the DC currents by making the AC fundamental component in (4.8) be equal to that in (4.9). It can be expressed as the following equation:

$$n\gamma\cos(2d_2\pi) - \cos(2d_1\pi) = n\gamma - 1. \tag{4.11}$$

The duty ratio regulation strategy is based on (4.11). The strategy can be

TABLE II

DUTY RATIOS REGULATION FOR MAIN CONVERTERS

$n\gamma$	d_1	d_2
$n\gamma = 1$	0.5	0.5
$n\gamma < 1$	$1-\frac{\arcsin(n\gamma)}{\pi}$	0.5
$n\gamma > 1$	0.5	$\frac{\arcsin\left(\frac{1}{n\gamma}\right)}{\pi}$

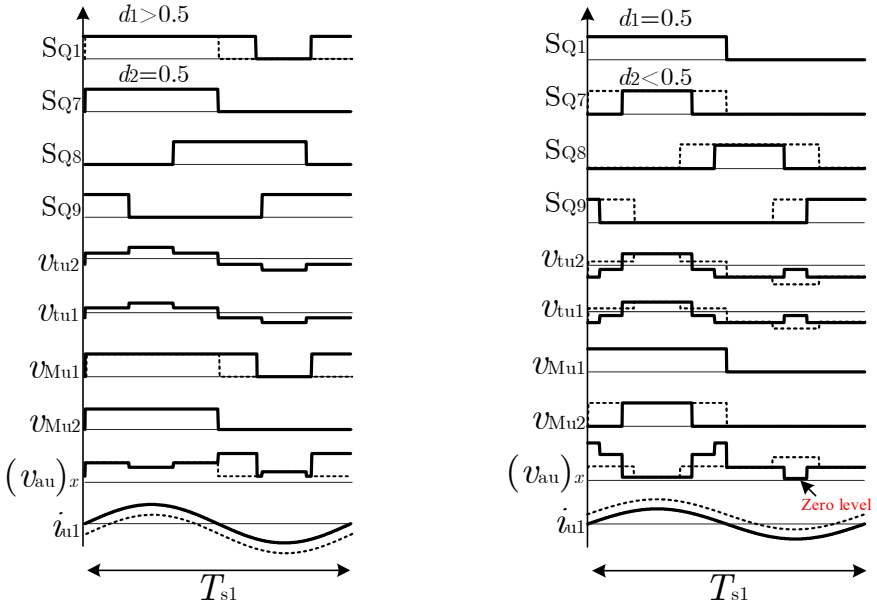

Figure 4-2 Ideal waveforms using variable duty ratios when (a) $n\gamma < 1$, (b) $n\gamma > 1$.

described as follows [146]: when $n\gamma = 1$, the duty ratios of both main converters are fixed at 0.5; when $n\gamma < 1$, d_2 is fixed at 0.5, and d_1 is increased to reduce the fundamental AC component of v_{Mu1}; when $n\gamma > 1$, d_1 is fixed at 0.5, and d_2 is decreased to reduce the fundamental AC component of v_{tu1}. It is noted that, d_1 should be kept at 0.5 when $n\gamma < 1$ and d_2 should be kept at 0.5 when $n\gamma > 1$ to ensure that the NPW-CC DC-DC converter can always output maximum power without zero-sequence current. Combining this strategy with the relationship given by (4.11), the duty ratios for the main converters can be calculated as listed in TABLE II.

Since the duty cycle is altered, the theoretical waveforms of the circuit also change, primarily reflected on $(v_{\mathrm{au}})_x$. The new $(v_{\mathrm{au}})_x$ can be calculated using the following equation:

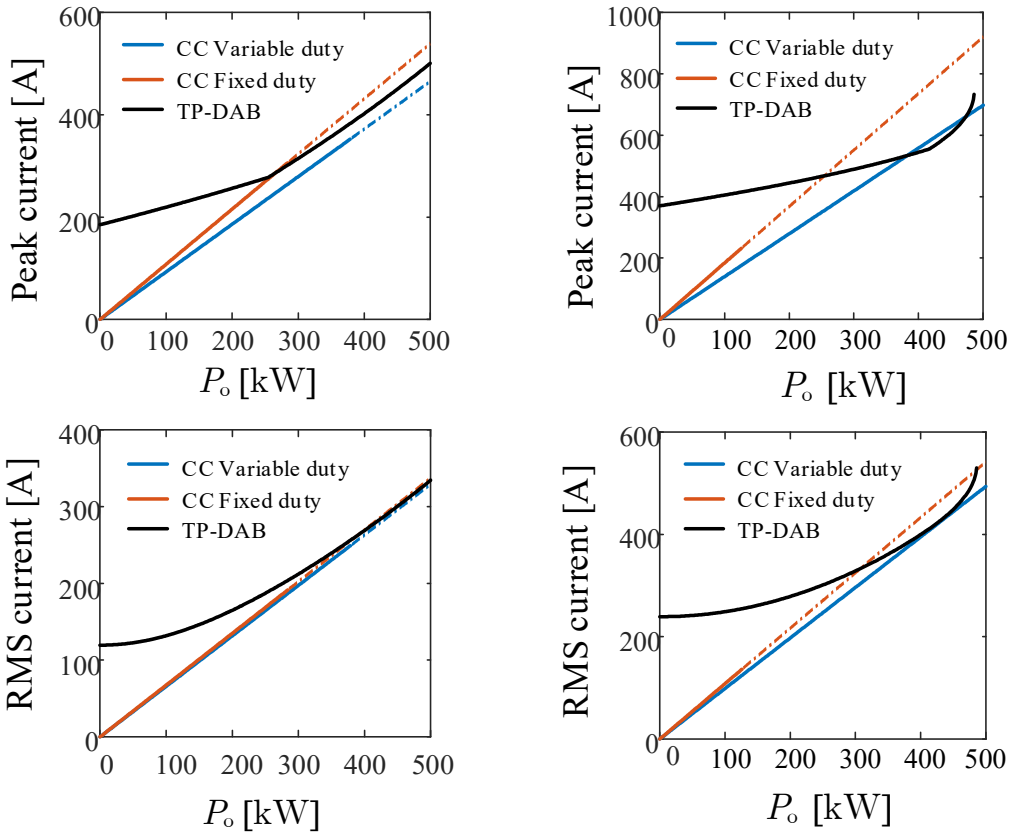

Figure 4-3 Comparisons in terms of RMS and peak current when (a) $n\gamma = 0.75$, (b) $n\gamma = 0.5$.

$$\left(v_{\mathrm{au}}\right)_x = V_{\mathrm{dc1}}\left(\mathrm{S_{Q1}} - \frac{2n\gamma}{3}\mathrm{S_{Q7}} + \frac{n\gamma}{3}\mathrm{S_{Q8}} + \frac{n\gamma}{3}\mathrm{S_{Q9}}\right). \tag{4.12}$$

Figure 4-2 shows the ideal waveforms with a variable duty ratio and those with a fixed ratio, where the solid lines and dashed lines represent the variable and fixed duty cycles, respectively. It can be seen that, $(v_{\mathrm{au}})_x$ with variable duty ratios becomes more complicated and higher compared with that with fixed duty ratios. That means applying variable duty ratios may increase the minimum voltage of the DC-capacitors in the auxiliary converters, then further increase the power losses. Nevertheless, the DC currents can be ideally eliminated.

When the duty is changed, the output equation can be given by

$$P_{\mathrm{o}} = \begin{cases} \dfrac{3n\gamma V_{\mathrm{dc1}}}{\pi} I_{\mathrm{ac}}, & n\gamma \le 1 \\ \dfrac{3V_{\mathrm{dc1}}}{\pi n\gamma} I_{\mathrm{ac}}, & n\gamma > 1\,. \end{cases} \tag{4.13}$$

It can be known from the above power equation that when $n\gamma \le 1$, the output power is same as that with fixed duty ratio, however, when $n\gamma > 1$, the output power is smaller than that with fixed duty ratio. Additionally, when

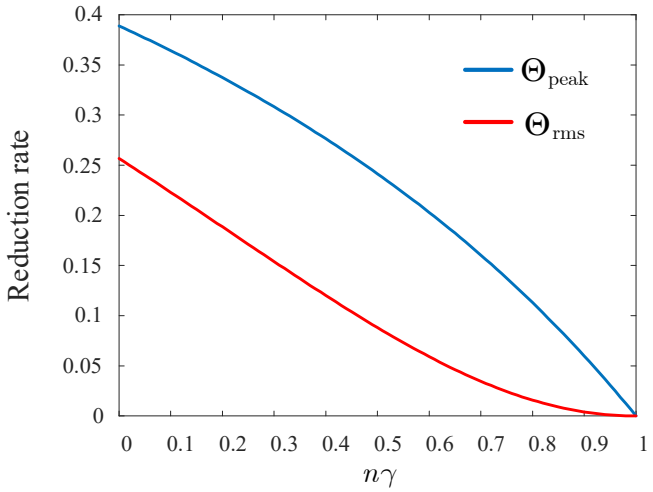

Figure 4-4 Reduction rates of RMS and peak currents.

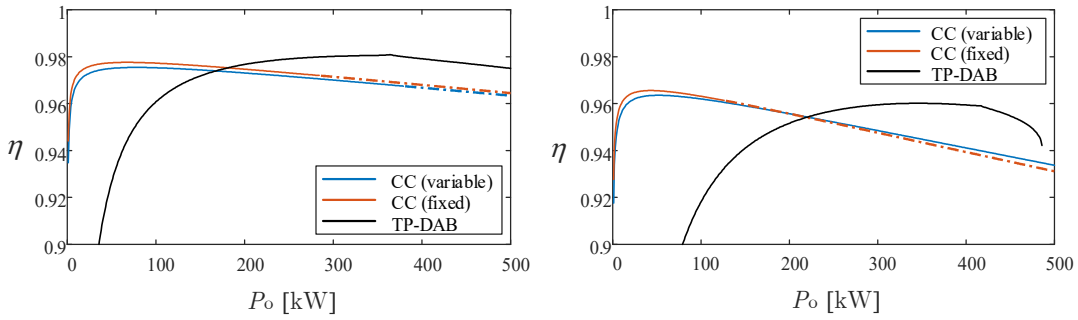

(a) (b)

Figure 4-5 Evaluated conversion efficiency when (a) $n\gamma = 0.75$, (b) $n\gamma = 0.5$.

$n\gamma > 1.15$, zero-voltage levels occurs in $(v_{au})_x$ [146], this phenomenon potentially cause overmodulation in auxiliary converters and makes this method not applicable to step-up applications. Thus, this Section only discusses the case of $n\gamma < 1$.

4.4 Reduction Effect and Efficiency Evaluation

This section focuses on the comparisons between the method using fixed duty ratio and the method using variable duty ratio when $n\gamma < 1$. The comparisons include peak and RMS currents, and conversion efficiency. Additionally, the corresponding results of the TP-DAB converter with SPS modulation are also provided for reference. The same converter models in Section 3.6 are used for performance evaluations.

Figure 4-3 shows the comparison in terms of RMS and peak currents of u-phase inductor current (i.e., i_{ul}) under different power. Figure 4-3(a) displays the case of $n\gamma = 0.75$ while Figure 4-3(b) displays the case of $n\gamma = 0.5$. It can

be observed that the reduction in current, particularly the peak current, is very significant. When using a fixed duty ratio, the peak current of the NPW-CC DC-DC converter exceeds that of the TP-DAB converter under heavy load, which would undoubtedly increase the size of the inductor and transformer. However, with a variable duty ratio, the DC current is entirely eliminated, resulting in that the peak current of the NPW-CC DC-DC converter being almost consistently lower than that of the TP-DAB converter.

The reduction rates of RMS and peak currents can be expressed by

$$\begin{cases} \Theta_{\text{peak}} = \dfrac{I_{\text{peak\_old}} - I_{\text{peak\_new}}}{I_{\text{peak\_old}}} = 1 - \dfrac{\pi}{\pi + 2 - 2n\gamma} \\ \Theta_{\text{rms}} = \dfrac{I_{\text{rms\_old}} - I_{\text{rms\_new}}}{I_{\text{rms\_old}}} = 1 - \dfrac{\pi}{\sqrt{\pi^2 + 4n^2\gamma^2 - 8n\gamma + 4}} \end{cases}. \tag{4.14}$$

where Θ_{peak} and Θ_{rms} indicate the reduction rates of the peak and RMS currents, respectively. In (4.14), $I_{\text{peak\_old}}$ and $I_{\text{peak\_new}}$ represent the peak and RMS currents using the fixed-duty method, while $I_{\text{rms\_old}}$ and $I_{\text{rms\_new}}$ denote the peak and RMS currents using variable duty ratio. They are given by

$$\begin{aligned} I_{\text{peak\_old}} &= |I_{\text{ac}}|(1 + \frac{2}{\pi} - \frac{2}{\pi} n\gamma), \\ I_{\text{rms\_old}} &= \left|I_{\text{ac}}\right| \sqrt{\frac{1}{2} + \frac{2}{\pi^2}(n^2\gamma^2 - 2n\gamma + 1)}, \\ I_{\text{peak\_new}} &= |I_{\text{ac}}|, \\ I_{\text{rms\_new}} &= \frac{1}{\sqrt{2}} \left|I_{\text{ac}}\right| \end{aligned} \quad . \tag{4.15}$$

The detailed derivation of RMS and peak currents is given in Appendix II. It can be calculated that Θ_{rms} is consistently lower than Θ_{peak} for $n\gamma < 1$ as shown in Figure 4-4, and this is the reason why the variable duty ratio is more effective at reducing the peak current than the RMS current.

Figure 4-5(a) and Figure 4-5(b) show the evaluated conversion efficiencies when $n\gamma = 0.75$ and $n\gamma = 0.5$, respectively. It is difficult to determine which one, i.e., variable duty ratio and fixed duty ratio, is superior, since they both exhibit very comparable conversion efficiency. Under light-load conditions, the fixed-duty method presents slightly better efficiency because switching losses are dominant, and the variable-duty method has higher switching losses due to higher V_{c}. When load becomes heavier, the variable-duty method gradually has better efficiency because conduction losses become dominant, and the fixed-

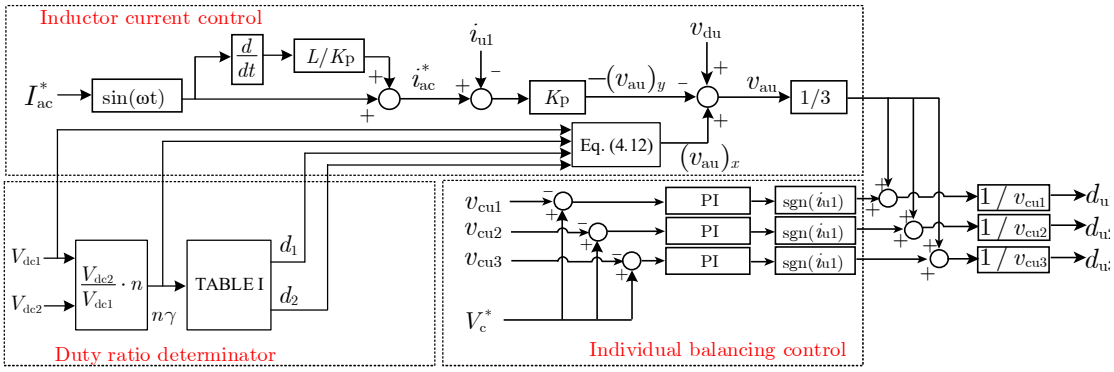

Figure 4-6 Block diagram of control system for variable-duty method.

duty method has higher conduction losses due to higher RMS current. Nevertheless, the efficiency difference between the two methods is just very small. However, the variable-duty method is useful to reduce the peak and RMS currents, particularly when $n\gamma$ is far from one as shown in Figure 4-4. Although the strategy of varying the duty ratio does not result in higher conversion efficiency, as the auxiliary converter requires a higher voltage (V_c), it can still significantly reduce the peak current. This means that this method can effectively lower the saturation risk of ferromagnetic components in the circuit, potentially reducing the volume and cost of the converter.

4.5 Control Systems

Figure 4-6 shows the block diagram of the control system for the NPW-CC DC-DC converter when the variable duty ratio is applied. Similar to the control system when the fixed duty ratio is applied, most of control strategies are the same, such as the inductor current control and the individual balancing control in Figure 3-5, Section 3.4. Therefore, this section only explains two obvious differences between the old and new methods.

Firstly, the overall voltage control is necessary in the old method to calculate the DC zero-sequence current, while it is not required in the variable-duty method because the auxiliary converters do not generate any active power ideally.

Secondly, in the old method, a constant duty ratio of 0.5 is applied for the main converters 1 and 2. However, in the variable-duty method, the duty ratios of the main converters (i.e., d_1 and d_2) are dynamically calculated by the duty ratio determinator as introduced in TABLE II. Then, the reference voltage of

$(v_{au})_x$ is subsequently determined by (4.12) using the real-time values of d_1, d_2, V_{dc1}, and $m\gamma$.

In addition, the initial charge control for this system is entirely same as that in Section 3.5, which is not discussed in this Chapter.

4.6 Experimental Verifications

This Chapter uses the same prototype as demonstrated in Section 3.7 for experimental verification. Nevertheless, some parameters are different from the experiments in Chapter 3.

- f_{s2} is set to be 3.6 kHz (7.2 kHz in Chapter 3).
- V_c is set to be 70 V for variable duty ratio and 55 V for fixed duty ratio.
- $m\gamma$ varies from 0.5 to 1.

Steady-State Experiments

Figure 4-7 and Figure 4-8 and show the experimental waveforms of the NPW-CC DC-DC converter applying the fixed duty ratio where $m\gamma$ is 0.75 and 0.5, respectively. In these experiments, V_c was set at 55 V; the reference value of I_{ac} (i.e., I_{ac}^*) was set at +15 A. It can be observed that all the phase currents (i.e., i_{u1}, i_{v1}, i_{w1}, i_{u2}, i_{v2}, and i_{w2}) are sinusoidal with an amplitude of 15 A, and the DC-capacitor voltages of the choppers (i.e., $v_{cu1,2,3}$, v_{cv1}, and v_{cw1}) are regulated at 55 V. In addition, the fundamental AC component of i_{u1} is in phase with that of v_{Mu1}. On the other hand, a DC current of -4.55 A flowing in the neutral point of the transformer (i_n) is confirmed in Figure 4-7, while a DC current of -10.97 A flowing in the neutral point of the transformer is confirmed in Figure 4-8. Since u, v, w phases of the NPW-CC DC-DC converter are balanced, it can be calculated from the measured data that a DC current of -1.52 A ($\approx -4.55/3$ A) and a DC current of -3.66 A ($\approx -10.97/3$ A) are superimposed in each primary-side phase current of Figure 4-7 and Figure 4-8, respectively. It should be noted that the experimental DC-current values are different from the theoretical DC-current values (-2.39 A for Figure 4-7 and -4.77 A for Figure 4-8) given by (3.17). This can happen because some unavoidable disturbances, such as switching-ripple components, tolerance of power devices and passive components, and power losses strongly influence the DC current. Figure 4-9 and Figure 4-10 show the experimental waveforms of

the

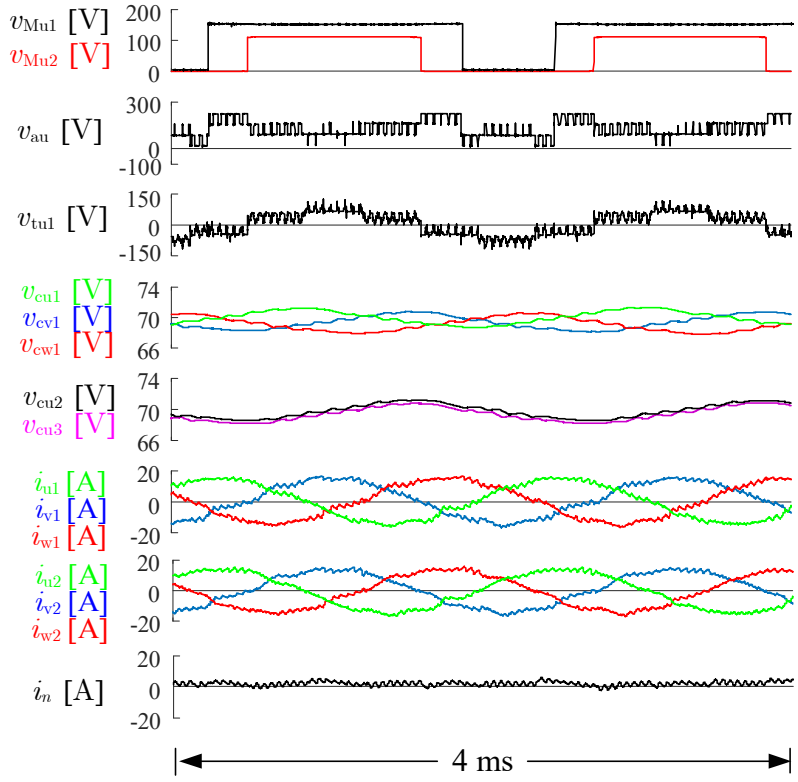

Figure 4-7 Experimental steady-state waveforms using variable duty ratio when $n\gamma = 0.75$ and $I_{ac}^{*} = +15$ A .

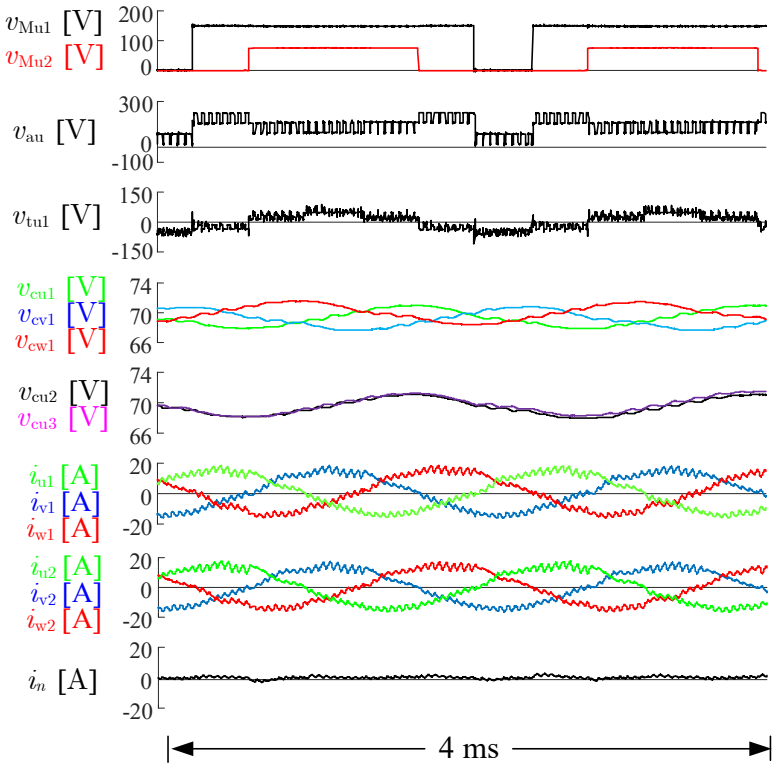

Figure 4-8 Experimental steady-state waveforms using variable duty ratio when $n\gamma = 0.5$ and $I_{ac}^{*} = +15$ A .

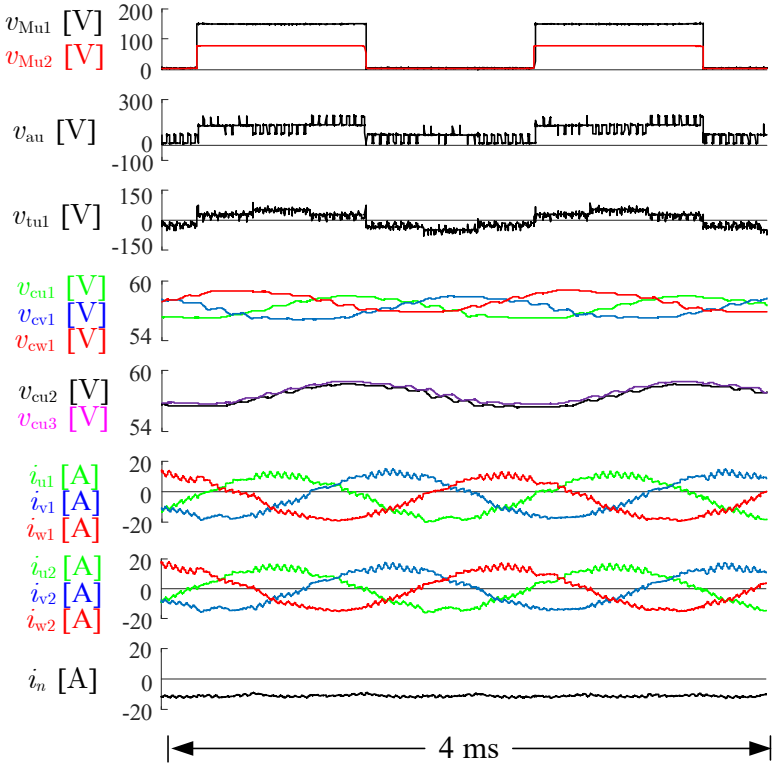

Figure 4-9 Experimental steady-state waveforms using fixed duty ratio when $n\gamma = 0.5$ and $I_{ac}^{*} = +15$ A .

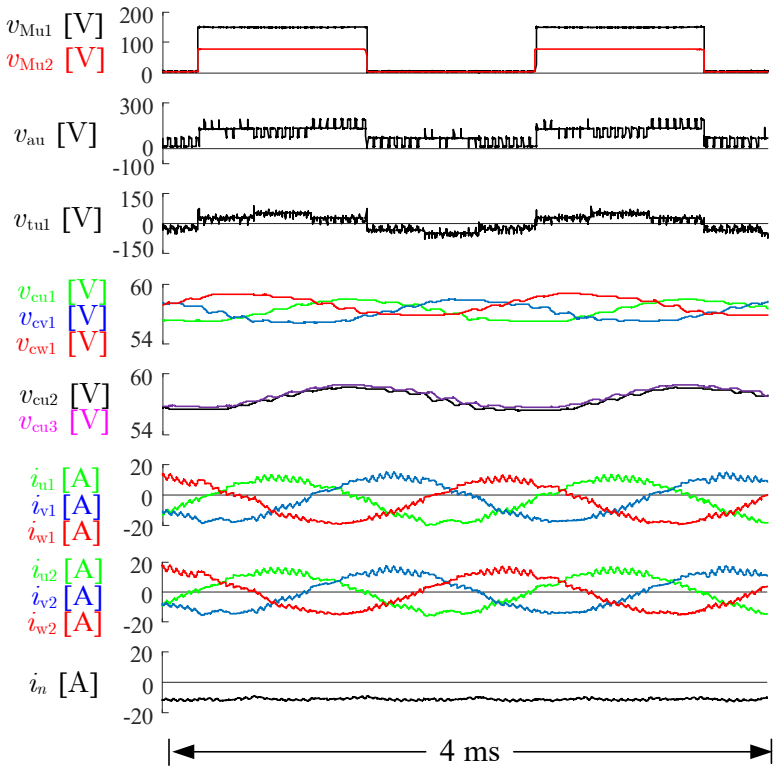

Figure 4-10 Experimental steady-state waveforms using fixed duty ratio when $n\gamma = 0.5$ and $I_{ac}^{*} = +15$ A .

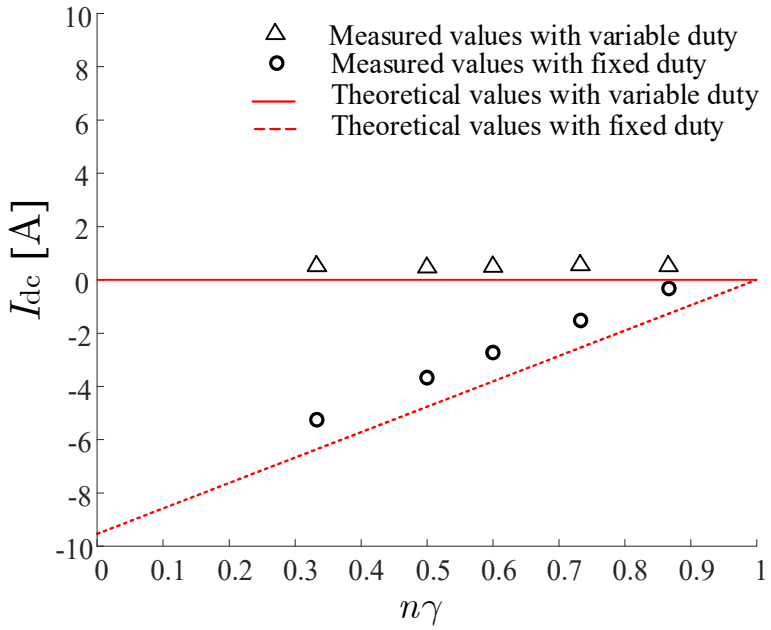

Figure 4-11 Theoretical and experimental DC currents in each phase current of CC DC-DC converter when $I_{ac}^{*} = +15$ A .

NPW-CC DC-DC converter applying the variable duty ratio, with the same $n\gamma$ and I_{ac}^{*} in Figure 4-7 and Figure 4-8. In these experiments, V_c was set at 70 V.

It is observed from Figure 4-9 and Figure 4-10 that the duty ratio of v_{Mu1} was increased from 0.5 as introduced in TABLE II. In addition, the waveforms of v_{au} depicted in Figure 4-9 and Figure 4-10 have higher average and peak voltages than those demonstrated in Figure 4-7 and Figure 4-8, which proves that the variable-duty method requires a higher V_{c} compared with the fixed-duty method, as mentioned in Section 4.3. Meanwhile, the DC-capacitor voltages of the choppers are always kept at 70 V in both Figure 4-9 and Figure 4-10, which validates the effectiveness of the feedback control system shown in Figure 4-6. Furthermore, the DC current flowing in the neutral point of the transformer (i_n) was significantly reduced compared with those in Figure 4-7 and Figure 4-8. In Figure 4-9 where $m\gamma$=0.75, a DC current of $+0.56$ A is superimposed on each primary-side current, while in Figure 4-10 where $m\gamma$=0.5, a DC current of $+0.50$ A is superimposed on each primary-side current. It should be noted that a non-zero DC current still exists in both Figure 4-9 and Figure 4-10 due to unavoidable disturbances such as power losses in the transformer.

Figure 4-11 shows the theoretical and experimental DC current of each phase current. It can be confirmed from Figure 4-11 that the experimental DC

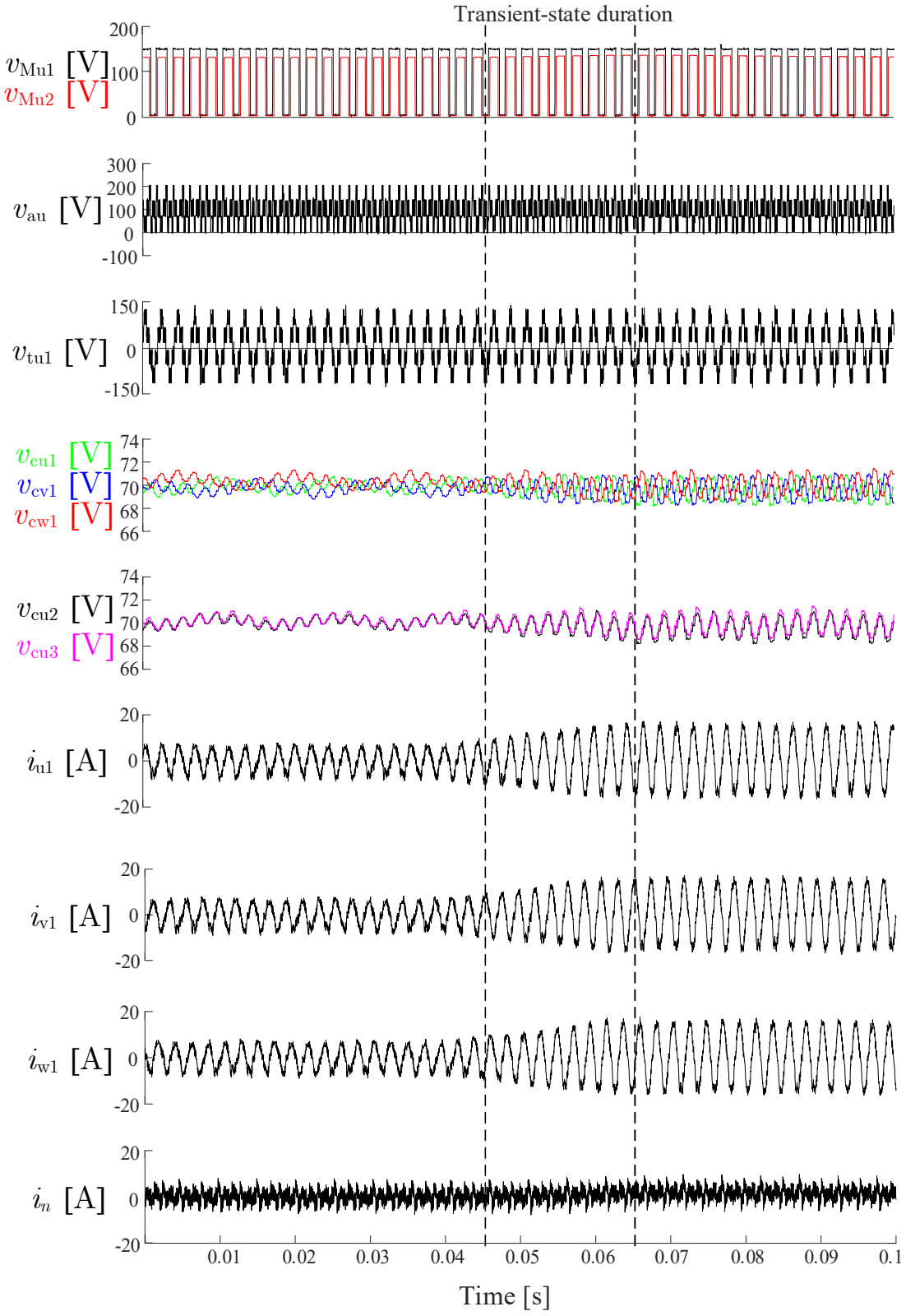

Figure 4-12 Experimental transient-state waveforms using new method when $n\gamma = 0.85$ and I_{dc}^{*} varies from $+5$ A to $+15$ A .

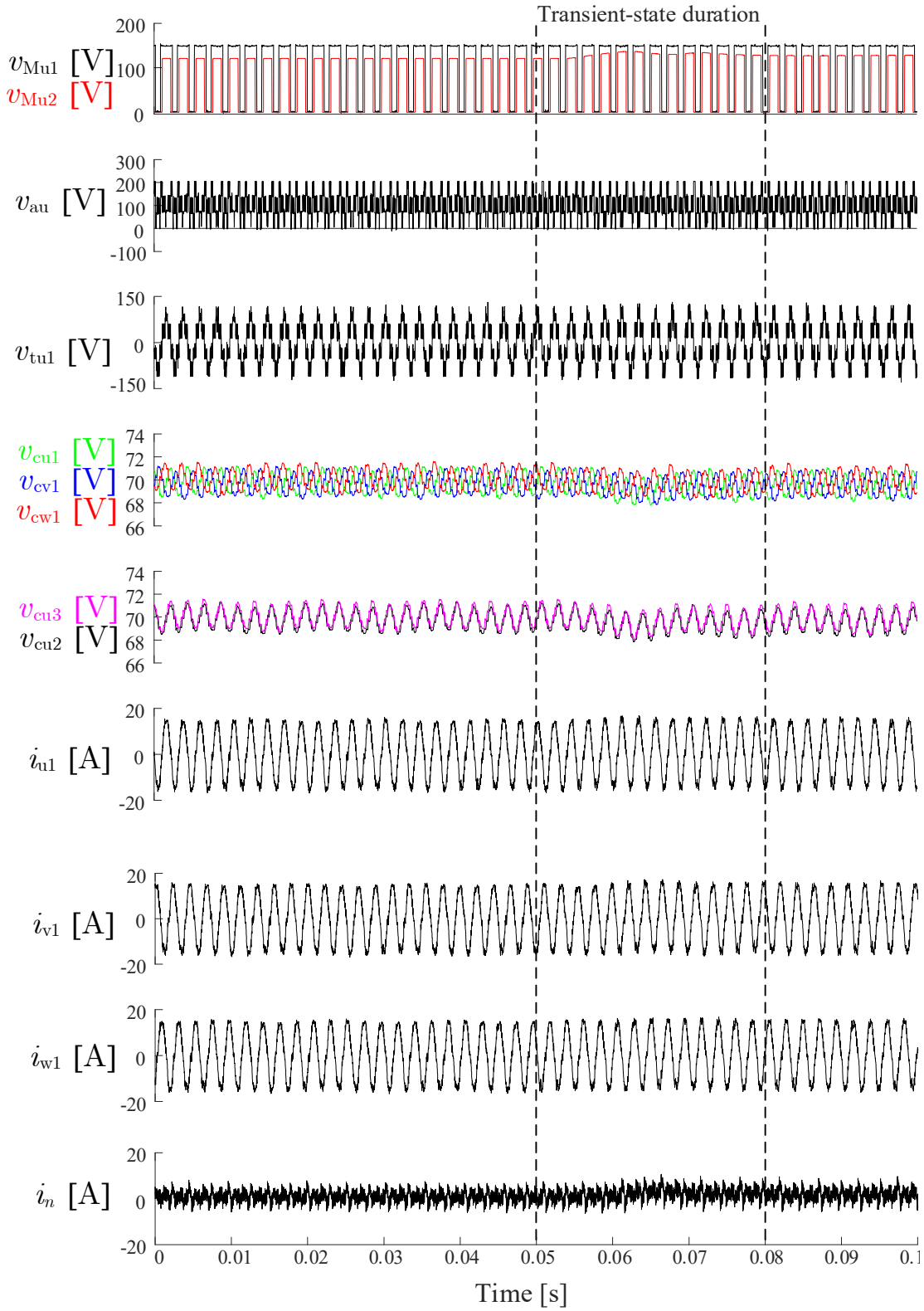

Figure 4-13 Experimental transient-state waveforms using new method when $I_{ac}^{*} = +15$ A and V_{dc2} varies from 120 V to 130 V.

current when the fixed duty ratio is applied presents a linear relationship to $n\gamma$, which matches with the theoretical values calculated from (3.16). Furthermore, the experimental DC current when the variable duty ratio is applied is consistently close to the theoretical value of zero.

Consequently, the experimental waveforms shown in Figure 4-9 and Figure 4-10 validate the feasibility of the variable-duty method. It is confirmed from Figure 4-11 that this strategy can effectively reduce the zero-sequence DC current. Since the AC fundamental components of the primary-side phase currents are the same in amplitude ($= +15$ A) between new and old methods, the peak current of the phase currents when variable duty ratio is applied is smaller than that when fixed duty ratio is applied as shown in Figure 4-7 and Figure 4-8, which verifies the reduction effect of peak current simultaneously.

Transient-State Experiments

To further verify the feasibility of the variable-duty method, two transient-state experiments were carried out: Figure 4-12 shows the transient-state experimental results when $n\gamma = 0.85$ and I_{ac}^{*} was changed from $+5$ A to $+15$ A; Figure 4-13 shows another transient-state experimental results when $I_{\text{ac}}^{*} = +15$ A and V_{dc2} was changed from 120 V to 130 V. It should be noted that V_{dc1} was set to 150 V in both transient-state experiments.

In Figure 4-12, the transient-state response starts from 0.045 ms and ends at 0.065 ms. It can be confirmed that the amplitude of inductor current in each phase is regulated from $+5$ A to $+15$ A with good accuracy. Meanwhile, the DC-capacitor voltages, e.g., v_{cu1}, v_{cu2}, and v_{cu3} are always kept at 70 V. The entire transient-state response is completed within 20 μs and the zero-sequence DC current (i.e., i_n) is always close to zero.

In Figure 4-13, the transient-state response starts from 0.05 ms and ends at 0.08 ms. Since V_{dc2} is changed from 120 V to 130 V, a corresponding voltage rise of v_{Mu2} can be observed in the transient-state duration. It can be confirmed from the results of Figure 4-13 that the inductor current is well-tracked with an amplitude of $+15$ A and the DC-capacitor voltages are always kept at 70 V. The whole transient-state response is completed very fast (within 30 μs) and stably, although a slight overshoot exists in the transient-state duration.

According to the experimental results of Figure 4-12 and Figure 4-13, the dynamical performance of the NPW-CC DC-DC converter when variable duty

ratio is applied is initially validated.

4.7 Conclusion

This Chapter presents new operating principles for the NPW-CC DC-DC converter based on variable duty ratios. The new operating principles can eliminate the DC zero-sequence current in the primary side and can decrease the peak and RMS currents, especially when $m\gamma$ is far from one. By applying this variable-duty method, the voltage harmonic distortion is increased while the current harmonic distortion is reduced to zero. Thus, although the total power factor (PF_{ot}) becomes even lower, the RMS and peak currents of the NPW-CC DC-DC are successfully further reduced. Although the theoretical calculated efficiency is not significantly improved, the huge peak-current reduction effect can help decrease size and saturation risk of the inductor and transformer.

The new operating principles, including steady-state and transient-state response, have been validated using a 150 V, 2.5 kW downscaled model. Finally, the DC zero-sequence current reduction effect has also been verified with the experiments.

Chapter 5 Other Types of Cascaded-Converters DC-DC Converters

In the previous two Chapters, the most basic type of cascaded-converters DC-DC converter—NPW-CC DC-DC converter has been introduced, including operating principles using fixed duty ratio and an improvement method to eliminate zero-sequence current using variable duty ratio. However, since the NPW-CC DC-DC converter uses cascaded choppers as the auxiliary converter, there is another issue which neither method can resolve well: the power limitation caused by overmodulation in the cascaded choppers. This Chapter focuses on the overmodulation phenomenon and tries to address this issue by using other types of cascaded-converters DC-DC converters.

5.1 Basis of Overmodulation

Before the discussion of the power limitation, the basis about overmodulation is introduced in this Section. Figure 5-1 shows the principles of overmodulation in a chopper. Figure 5-1(a) shows the circuit topology of a HB chopper and Figure 5-1(b) shows the principles of generating PWM signals. It is well-known that PWM signal is generated by comparing reference voltage with carrier voltage. Generally, the carrier is a periodic triangular waveform that varies from 0 to V_{dc}. When the reference voltage is higher than the carrier voltage, the high-side power switch is turned on. When the reference voltage is lower than carrier voltage, the high-side power switch is turned off.

In this context, overmodulation is defined as the phenomenon where a HB chopper continuously outputs "0" or "1" (i.e., V_{dc} in Figure 5-1) over multiple cycles, as shown in Figure 5-1(b). This phenomenon occurs when the modulation index M_{I} which is defined as

$$M_{\mathrm{I}} = \frac{\left|v_{\mathrm{r}}\right|}{V_{\mathrm{dc}}}. \tag{5.1}$$

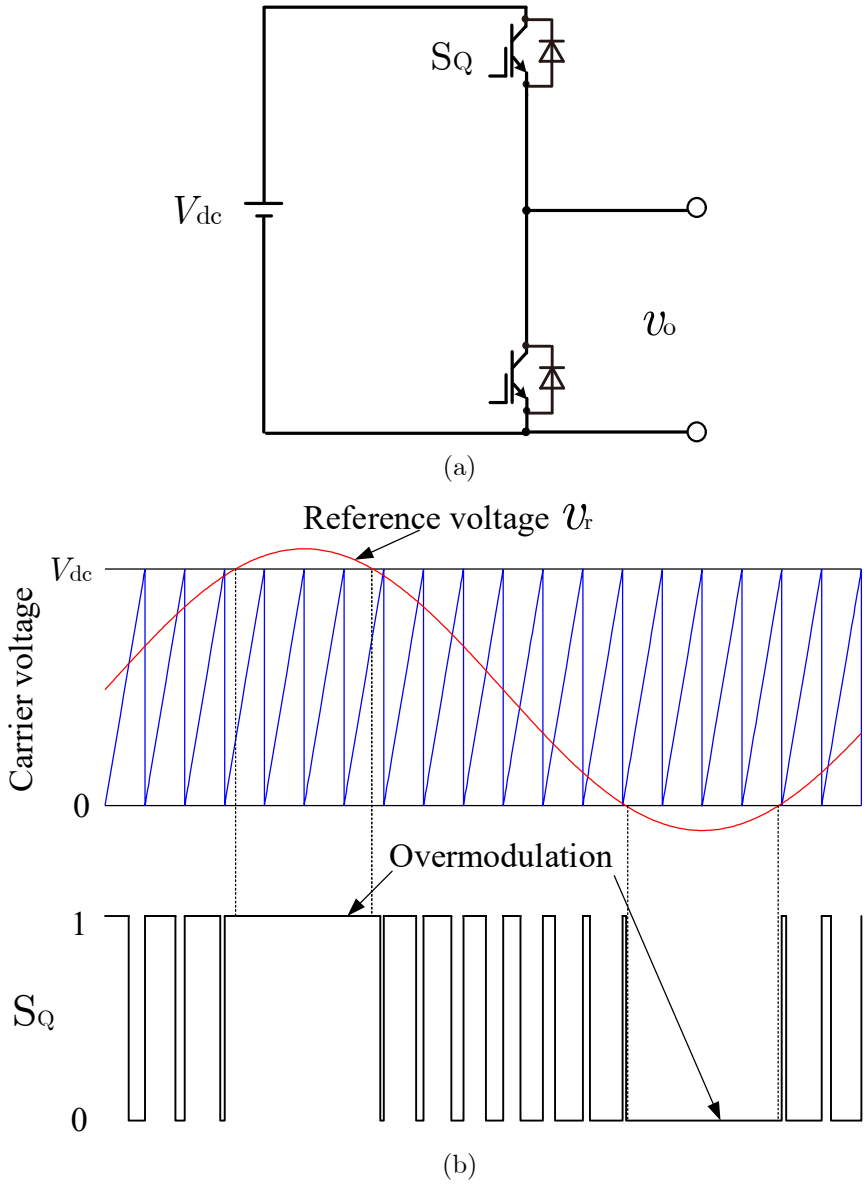

Figure 5-1 Principles of overmodulation. (a) Typical half bridge chopper; (b) PWM waveform of choppers.

is greater than 1 or less than 0. The overmodulation makes the chopper out of control and makes the output nonlinear. Therefore, in most cases, overmodulation in the circuit is not allowed.

5.2 Overmodulation in Cascaded Choppers

Since the NPW-CC DC-DC converter employes cascaded choppers to control the power flow and to reduce the RMS and peak currents, overmodulation may occur in the auxiliary converter. Specifically, the overmodulation occurs when the reference voltage of the auxiliary converter is higher than the total

DC-capacitor voltage or lower than that. It can also be expressed as

$$M_{\mathrm{I}} < 0\,, \tag{5.2}$$

or

$$M_{\mathrm{I}} > 1\,, \tag{5.3}$$

where the modulation index M_{IU} (for u-phase auxiliary converter) is defined as

$$M_{\mathrm{IU}} = \frac{v_{\mathrm{au}}}{\sum_{x=1}^{N} v_{\mathrm{cu}x}}\,. \tag{5.4}$$

According to the feedback control introduced in Section 3.4, the voltage of each DC-capacitor $v_{\mathrm{cu}x}$ should be kept at V_{c}. In addition, v_{au} contains two parts, $\left(v_{\mathrm{au}}\right)_x$ and $\left(v_{\mathrm{au}}\right)_y$, which is given by (3.9). Thus, the overmodulation can be re-written as

$$M_{\mathrm{IU}} = \frac{\left(v_{\mathrm{au}}\right)_x + \left(v_{\mathrm{au}}\right)_y}{NV_{\mathrm{c}}} < 0\,. \tag{5.5}$$

or

$$M_{\mathrm{IU}} = \frac{\left(v_{\mathrm{au}}\right)_x + \left(v_{\mathrm{au}}\right)_y}{NV_{\mathrm{c}}} > 1\,. \tag{5.6}$$

It can be known from (5.5) and (5.6) that the denominator of M_{IU} is a constant determined by N and V_{c}. The numerator, however, consists of two parts: $\left(v_{\mathrm{au}}\right)_x$, which is a fixed waveform determined by V_{dc1} and $n\gamma$; and $\left(v_{\mathrm{au}}\right)_y$, which is a waveform determined by the current magnitude, frequency, and inductance value as in (3.12).

In the NPW-CC DC-DC converter, the value of V_{c} can be dynamically adjusted using the feedback control system. Therefore, the overmodulation pattern of (5.6) can be avoided by ensuring that V_{c} is sufficiently high. However, the overmodulation mode in (5.5) cannot be avoided by adjusting V_{c}. Hence, this Chapter mainly focuses on discussing how to avoid the latter, i.e., the following case:

$$\min\left\{\frac{\left(v_{\mathrm{au}}\right)_x + \left(v_{\mathrm{au}}\right)_y}{NV_{\mathrm{c}}}\right\} < 0 \quad \text{or} \quad \min\left\{\left(v_{\mathrm{au}}\right)_x + \left(v_{\mathrm{au}}\right)_y\right\} < 0\,. \tag{5.7}$$

In Section 4.3, $\left(v_{\mathrm{au}}\right)_x$ has been given by (4.12) as

$$\left(v_{\mathrm{au}}\right)_x = v_{\mathrm{Mu1}} - v_{\mathrm{tu1}} = \mathrm{S}_{\mathrm{Q1}} V_{\mathrm{dc1}} - \left(\frac{2}{3}\mathrm{S}_{\mathrm{Q7}} - \frac{1}{3}\mathrm{S}_{\mathrm{Q8}} - \frac{1}{3}\mathrm{S}_{\mathrm{Q9}}\right) n\gamma\,. \tag{5.8}$$

Meanwhile, since a sinusoidal current given by (3.13) is desired, $\left(v_{\mathrm{au}}\right)_y$ can be calculated as

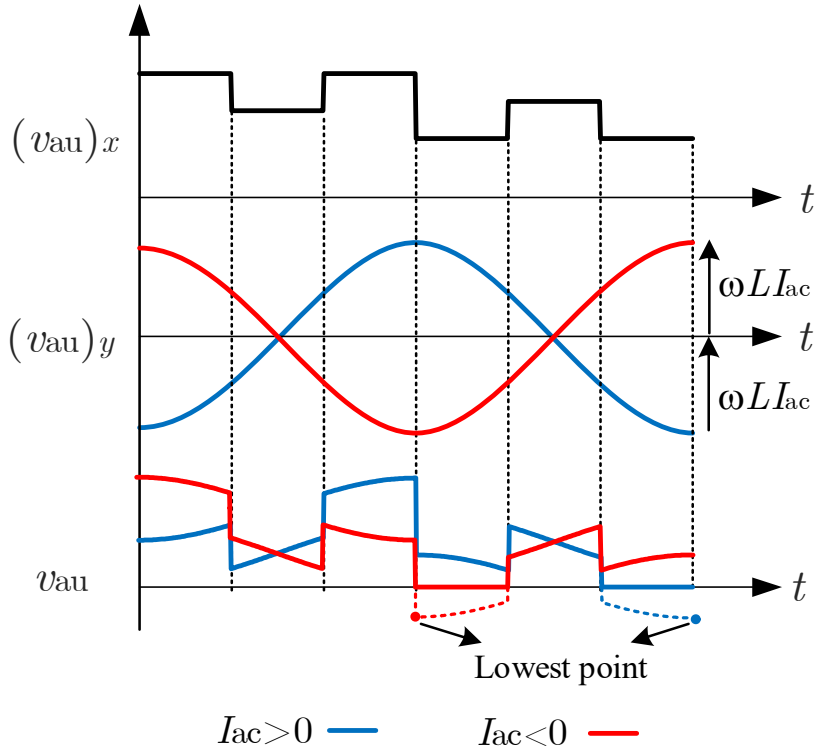

Figure 5-2 Overmodulations in NPW-CC DC-DC converter.

$$\left(v_{\text{au}}\right)_y = -\omega L I_{\text{ac}} \cos\left(\omega t\right). \tag{5.9}$$

Substituting (5.8) and (5.9) into (5.7) yields the condition for overmodulation as

$$\min\left\{\text{S}_{\text{Q1}} V_{\text{dc1}} - \left(\frac{2}{3}\text{S}_{\text{Q7}} - \frac{1}{3}\text{S}_{\text{Q8}} - \frac{1}{3}\text{S}_{\text{Q9}}\right) n\gamma - \omega L I_{\text{ac}} \cos\left(\omega t\right)\right\} < 0\,. \tag{5.10}$$

The overmodulation occurs in the NPW-CC DC-DC converter if the minimum point of v_{au} is lower than zero, as shown in Figure 5-2. It can be observed that due to the symmetry of the waveform, overmodulation is independent of the current direction (i.e., the sign of I_{ac}). In (5.10), typically, V_{dc1}, f_{s1}, L, and other variables are fixed. Thus, it can be inferred that the minimum value of v_{au} is negatively correlated with $n\gamma$ and I_{ac}, simultaneously. This means that when one variable ($n\gamma$ or I_{ac}) increases, the other must decrease correspondingly. In fact, this is indeed the case. Figure 5-3(a) and (b) respectively show the maximum current and maximum power of the NPW-CC DC-DC converter at a certain $n\gamma$ without overmodulation. It can be observed that when $n\gamma$ is relatively large, the NPW-CC DC-DC converter loses its power transmission capability whatever fixed-duty method or variable-duty method is applied. Additionally, although unrelated to this Chapter, Figure 5-3 also shows that the variable-duty method has a larger capacity when $n\gamma < 1$, while the fixed-duty

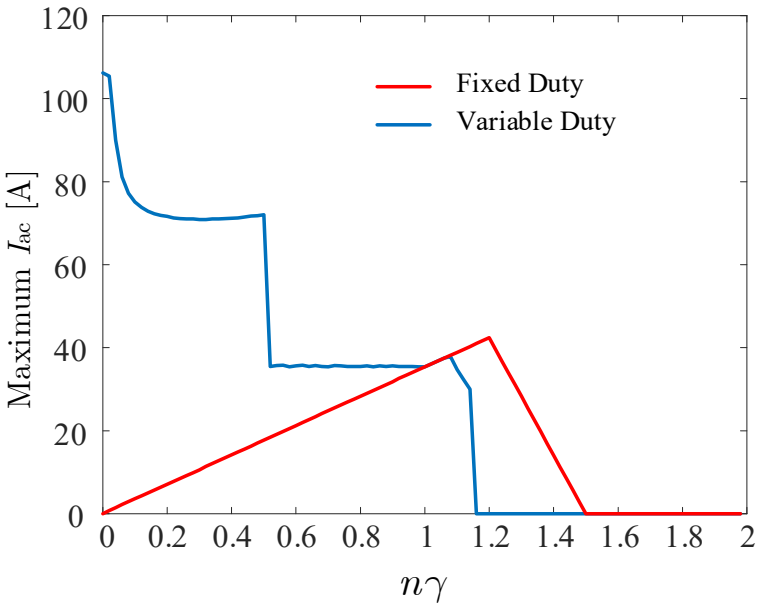

(a)

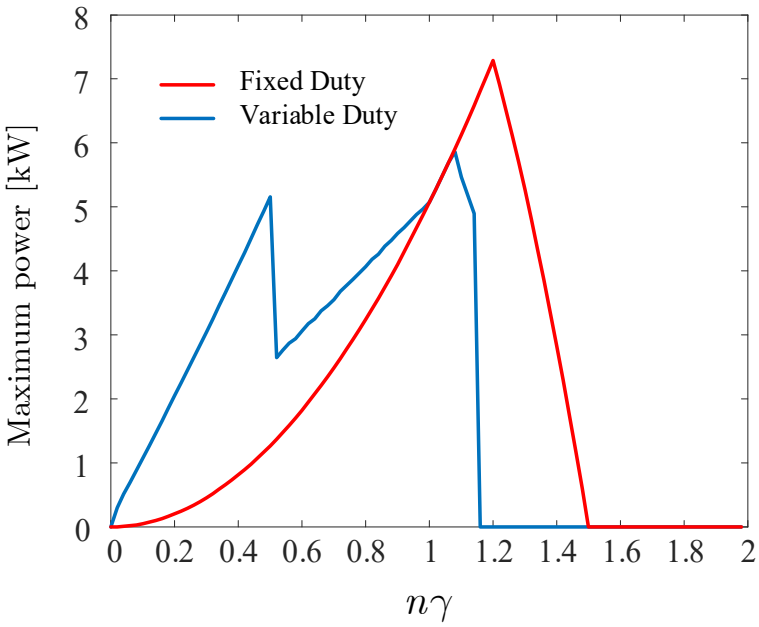

(b)

Figure 5-3 Maximum (a) current and (b) power of NPW-CC DC-DC converter without over-modulation in auxiliary converter using the model of Section 3.6.

method has a larger capacity when $n\gamma > 1$. Therefore, for some specific applications, the maximum output power of the NPW-CC DC-DC converter can be matched through appropriate control algorithm.

5.3 NNPW-CC DC-DC Converter

Circuit Configuration and Basic Operations

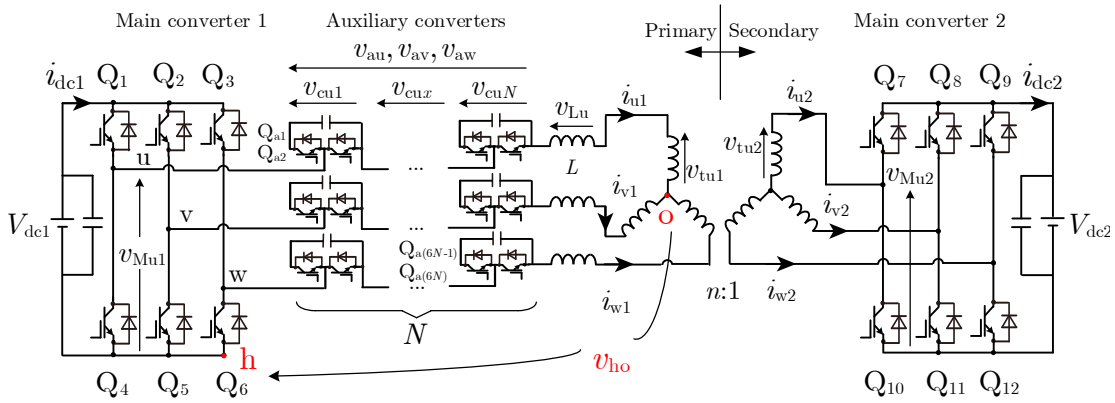

Figure 5-4 Circuit configuration of the NNPW-CC DC-DC converter with a Yn-Y transformer (using IGBTs).

The simplest method to avoid overmodulation is using NNPW-CC DC-DC converter instead of NPW-CC DC-DC converter. The circuit topology of NNPW-CC DC-DC converter is shown in Figure 5-4, and it is very similar to that of the NPW-CC converter, with the primary difference being the absence of a neutral point wire. The specific classification method has already been explained in Section 2.5.2. Nevertheless, the operating principles of the NNPW-CC DC-DC converter differ significantly from those of the basic type (NPW-CC).

The biggest difference between them is the floating voltage, i.e., v_{ho}. In the basic type, due to the presence of the neutral line, the floating voltage v_{ho} is always equal to zero. However, in the NNPW-CC type, the floating voltage is not equal to zero and the KVL equation becomes as

$$v_{Mu1} + v_{ho} = v_{tu1} + v_{au} + v_{Lu} , \tag{5.11}$$

where v_{ho} is a common-mode voltage components of u, v, and w phases. Typically, in a three-phase circuit, DC voltage and third-series harmonic voltages (3^{rd}, 6^{th}, 9^{th}, etc.) are considered as the components of the common-mode voltage. Among these, since generating third-series harmonics is significantly more challenging than generating DC, this dissertation considers DC as the common-mode voltage for the NNPW-CC type converter.

Applying the same treatment to equation (5.11) as was done for (3.8) and (3.9), the following equation is obtained:

$$\begin{aligned} v_{au} &= \left(v_{Mu1} - v_{tu1}\right) + v_{ho} + \left(-v_{Lu}\right) \\ &= \left(v_{au}\right)_x + v_{ho} + \left(v_{au}\right)_y \end{aligned} . \tag{5.12}$$

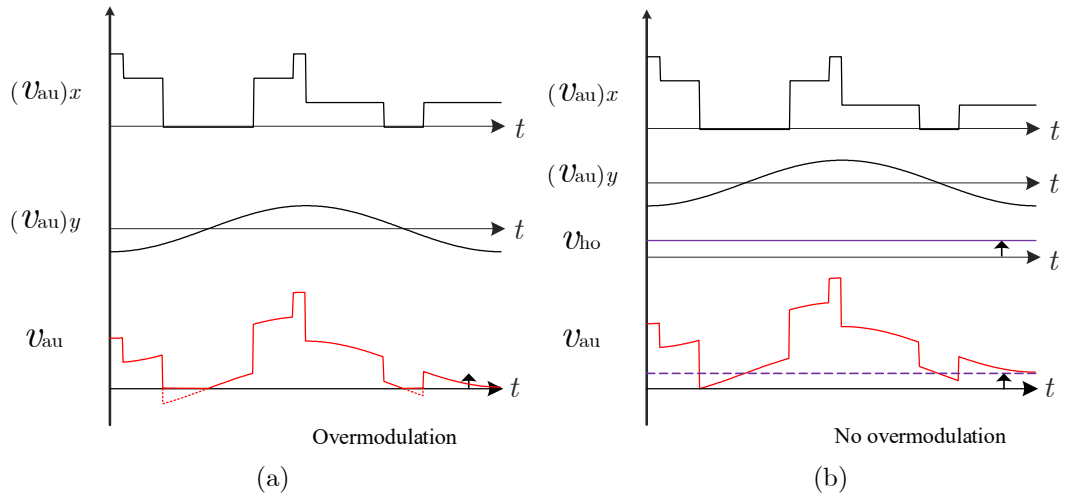

Figure 5-5 Simplified waveforms (a) with negative voltage in v_{au}; (b) using floating voltage to raise v_{au}.

The new auxiliary converter voltage (v_{au}) contains $(v_{au})_x$, $(v_{au})_y$, and an additional component v_{ho}. The common-mode voltage can actively raise v_{au}, ensuring that v_{au} remains entirely above zero, subsequently avoiding overmodulation in the auxiliary converter.

Figure 5-5(a) shows the typical waveforms when the auxiliary converter is overmodulated, while Figure 5-5(b) shows the simplified waveforms illustrating how the DC floating common-mode voltage v_{ho} raises v_{au} to avoid overmodulation. It should be noted that this method may increase the maximum value of v_{au}, which means a higher V_c is required.

Variable-Duty Operations

Since the NNPW-CC DC-DC converter does not have a neutral point wire, zero-sequence current is not allowed. Therefore, the fixed-duty operation described in Chapter 3 cannot be applied to the modified converter. As a result, the NNPW-CC DC-DC converter needs to adopt the variable-duty method described in Chapter 4. Meanwhile, except for the inclusion of an additional DC voltage in $\left(v_{au}\right)_x$, the remaining operating principles are the same as those in Chapter 4.

Block Diagram of Control System

Due to the absence of neutral current, the control system of the circuit is slightly different. First, instead of directly controlling the AC and DC

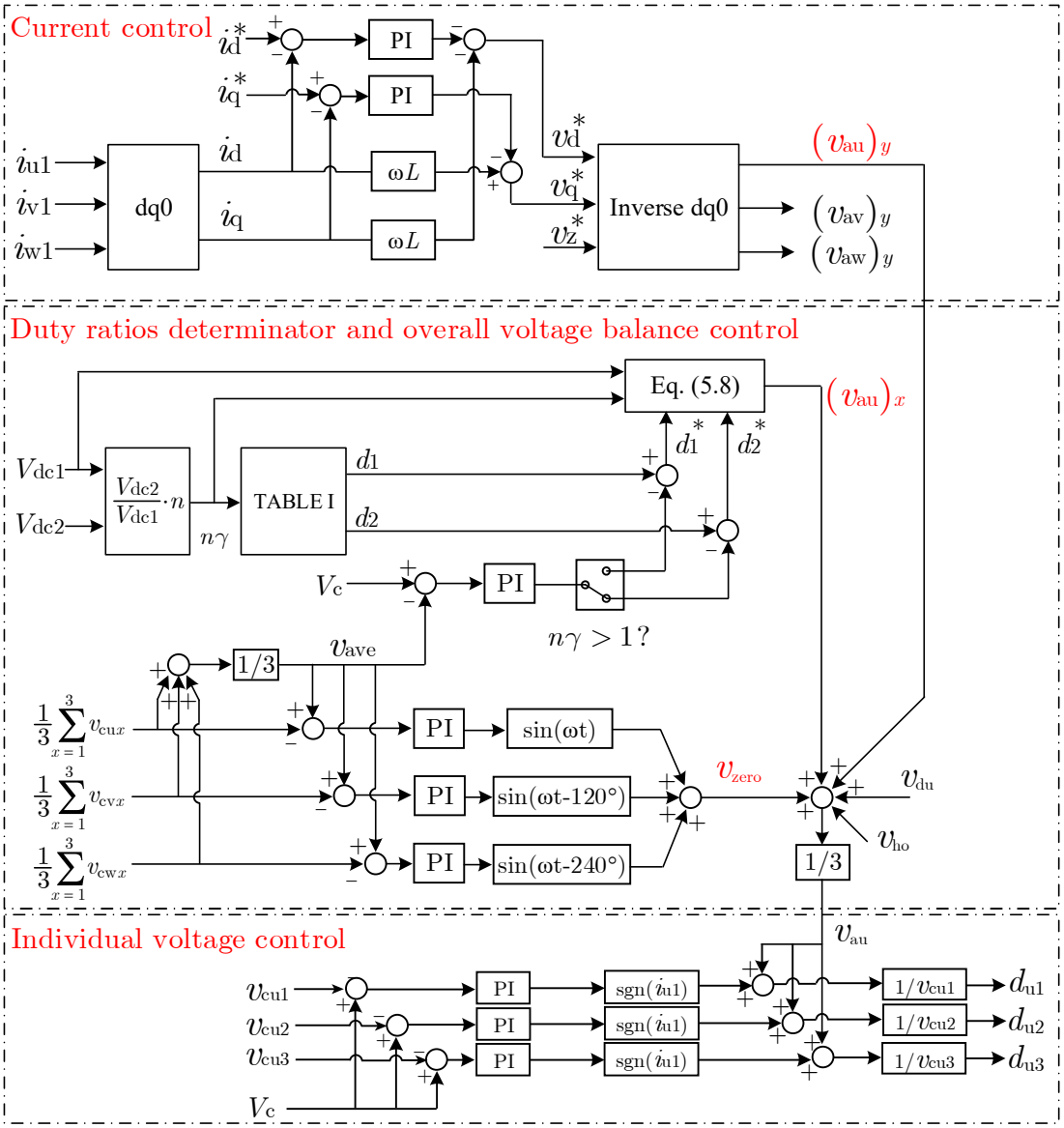

Figure 5-6 Block diagram of control system for NNPW-CC DC-DC converter.

components of the current as in Chapter 3 and Chapter 4, this circuit uses $dq0$ transformation for current control, as shown in Figure 5-6. Since the control plant is the inductor, there is a delay between its voltage and current, needing the following compensation relationship between the reference voltage and reference current:

$$\begin{cases} v_{\mathrm{d}}^{*} = -\omega L i_{\mathrm{q}} - \left(K_p + \dfrac{K_i}{s}\right)\left(i_{\mathrm{d}}^{*} - i_{\mathrm{d}}\right) \\ v_{\mathrm{q}}^{*} = \omega L i_{\mathrm{d}} - \left(K_p + \dfrac{K_i}{s}\right)\left(i_{\mathrm{q}}^{*} - i_{\mathrm{q}}\right) \\ v_{\mathrm{z}}^{*} = 0 \end{cases} . \tag{5.13}$$

This process is similar to the reference current compensation described in Section. 3.4. Besides, it should be noted that although the zero-sequence component v_{z}^{*} is used for voltage balance control, it is set to zero in the current control. This is to avoid coupling between different control loops. $(v_{\mathrm{au}})_y$ (also, $(v_{\mathrm{av}})_y$ and $(v_{\mathrm{aw}})_y$) is the output of the inverse $dq0$ transformation block, which is the opposite of the inductor voltage.

The duty ratio is determined by the same rule listed in TABLE II, Section 4.3. Furthermore, an additional PI controller is used to ensure that the active power of each auxiliary converter is always equal to zero, subsequently keeping the DC-capacitor voltage. However, the average voltages among u, v, and w phases may not achieve balance because they share the same duty ratios (i.e., d_1 and d_2), leading to unresolved individual phase errors. The NNPW-CC DC-DC converter uses zero-sequence voltage to balance the average DC-capacitor voltages between u, v, and w phases. The implementation is as

1) Calculate the error between the average voltage of all DC-capacitors and the average voltage of each phase.
2) The amplitude is calculated by the PI controller.
3) Generate the corresponding sinusoidal waveform with the calculated amplitude.
4) The zero-sequence voltage is the sum of all sinusoidal waveforms.

The operating principle of the zero-sequence voltage is to generate reactive power among phases u, v, and w, enabling the DC capacitors of each phase to charge and discharge each other to achieve balance. The details of the zero-sequence injection are reported in [141].

Moreover, the DC floating voltage v_{ho} is added to prevent overmodulation in the auxiliary converter as mentioned previously. The value of v_{ho} can be arbitrarily set as big as it ensures that the overall value of v_{au} remains greater than zero. However, although setting a high v_{au} can prevent the auxiliary converter from overmodulation, it may also increase the switching losses of power devices. Thus, considering an appropriate floating voltage is necessary. In fact, the theoretical optimal value of v_{ho} can be given by the following equation:

$$\min\left\{v_{\mathrm{ho}}\right\} = -\min\left\{\left(v_{\mathrm{au}}\right)_x - \omega L I_{\mathrm{ac}} \cos\left(\omega t\right)\right\}. \tag{5.14}$$

This optimal floating voltage increases v_{au} when the minimum value is negative

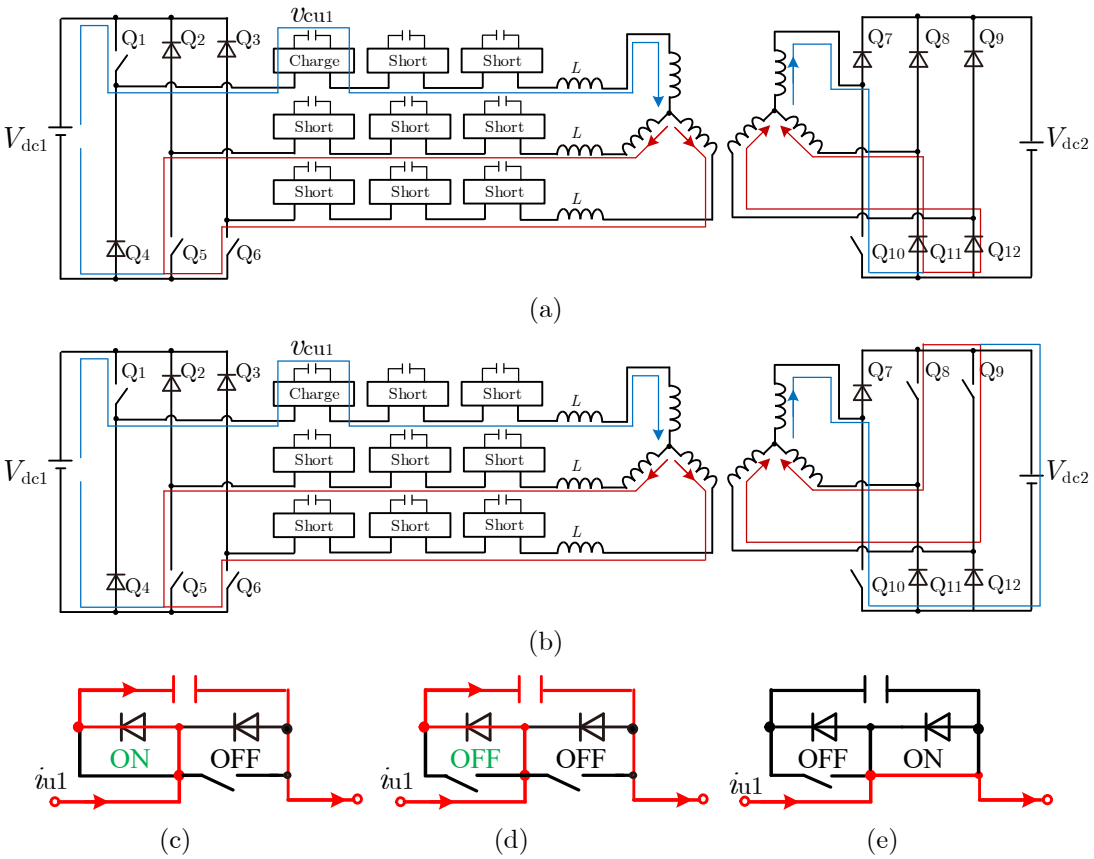

Figure 5-7 Simplified circuit and current flows for (a) low voltage charge mode, (b) high voltage charge mode. (c) charge mode for low voltage charge mode, (d) charge mode for high voltage charge mode, (e) short-circuit mode.

while it decreases v_{au} when the minimum value is naturally positive, which ensures that the minimum value of v_{au} is exactly equal to zero, as shown in Figure 5-5(b). In this way, overmodulation can be avoided, at the same time, the voltage of the DC-capacitors, i.e., V_c, can be minimized, thereby reducing losses to the greatest extent. However, since v_{au} also contains components for voltage control, ripple, and periodic errors, the actual v_{ho} will be larger than the theoretical value to prevent negative voltages.

Finally, the control system of NNPW-CC DC-DC has the same individual DC-capacitor voltage control as the NPW-CC DC-DC converter in Figure 3-8.

Initial Charge for DC-Capacitors

Due to the absence of a neutral point wire, the DC capacitors in the NNPW-CC cannot use the same initial charging method as that in the NPW-CC (i.e., charging group by group). This is because the NPW-CC allows neutral current to serve as the return path for charging current, whereas the NNPW-CC lacks

TABLE III
SWITCHING LOGICS IN INITIAL CHARGE FOR NNPW-CC

Devices	u phase charge	v phase charge	w phase charge
Q_1	d_M	0	0
Q_2	0	d_M	0
Q_3	0	0	d_M
Q_4	0	1	1
Q_5	1	0	1
Q_6	1	1	0
Low voltage charge mode			
Q_7	0	0	0
Q_8	0	0	0
Q_9	0	0	0
Q_{10}	1	1	1
Q_{11}	1	1	1
Q_{12}	1	1	1
High voltage charge mode			
$Q_7 = Q_4$	0	1	1
$Q_8 = Q_5$	1	0	1
$Q_9 = Q_6$	1	1	0
$Q_{10} = Q_1$	d_M	0	0
$Q_{11} = Q_2$	0	d_M	0
$Q_{12} = Q_3$	0	0	d_M

*1 means the power device is on. 0 means the power device is off. d_M means the power device is operated with a duty of d_M.

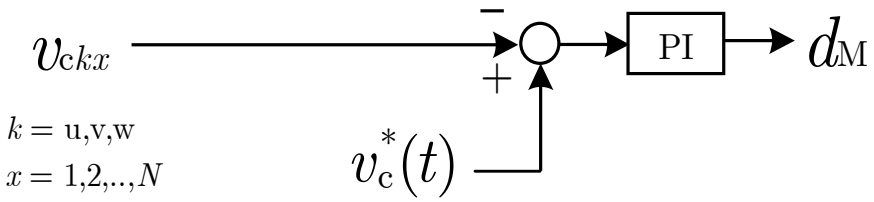

Figure 5-8 Control for initial charge in NNPW-CC DC-DC converter.

a path for neutral current. Therefore, the NNPW-CC requires new methods for initial charging. On the other hand, since the NNPW-CC type may require a higher V_c to generate the floating voltage and avoid overmodulation, therefore, this dissertation provides two charge modes: low voltage charge mode and high voltage charge mode.

[Low voltage charge mode]

In the low voltage charge mode, the DC-capacitors are charged using only V_{dc1}. The simplified circuit for initial charge is shown in Figure 5-7(a). It should

be noted that the words of "Charge" and "Short" marked in the choppers cells correspond to the charge mode in Figure 5-7(c) and the short-circuit mode in Figure 5-7(c). The operating principles can be concluded as follows:

- Although the high-side switch of the cell being charged (e.g., Q_{a1}) is always on-state, no current flows through it since V_c is always less than $V_{dc1.}$ This approach is intended to reduce losses to a certain extent.
- When the cells of u phase are being charged, the low-side switch of u phase (Q_4) remains off, while the high-side switch (Q_1) toggles on and off at a frequency of f_{s1} with a duty ratio of d_M. Meanwhile, the high-side switches of v phase and w phase (Q_2, Q_3) remain off, and the low-side switches (Q_5, Q_6) remain on. When the cells of v phase or w phase are charged, a similar logic is followed, as listed in TABLE III.
- The DC capacitors are charged one by one, following the order of v_{cu1}, v_{cu2}, ..., v_{cw3}, ..., and so on.
- The duty ratio d_M of the high-side switch during cell charging is provided by the control system shown in Figure 5-8. $v_c^*(t)$ is a slope function defined in (3.25), and its slope determines the charging speed.
- When v_{cu1} is being charged, the charging current path is shown in Figure 5-7. The charging current of u phase (blue line) is first transferred to the secondary side, then split into two equal parts (red lines), which return to the primary side via v phase and w phase, and finally flow back to the power source V_{dc1}.

In this mode, all high-side switches (or all low-side switches) of the main converter 2 remain on, which makes the secondary side short-circuited. In the low voltage charge mode, only V_{dc1} is used as the source, hence the highest V_c is equal to V_{dc1} as

$$\max\left\{V_c\right\} = V_{dc1}\,. \tag{5.15}$$

[High voltage charge mode]

In the high voltage charge mode, V_{dc2} is also used for initial charge. The operating principles can be explained using the simplified circuit shown in Figure 5-7(b). It should be noted that the words of "Charge" and "Short" marked in the choppers cells correspond to the charge mode in Figure 5-7(d) and the short-circuit mode in Figure 5-7(c). Since V_c is higher than V_{dc1}, the operating principles are slightly different from those of the low voltage charge mode.

- In this mode, the high-side switch of the cell being charged (e.g., Q_{a1}) is always off-state to avoid the discharging path from DC-capacitor to sources.
- The corresponding low-side switches in the secondary side follows the operation of the high-side switches in the primary side (e.g., $Q_{10} = Q_1$), while the high-side switches in secondary side follows the operation of the low-side switches in the primary side (e.g., $Q_7 = Q_4$), as listed in TABLE III.

Apart from the differences mentioned above, the other operating principles are the same as those of the low-voltage charge mode.

In this mode, the charging current flows through V_{dc2} as shown in Figure 5-7(b), hence a higher V_c can be obtained as

$$\max\left\{V_c\right\} = V_{dc1} + \frac{n}{2}V_{dc2} = \left(1 + \frac{n\gamma}{2}\right)V_{dc1}. \tag{5.16}$$

The NPW-CC type utilizes neutral current for initial charging, and as mentioned in Section 3.1, the transformer employs a three-limb core, ensuring that the neutral current does not influence the flux. However, the NNPW-CC type lacks a neutral point wire, and if the secondary side is open-circuited, all the charging current would flow through the magnetization core, potentially leading to core saturation. Therefore, regardless of the charging mode (low or high), the NNPW-CC type must lead the charging current to the secondary side first and then back to the primary side to prevent core saturation from excessive magnetization current.

Evaluated Efficiency

This Subsection shows a comparison between the TP-DAB converter and NNPW-CC DC-DC converter in terms of conversion efficiency using the same evaluation model used in Section 3.6. Figure 5-9(a) shows the case of $n\gamma = 1.2$, while Figure 5-9(b) shows the case of $n\gamma = 1.4$. As a reference, the conversion efficiency of the NPW-CC type using fixed-duty method is also given in Figure 5-9(a). It can be seen from Figure 5-9(a) that the NPW-CC DC-DC converter using fixed-duty method has the highest conversion efficiency when under full-range load conditions when $n\gamma = 1.2$. Although the NNPW-CC type presents a lower conversion efficiency than NPW-CC type because of higher V_c. Nevertheless, the NNPW-CC type still has comparable efficiency compared to the

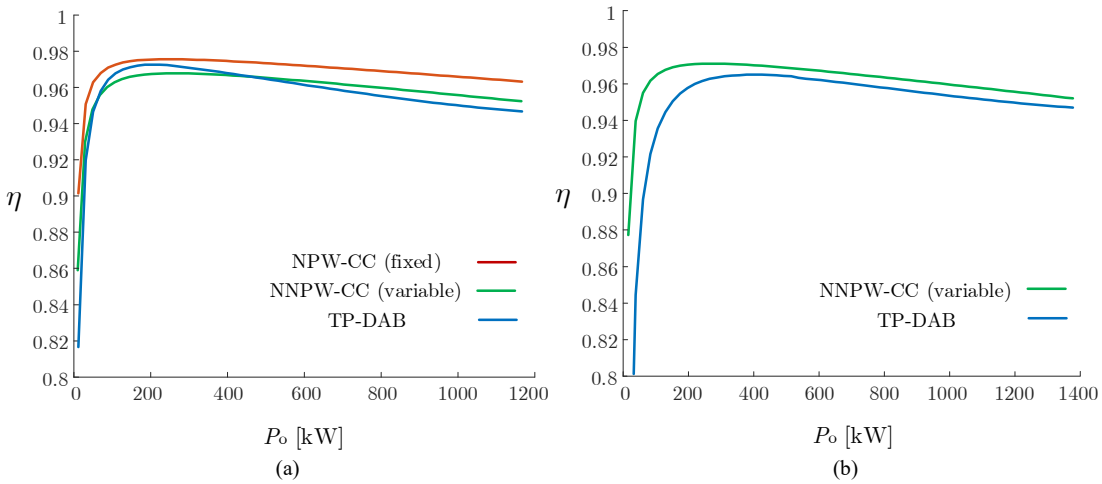

Figure 5-9 Evaluated efficiency when (a) $n\gamma = 1.2$, (b) $n\gamma = 1.4$.

TP-DAB converter, where it presents better except the area of 100-500 kW (around 10%-40% load). When $n\gamma = 1.4$, since the NPW-CC type losses most of output ability, only the NNPW-CC is considered for the comparison. It can be seen from Figure 5-9(b) that the NNPW-CC type presents a higher efficiency than the TP-DAB converter over the entire load range. Therefore, at higher $n\gamma$ values, benefiting for the low RMS current (owing to zero reactive power), the NNPW-CC can still achieve higher conversion efficiency despite using more power components.

Simulation Verifications

The NNPW-CC DC-DC converter is initially verified by computer simulation, which is shown in Figure 5-10. It shows the simulation results of the converter from the beginning of the initial charging phase to the end of the initial charging phase and its transition to steady state. In this simulation, V_{dc1} is set to 150 V; n is set to 2; γ is set to 0.7 (i.e., $n\gamma = 1.4$); L is set to 0.2 mH; V_c is set to 200 V; f_{s1} is set at 450 Hz; f_{s2} is set at 7.2 kHz. Besides, three cascaded choppers ($N = 3$) are employed in each phase. In the initial charge, high voltage charge mode is used and charging speed is set to 2000 V/s. In the steady state, i_d^* is set to +20 A.

Figure 5-10 shows that the converter transition from initial charge to steady state. It can be observed that the DC capacitors are charged one by one to 200V. It can be observed that the charging current in the simulation is very large. This is because the computational capacity (the PC) is limited, requiring a shorter simulation duration; therefore, the charging speed was set very high

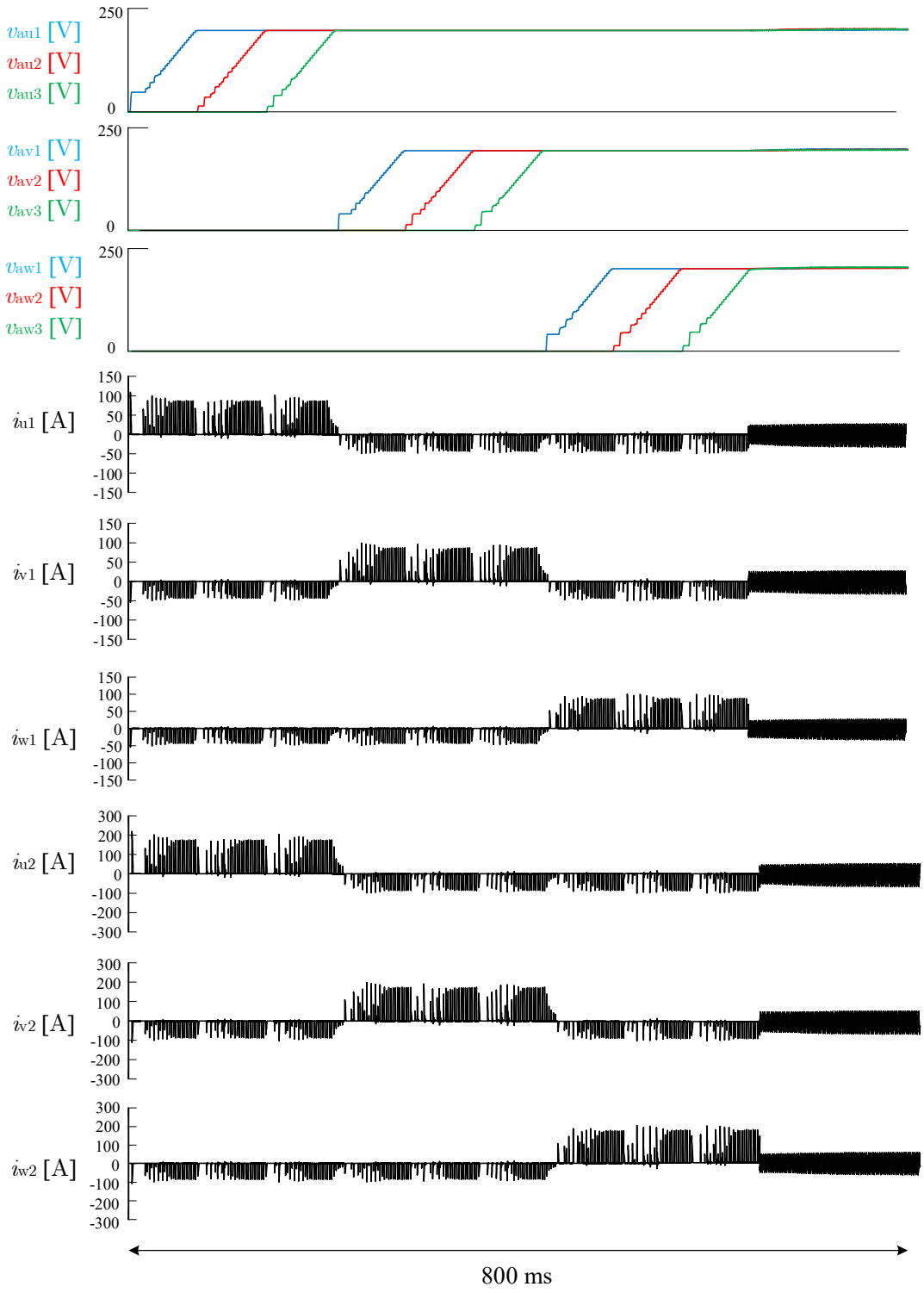

Figure 5-10 Simulation results of NNPW-CC DC-DC converter, from initial charge to steady state.

(2000 V/s). In practical applications, the charging speed can be set much slower to reduce the charging current. Additionally, the charging current goes to the secondary side then is split into two equal parts, as described previously. Once all DC capacitor voltages reach V_c, the converter enters steady state, and the

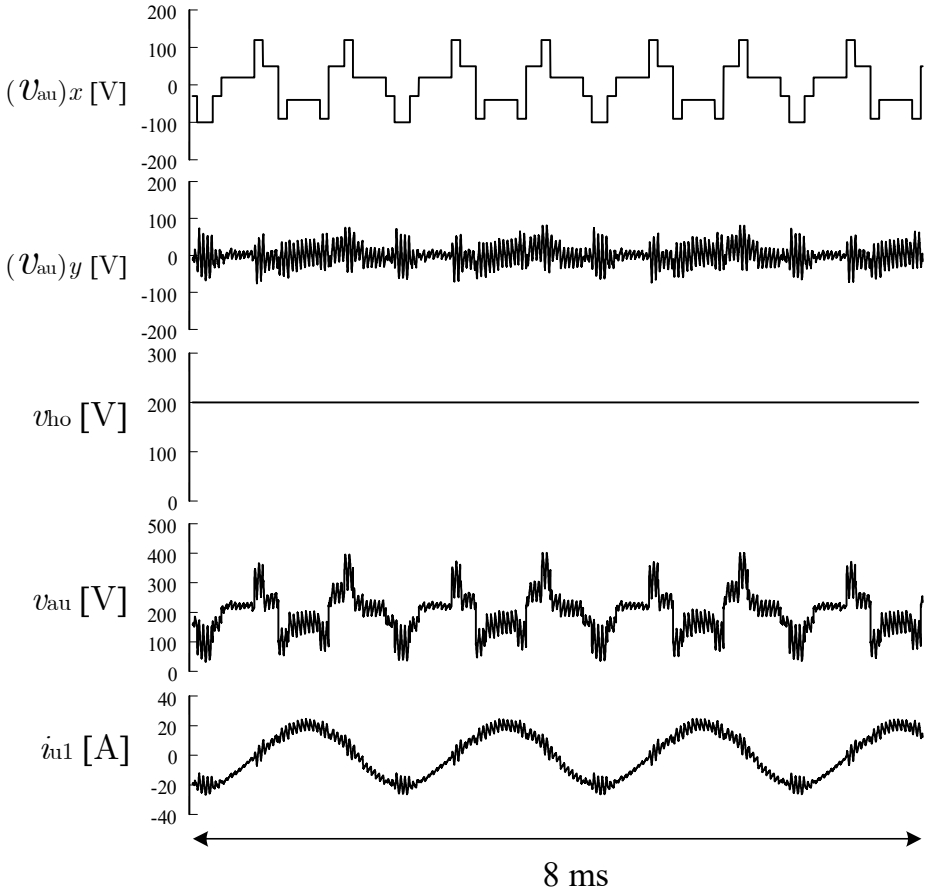

Figure 5-11 Steady-state simulation results of NNPW-CC DC-DC converter.

control system shown in Figure 5-6 begins to work. It can be overserved that the DC-capacitors voltages are well controlled at V_c, which proves the effectiveness of the control system. Figure 5-11 shows the detailed waveforms of the steady-state simulation results. The current is controlled as a sine wave with an amplitude of 20 A, and no DC current is superimposed on i_{u1}, which proves that the variable-duty method works properly. Then, a 200 V floating voltage v_{ho} is added to v_{au} to avoid the overmodulation. According to the description of Section 5.1, when the variable-duty method is applied, overmodulation occurs if $n\gamma > 1.15$. However, no overmodulation occurs in Figure 5-11, although $n\gamma$ is equal to 1.4.

The simulation results confirm that the NNPW-CC DC-DC converter indeed does not face the risk of overmodulation. However, it can be observed that the peak voltage of v_{au} reaches approximately 400 V, which means that each cascaded chopper requires at least 133 V of DC voltage. As $n\gamma$ increases, this voltage will become even higher, implying greater switching losses, higher-rated

power devices, or more chopper cells.

The purpose of this Chapter is to explain the basic operating principles of the NNPW-CC DC-DC converter and how it avoids overmodulation. Understanding these principles is crucial for introducing the two subsequent converters: NPW-CF type and NNPW-CF type.

5.4 NPW-CF DC-DC Converter

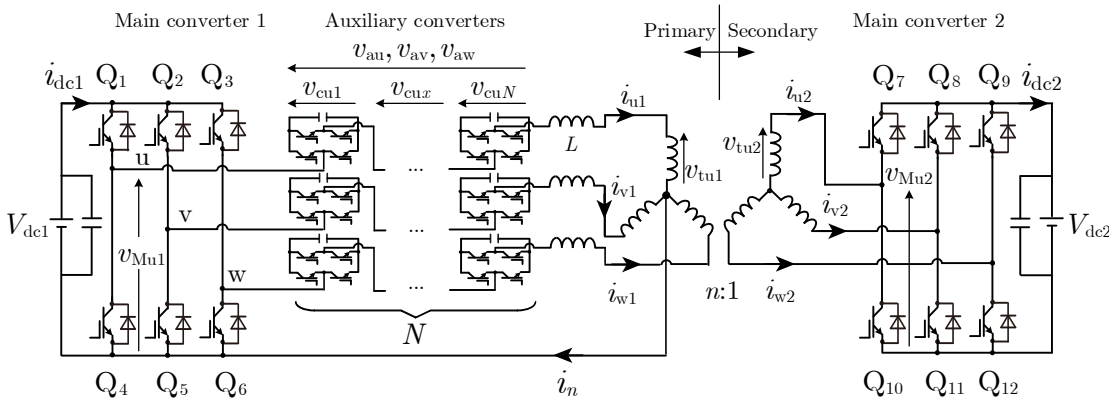

Figure 5-12 Circuit configuration of the NPW-CF DC-DC converter with a Yn-Y transformer (using IGBTs).

Figure 5-12 shows the circuit topology of the NPW-CF DC-DC converter. Apart from replacing the cascaded choppers with cascaded full bridges, the circuit structure is identical to that of the NPW-CC type. Additionally, except for the PWM output method used by the full bridge, the operating principles of the circuit are also the same. The NPW-CF type can also use both fixed-duty and variable-duty methods. Similarly, using variable-duty method can reduce the DC current but may increase the required voltage in the DC-capacitor (i.e., V_c). Therefore, the choice of method depends on the specific circumstances.
The biggest difference between NPW-CC type and NPW-CF type is the PWM generation. It is well-known that full bridge uses bipolar PWM while chopper uses unipolar PWM. Unipolar PWM means the PWM waveform is generated using a unipolar carrier, which is shown in Figure 5-1(b). Hence, bipolar PWM means the PWM waveform is generated using a bipolar carrier, which is shown in Figure 5-13. The full bridge has two sets of switching signals that share a single bipolar carrier. The reference voltage v_{r1} for the first set of switching signals (S_{Q1}) and the reference voltage v_{r2} for the second set of switching signals (S_{Q2}) satisfy the following relationship:

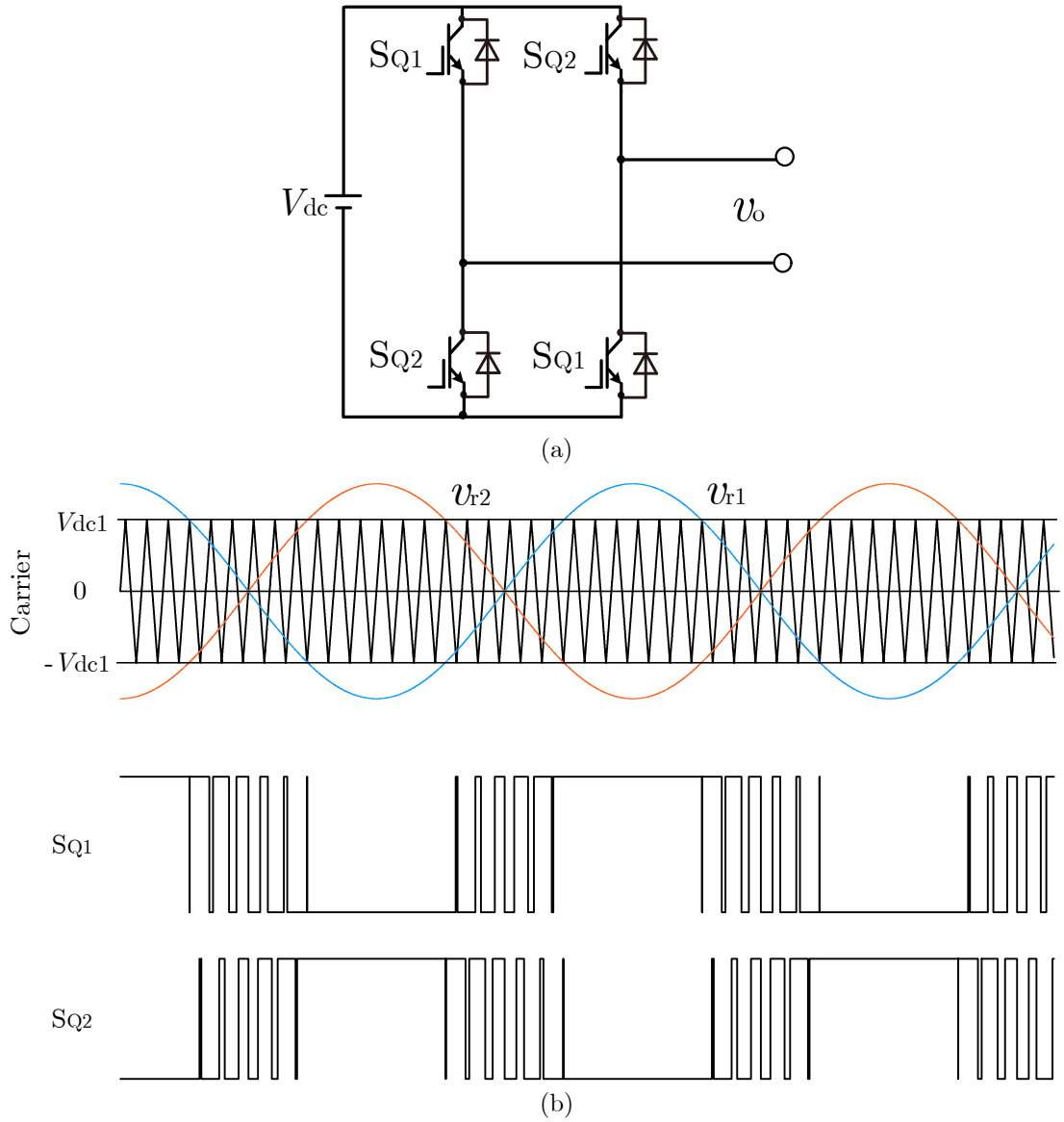

Figure 5-13 Principles of overmodulation. (a) Typical full bridge; (b) Bipolar PWM waveform for full bridge.

$$v_{r1} = -v_{r2}\,. \tag{5.17}$$

In the full bridge, the modulation index is still defined as:

$$M_I = \frac{|v_{r1}|}{V_{dc1}} \quad \text{or} \quad M_I = \frac{|v_{r2}|}{V_{dc1}}. \tag{5.18}$$

However, unlike the half-bridge chopper, the full bridge allows the modulation index to be negative. Overmodulation occurs only when the modulation index is greater than 1. Due to this characteristic, the overmodulation shown in Figure 5-2 no longer occurs. As long as V_c is sufficiently high, the NPW-CF type theoretically has no voltage conversion ratio or current limitations.

Finally, cascaded full bridges using bipolar PWM can achieve an equivalent

frequency that is twice that of cascaded choppers using unipolar PWM. For instance, N cascaded full bridges with a switching frequency of f_{s2} can achieve an equivalent frequency of $2Nf_{s2}$ through PS-PWM, whereas the same number and frequency of cascaded choppers can only achieve an equivalent frequency of Nf_{s2}. Nevertheless, full bridges require twice the number of switches compared to choppers, so the specific circuit configuration should be determined based on application requirements.

5.5 NNPW-CF DC-DC Converter

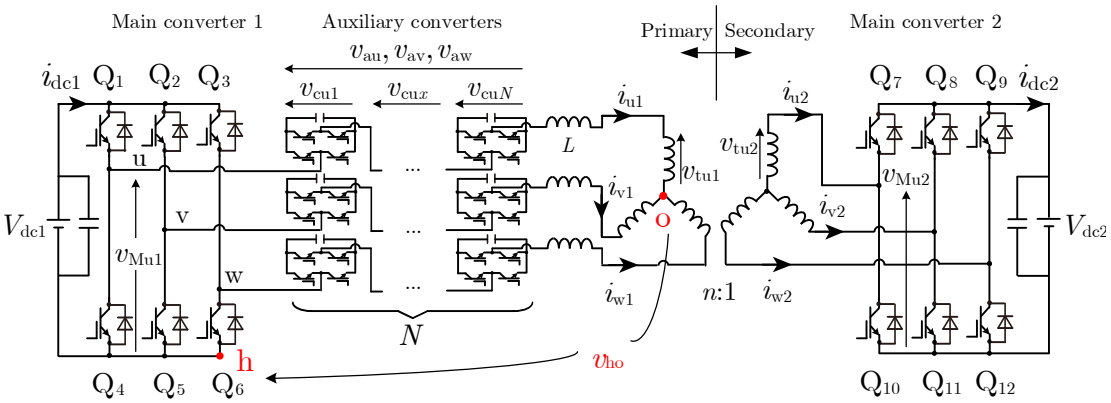

Figure 5-14 Circuit configuration of the NNPW-CF DC-DC converter with a Yn-Y transformer (using IGBTs).

The circuit configuration of NNPW-CF DC-DC converter is shown in Figure 5-14. Apart from the neutral wire, the NNPW-CF type and NPW-CF type have the same circuit topology. Besides, the NNPW-CF type has similar operating principles to the NNPW-CC type. Due to the absence of neutral point wire, the NNPW-CF type also needs to operate with variable-duty method. Compared with the NNPW-CC type, the NNPW-CF type does not need to raise v_{au} to avoid overmodulation, owing to the modulation ability with negative voltages of full bridges. In addition, the NNPW-CF type can reduce the value of V_c through a floating voltage. The specific method is shown in Figure 5-15(a). In Figure 5-15(a), the peak-to-peak value of v_{au} ($V_{p\text{-}p}$) is calculated as

$$V_{p-p} = \max\left\{v_{au}\right\} - \min\left\{v_{au}\right\}, \tag{5.19}$$

then an appropriate floating voltage (v_{ho}) is used to make the absolute values of the positive and negative peaks of v_{au} equal to half of the peak-to-peak value. i.e., the following equation holds:

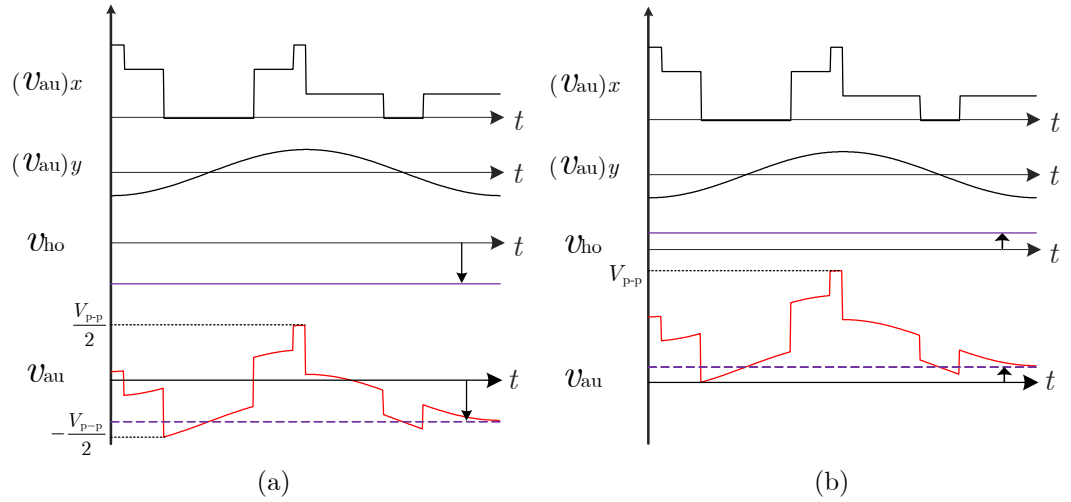

Figure 5-15 Simplified waveforms of (a) NNPW-CF; (b) NNPW-CC.

$$\max\left\{v_{\text{au}}\right\} = \max\left\{\left(v_{\text{au}}\right)_x + \left(v_{\text{au}}\right)_y\right\} + v_{\text{ho}} = \frac{1}{2}V_{\text{p-p}}\,. \tag{5.20}$$

Thus, the equation of v_{ho} can be given by

$$v_{\text{ho}} = \frac{1}{2}\max\left\{\left(v_{\text{au}}\right)_x + \left(v_{\text{au}}\right)_y\right\} + \frac{1}{2}\min\left\{\left(v_{\text{au}}\right)_x + \left(v_{\text{au}}\right)_y\right\}. \tag{5.21}$$

Meanwhile, the waveforms of the NNPW-CC type are also shown in Figure 5-15(b). Unlike the NNPW-CF type, the NNPW-CC type uses a floating voltage to raise v_{au} so that it remains entirely above zero, thereby preventing overmodulation. On the other hand, the NNPW-CF type uses a floating voltage to "balance" v_{au}, i.e., making (5.20) holds, thereby reducing V_{c}. Under the same conditions (V_{dc1}, $n\gamma$) and with the same output (I_{ac}), the waveforms of $(v_{\text{au}})_x$ and $(v_{\text{au}})_y$ for the NNPW-CC and NNPW-CF types are identical, i.e., the peak-to-peak value of v_{au} is same. In Figure 5-15(a), the maximum value of v_{au} can also be expressed using the peak-to-peak value $V_{\text{p-p}}$ as

$$\max\left\{v_{\text{au}}\right\} = V_{\text{p-p}}\,. \tag{5.22}$$

However, due to the difference in floating voltage, the peak value of v_{au} in the NNPW-CF type is ideally only half that of the NNPW-CC type as given by (5.20).

5.6 Cost Evaluations

This Chapter has discussed the circuit topologies and operating principles of three converters other than the basic cascaded converter (NPW-CC type). All of them do not have overmodulation concerns and limitations on voltage

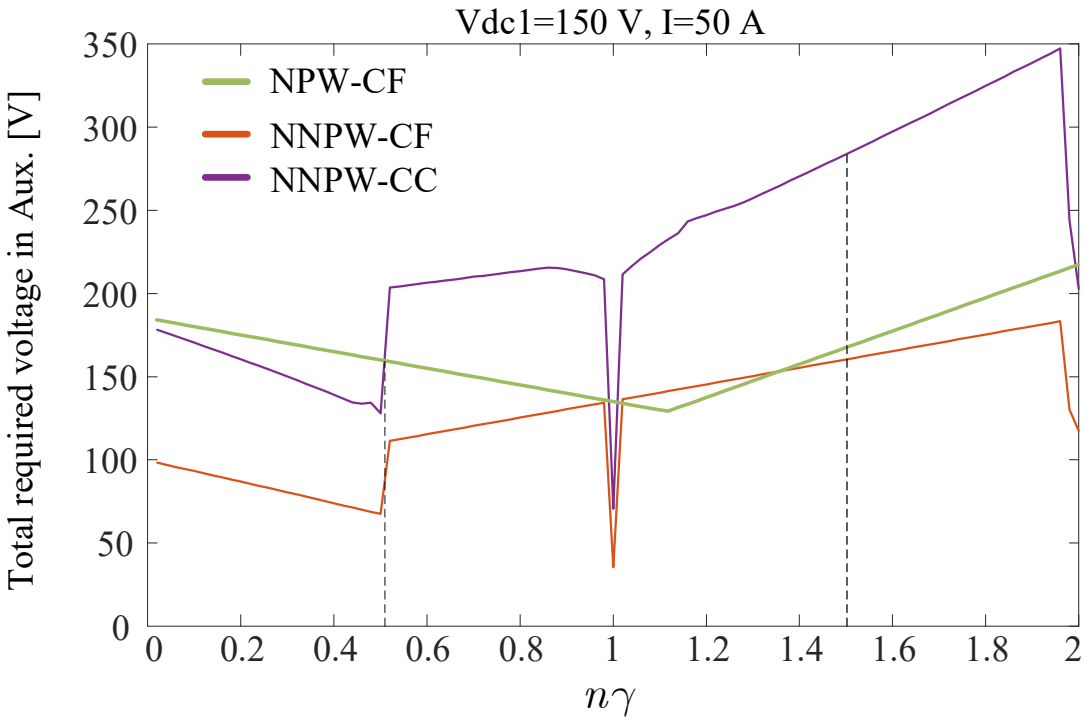

Figure 5-16 Minimum required voltages in each auxiliary converter under different $n\gamma$.

conversion ratio or output current. However, each converter has distinct characteristics and application scenarios. This Section focuses on cost, discussing the power rating and quantity of power components required for each auxiliary converter. All comparisons and discussions are based on the same V_{dc1}, $n\gamma$, and output power. The comparison focuses on the maximum value of v_{au}, which represents the maximum voltage the auxiliary converter needs to output. To achieve this maximum voltage, the total voltage of all DC capacitors in each phase of the auxiliary converter must exceed this value. Assuming that each phase of the converter has N cascaded converters and that the DC voltage of each cascaded converter is V_{c}, the following relationship must be satisfied:

$$V_{\mathrm{c}} \geq \frac{\max\left\{v_{\mathrm{au}}\right\}}{N}. \tag{5.23}$$

In this section, V_{dc1} is set to 150 V, I_{ac} is set to 50 A, and L is set to 0.5 mH. Figure 5-15 shows the theoretical maximum v_{au} values for the three converters when achieving the current amplitude of 50 A without overmodulation. As previously analyzed, it can be observed that the maximum v_{au} value of the NNPW-CF type is approximately half that of the NNPW-CC type. Additionally, the NPW-CF type has a higher v_{au} value than the NNPW-CF type in the range of $0 < n\gamma < 1$, while they are comparable in the range of $1 < n\gamma < 2$. Compared

TABLE IV
COST INDEX FOR AUXILIARY CONVERTER IN EACH PHASE

TYPE	Main Duty[1]	O.M.[2]	Devices Quantity[2]	Cell Quantity[3]	Device Rating[4]	Cost Index[5]
NPW-CC	Fixed/ Variable	Yes				
NNPW-CC	Variable	No	3	2X or X	Y or 2Y	6XY
NPW-CF	Fixed/ Variable	No	5	2X or X	Y or 2Y	10XY
NNPW-CF	Variable	No	5	X	Y	5XY

[1] What duty method can be used for main converters. [2] Does the converter has concern of overmodulation. [3] 2 power switches and 1 capacitor for choppers; 4 power switches and 1 capacitor for full bridges. [4] The number of cascaded converters, based on NNPW-CF type. [5] The power rating of each power device in auxiliary converters. [6] Evaluated cost, equal to device quantity times cell quantity times device power rating.

to the NNPW-CC type, the NPW-CF type has a significantly lower v_{au} value in the range of $0.5 < n\gamma < 2$ but a higher v_{au} value in the range of $0 < n\gamma < 0.5$. Based on the results in Figure 5-16, the cost of power components in the auxiliary converter for each type of converter can be evaluated, as shown in TABLE IV. It should be noted that the NPW-CC type is excluded from the cost evaluation due to concerns about overmodulation.

From TABLE IV, the NNPW-CF type has the lowest cost index. For example, when $n\gamma = 1.5$, the NNPW-CC type requires approximately 4 choppers rated at 80 V each (totaling 320 V), the NPW-CF type requires approximately 2 full bridges rated at 80 V each (totaling 160 V), and the NNPW-CF type also requires approximately 2 full bridges rated at 80 V each (totaling 160 V). Thus, the NNPW-CC type requires 12 power components rated at 80 V per phase (8 switches and 4 DC-capacitors), the NPW-CF type requires 10 power components rated at 80 V per phase (8 switches and 2 DC-capacitors), and the NNPW-CF type also requires 10 power components rated at 80 V (the same as the NPW-CF type). When $n\gamma = 0.5$, the NNPW-CC type requires approximately 2 choppers rated at 80 V each (totaling 160 V), the NPW-CF type requires approximately 2 full bridges rated at 80 V each (totaling 160 V), and the NNPW-CF type requires only 1 full bridge rated at 80 V (totaling 80 V). Thus, the NNPW-CC type requires 6 power components rated at 80 V per phase (4

switches and 2 DC-capacitors), the NPW-CF type requires 10 power components rated at 80 V per phase (8 switches and 2 DC-capacitors), and the NNPW-CF type requires only 5 power components rated at 80 V per phase (4 switches and 1 DC-capacitor).

Furthermore, TABLE IV also shows if the converter needs the variable-duty method. Although all CC DC-DC converters can use the variable-duty method to reduce zero-sequence current, it is not always necessary to do so. This is because the variable-duty method requires higher DC voltage (V_c) and switching frequency in the auxiliary converter (f_{s2}). However, since the NNPW-CC and NNPW-CF types lack a neutral point wire, the variable-duty method is necessary. Additionally, whether or not to use the variable-duty method also affects the type of transformer used. For example, when the variable-duty method is used, no zero-sequence current flows through the transformer (achieving unity power factor PF_{ot}), making three-limb core transformers unnecessary. On the other hand, for NPW-CC and NPW-CF converters that use fixed duty ratios, three-limb core transformers are recommended to prevent core saturation caused by zero-sequence currents.

It is worth noting that the cost index in this Section is for reference only. In practice, the cost index is not a fixed value; it varies with changes in current and $n\gamma$. Therefore, the cost of each converter should be evaluated based on specific applications and requirements.

5.7 Conclusion

This Chapter primarily discusses the remaining three types of cascaded converter DC-DC converters. The cascaded chopper DC-DC converters were categorized into four types in Subsection 2.5.2. Chapter 3 and Chapter 4 have introduced the basic type, the NPW-CC DC-DC converter, including its basic operating principles and experimental verification. However, the cascaded choppers in the NPW-CC type face a risk of overmodulation when operating at high voltage conversion ratios or currents. The other three types do not have overmodulation concerns and can utilize floating voltages or cascaded full-bridges (or both) to overcome the limitations of voltage conversion ratios and currents. This Chapter focuses on the operating principles of the NNPW-CC type and how it uses floating voltage to avoid overmodulation in choppers. Additionally,

this Chapter also briefly introduces the fundamentals of NPW-CF and NNPW-CF types. Although their operating principles are very similar to the previous two types, they each have unique characteristics, e.g., reducing V_c. Lastly, this Chapter introduces a cost index method based on the maximum voltage of the auxiliary converter to evaluate these three types of cascaded converter DC-DC converters.

Chapter 6 Discussions and Conclusions

6.1 Discussions

6.1.1 Optimal Switching Frequency

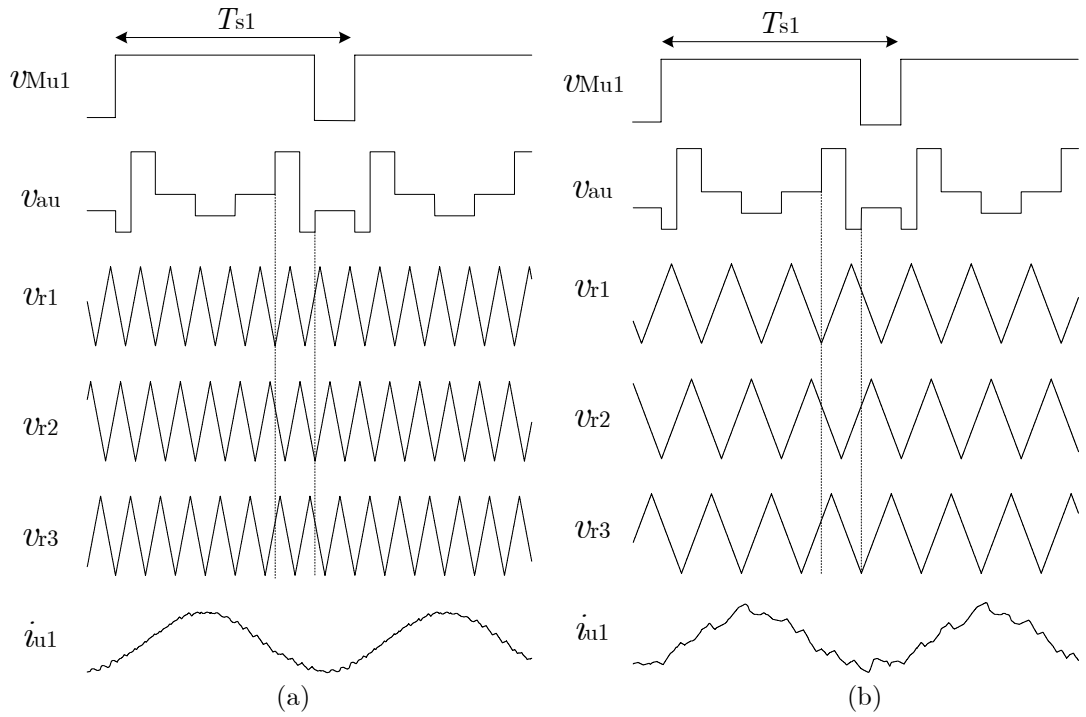

Figure 6-1 Waveforms using variable-duty method with same f_{s1} ($= 1/T_{s1}$) but different $f_{s2;}$ (a) $f_{s2} = 8f_{s1}$, (b) $f_{s2} = 4f_{s1}$.

This Section briefly discusses the switching frequency of the auxiliary converters. The proposed DC-DC converter in this dissertation is essentially a solution that trades additional power components for improved performance. The cascaded converter generates high-frequency components to control the low-frequency components of the main converter. It is well known that higher switching frequencies result in better control performance but also lead to larger switching

losses. Since the equivalent frequency of the cascaded converter is related to both the number of cascaded units and the switching frequency, achieving the same or even better performance with fewer converters and lower switching frequencies is one of the goals. However, this is not an easy task.

Figure 6-1(a) and (b) show the waveforms with different f_{s2}. When f_{s2} is sufficiently high, as shown in Figure 6-1(a), the carrier signal of the auxiliary converter can effectively generate $\left(v_{au}\right)_x$, resulting in better current control performance in the circuit. Conversely, when f_{s2} is too low, as shown in Figure 6-1(b), the large carrier intervals prevent certain cells of the auxiliary converter from correctly generating $(v_{au})_x$, leading to increased current harmonics and a loss of control. Additionally, the variable-duty method as discussed in Chapter 4 requires a much higher switching frequency compared to the fixed-duty method. This is because when the variation in duty cycle is small, a very high switching frequency is needed to reflect this information in the auxiliary converter, similar to the Nyquist sampling theorem. In the experimental verifications using variable-duty method, e.g., 450-Hz switching frequency was adopted as f_{s1} for the main converters and 3.6-kHz (which is 8 times of 450 Hz) switching frequency was adopted as f_{s2} for the auxiliary converters. The results are shown in Section 4.6 and they look well-controlled. However, if a lower f_{s2} is used, more distortion may be superimposed on the current and even makes the current out of sinusoidal. In fact, after several attempts, it was found that when f_{s2} is lower than 2.7 kHz, the experimental setup struggles to achieve good current control performance, and the results were subjectively considered by the author as "unusable".

Another point worth discussing is the current waveform. Obviously, this dissertation adopts a sinusoidal current which is in phase with the voltage to achieve zero reactive power and minimum distortion power. However, generating sinusoidal currents demands a higher switching frequency, because they are "irregular". Theoretically, if f_{s2} is sufficiently high, the converter can generate current waveforms of any shape. It is also possible to reduce f_{s2} by generating "regular" current waveforms, such as triangular or square waves. However, triangular and square waves contain higher harmonic components, which increase distortion power and, consequently, raise RMS current (and possibly peak current). The author of this dissertation believes that the choice of current waveform will depend on the specific application, which may become one of the research topics in the future.

Additionally, since the auxiliary converter employs PS-PWM, a higher equivalent frequency can also be achieved by increasing the number of cascaded units. However, this increases the number of power components. Similarly, replacing choppers with full bridges achieves 2-times equivalent frequency, by increasing 3 power components per cell to 5 power components per cell. Therefore, although this dissertation does not explore how to achieve the optimal number of cascaded units and switching frequency, investigating the optimal solution for the auxiliary converter could be a future direction of this research.

6.1.2 Cascaded-Converters DC-DC Converter with Breaker

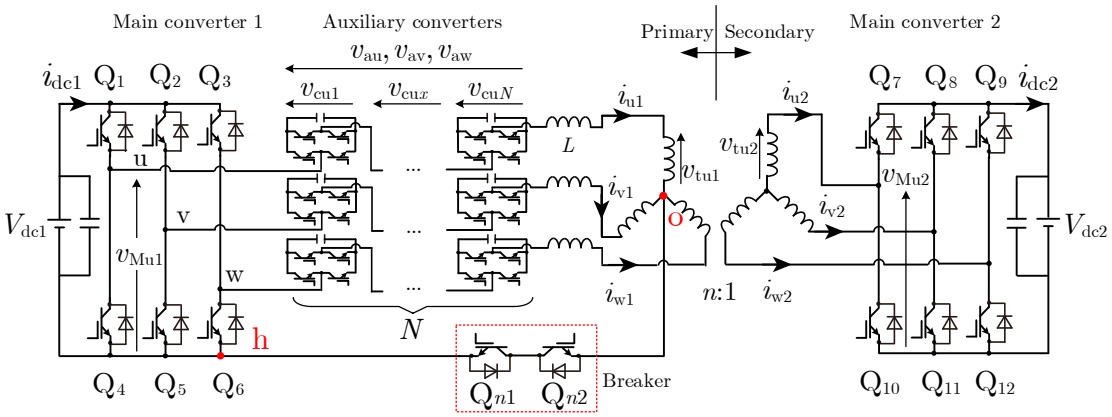

Figure 6-2 NPW-CF DC-DC converter with semiconductor breaker in neutral point wire (using IGBTs).

This dissertation discusses four types of cascaded-converter DC-DC converters. Although their structures are similar, each has distinct characteristics. Each converter excels in specific areas, so there is no definitive winner among them. However, in some cases, a solution that is suitable for most scenarios is desirable. This Section proposes a special structure aimed at achieving high performance over the entire load range and the full voltage conversion ratio range. Figure 6-2 shows the circuit topology of the NPW-CF DC-DC converter with a semiconductor breaker in the neutral point wire. This converter incorporates the functionalities of the NPW-CF, NNPW-CF, and TP-DAB converters. By controlling the cascaded full-bridge and circuit breakers, its operating mode can be switched. Specifically, this circuit features three operating modes:

1. When the cascaded full-bridge is bypassed (short-circuited) and the circuit breaker is open (Q_{n1} off, Q_{n2} off), the converter operates as a TP-DAB converter.

2. When the circuit breaker is short (Q_{n1} on, Q_{n2} on) and the auxiliary converter operates normally, the converter functions as an NNPW-CF converter. In this mode, the main converter should use the variable-duty method.
3. When the circuit breaker is open and the auxiliary converter operates normally, the converter functions as an NPW-CF converter. In this mode, the main converter can use either the fixed- or variable-duty ratio method.

Since ESS is a long-term operating system rather than an instantaneous one i.e., each operating state persists (e.g., the input and output voltages) for a relatively long time, the converter can switch operating modes as needed. The advantage of this design is that it ensures satisfactory performance across any voltage conversion ratio and load range. For example:

- When $n\gamma = 1$, the converter operates in TP-DAB mode, achieving high efficiency.
- When $n\gamma < 1$, the system operates in NPW-CF mode using the fixed-duty method.
- When $n\gamma \ll 1$, it operates in NPW-CF mode using the variable-duty method.
- When $n\gamma > 1$, it can operate in NNPW-CF mode.

This dissertation provides only one specific case as a reference, while real scenarios are far more complex. Determining how to switch modes requires calculations, evaluations, and validations. Since this topic is beyond the scope of this dissertation, further details are not provided here. The author hopes that this research can be continued in the future.

6.1.3 Transformer Design

This Section briefly discusses transformer design. Since each cascaded-converter DC-DC converter has its own unique characteristics, it is difficult to propose a universal transformer design method. However, the author still hopes that this dissertation can provide some considerations to inspire readers.

First, regarding the transformer windings turns ratio n, it is a crucial parameter (as it affects $n\gamma$). The core idea of this dissertation is to explore which converter has advantages under different $n\gamma$ conditions. For example, when $n\gamma = 1$, the TP-DAB converter clearly exhibits lower losses under typical load

conditions (as shown in Figure 5-9). Additionally, when $n\gamma > 1.5$, the NPW-CC type becomes unusable due to overmodulation. Therefore, when using the NPW-CC type, it is advisable to avoid employing a transformer with large n value. Nevertheless, from an engineering perspective, certain benchmarks must still be followed. For example, if the known DC input voltage range (e.g., the DC grid) is:

$$V_{\mathrm{i1}} \sim V_{\mathrm{i2}}\,. \tag{6.1}$$

and the DC output voltage range (e.g., the energy storage battery pack) is:

$$V_{\mathrm{o1}} \sim V_{\mathrm{o2}}\,. \tag{6.2}$$

then the range of γ should be considered as:

$$\gamma \in \left(\gamma_1, \gamma_2\right), \tag{6.3}$$

where

$$\gamma_1 = \frac{V_{\mathrm{o1}}}{V_{\mathrm{i2}}}, \gamma_2 = \frac{V_{\mathrm{o2}}}{V_{\mathrm{i1}}}\,. \tag{6.4}$$

In this case, n should be designed based on the γ in (6.3). For instance, the turns ratio n for the NPW-CC type should follow:

$$n < \frac{1.5}{\gamma_2} = \frac{1.5V_{\mathrm{i1}}}{V_{\mathrm{o2}}}\,. \tag{6.5}$$

The actual value of n should depend on the type of converter, its rated capacity, and the voltage conversion ratio. Additionally, for the mode-switchable converter discussed in the previous subsection, the design of n becomes more complex. This dissertation provides a design approach where $n\gamma$ is set near one (or equal to one), ensuring that the converter can switch between the three modes and achieve optimal performance under each voltage conversion ratio. In this case, the value of γ should be determined as the ratio of the average (or median) DC output voltage to the average (or median) DC input voltage.

6.2 Conclusions

This dissertation proposes a novel bidirectional isolated DC-DC converter based on the TP-DAB and cascaded converters. It comprises a total of four types.

In Chapter 3, one of these types, the NPW-CC DC-DC converter, is introduced. Compared to the conventional TP-DAB converter, it features lower RMS and peak currents. In some cases, it also achieves higher conversion efficiency, especially under light-load conditions. However, since the NPW-CC DC-DC

converter discussed in Chapter 3 adopts a fixed duty ratio, it generates significant DC current when the voltage conversion ratio ($n\gamma$) is not equal to one.

In Chapter 4, a variable-duty method for reducing DC current is proposed. This method effectively eliminates DC current, further reducing the RMS and peak currents in the circuit. Despite the advantages of the NPW-CC DC-DC converter, it still faces overmodulation issues under high voltage conversion ratios and high currents.

In Chapter 5, the overmodulation problem is discussed in detail. Additionally, the operating principles of the remaining three types of cascaded converter DC-DC converters are introduced. Finally, this dissertation compares the minimum voltage requirements of the auxiliary converters for each type and proposes a cost index method for evaluating them.

APPENDIX I

Appendix I is attached for the calculations of RMS and peak currents of the TP-DAB converter (topology in Figure 2-3). It should be noted that all analysis and calculations for TP-DAB converter are based on SPS modulation introduced in [86], and this part is only used as supplementary materials for Section 3.6. Since the TP-DAB converter involves phase shift angle, all derivations in this appendix are conducted using radians rather than time. The TP-DAB converter has two operating modes switched at $\phi = 60°$. When $0° \leq \phi \leq 60°$, the key waveforms of the TP-DAB converter can be shown as Figure 2-4(a). The current waveform can be expressed as

$$i_{\mathrm{n1}} = \begin{cases} i_1(\delta) = i(0) + \dfrac{V_{\mathrm{dc1}}(1+n\gamma)}{3\omega_{\mathrm{s1}}L}\delta & 0 \leq \delta < \phi \\ i_2(\delta) = i(\phi) + \dfrac{V_{\mathrm{dc1}}(1-n\gamma)}{3\omega_{\mathrm{s1}}L}(\delta-\phi) & \phi \leq \delta < \dfrac{\pi}{3} \\ i_3(\delta) = i(\dfrac{\pi}{3}) + \dfrac{V_{\mathrm{dc1}}(2-n\gamma)}{3\omega_{\mathrm{s1}}L}(\delta-\dfrac{\pi}{3}) & \dfrac{\pi}{3} \leq \delta < \dfrac{\pi}{3}+\phi \\ i_4(\delta) = i(\phi+\dfrac{\pi}{3}) + \dfrac{V_{\mathrm{dc1}}(2-n\gamma)}{3\omega_{\mathrm{s1}}L}(\delta-\phi-\dfrac{\pi}{3}) & \dfrac{\pi}{3}+\phi \leq \delta < \dfrac{2\pi}{3} \\ i_5(\delta) = i(\dfrac{2\pi}{3}) + \dfrac{V_{\mathrm{dc1}}(2-2n\gamma)}{3\omega_{\mathrm{s1}}L}(\delta-\dfrac{2\pi}{3}) & \dfrac{2\pi}{3} \leq \delta < \dfrac{2\pi}{3}+\phi \\ i_6(\delta) = i(\phi+\dfrac{2\pi}{3}) + \dfrac{V_{\mathrm{dc1}}(2-n\gamma)}{3\omega_{\mathrm{s1}}L}(\delta-\phi-\dfrac{2\pi}{3}) & \dfrac{2\pi}{3}+\phi \leq \delta \leq \pi \end{cases} \quad ,(A.1)$$

where $i(0)$ denotes the initial current value and $i(0) = \dfrac{V_{\mathrm{dc1}}}{3\omega_{\mathrm{s1}}L}\left(\dfrac{2\pi\gamma}{3} - \gamma\phi - \dfrac{2\pi}{3}\right)$. Meanwhile, the transmitted power of the TP-DAB converter in this case is given by

$$P_{\mathrm{o}}\left(\phi,\ n\gamma\right) = \frac{V_{\mathrm{dc1}}^2 n\gamma}{\omega_{\mathrm{s1}}L}\phi\left[\frac{2}{3} - \frac{\phi}{2\pi}\right]. \quad (A.2)$$

It can be seen that the relationship between the phase shift angle ϕ and the transmitted power P_{o} is a quadratic equation. Therefore, mathematically, the required ϕ corresponding to the desired transmitted power can be solved using the quadratic formula. Subsequently, substituting this ϕ into (A.1) yields the

current expression for the first half-cycle (0, π). Finally, the current expression for the second half-cycle can also be obtained due to symmetry.

Figure 2-4(b) shows the key waveforms of the TP-DAB converter when 60°≤ ϕ ≤120°. In this case, the current waveform can be expressed as

$$i_{u1}=\begin{cases} i_1(\delta)=i(0)+\dfrac{V_{dc1}(1+2n\gamma)}{3\omega_{s1}L}\delta & 0\le\delta<\phi-\dfrac{\pi}{3} \\ i_2(\delta)=i(\phi-\dfrac{\pi}{3})+\dfrac{V_{dc1}(1+n\gamma)}{3\omega_{s1}L}(\delta-\phi+\dfrac{\pi}{3}) & \phi-\dfrac{\pi}{3}\le\delta<\dfrac{\pi}{3} \\ i_3(\delta)=i(\dfrac{\pi}{3})+\dfrac{V_{dc1}(2+n\gamma)}{3\omega_{s1}L}(\delta-\dfrac{\pi}{3}) & \dfrac{\pi}{3}\le\delta<\phi \\ i_4(\delta)=i(\phi)+\dfrac{V_{dc1}(2-n\gamma)}{3\omega_{s1}L}(\delta-\phi) & \phi\le\delta<\dfrac{2\pi}{3} \\ i_5(\delta)=i(\dfrac{2\pi}{3})+\dfrac{V_{dc1}(1-n\gamma)}{3\omega_{s1}L}(\delta-\dfrac{2\pi}{3}) & \dfrac{2\pi}{3}\le\delta<\phi+\dfrac{\pi}{3} \\ i_6(\delta)=i(\phi+\dfrac{\pi}{3})+\dfrac{V_{dc1}(1-2n\gamma)}{3\omega_{s1}L}(\delta-\phi-\dfrac{\pi}{3}) & \phi+\dfrac{\pi}{3}\le\delta<\pi \end{cases}, \quad \text{(A.3)}$$

where $i(0)=\frac{V_{dc1}}{3\omega_{s1}L}\left(\pi\gamma-2\gamma\phi-\frac{2\pi}{3}\right)$. Meanwhile, the transmitted power of the TP-DAB converter in this case is given by

$$P_o\left(\phi,\ n\gamma\right)=\frac{V_{dc1}^2 n\gamma}{\omega_{s1}L}\left[\phi-\frac{\phi^2}{\pi}-\frac{\pi}{18}\right]. \quad \text{(A.4)}$$

In this case, the relationship between the phase shift angle ϕ and the transmitted power P_o remains a quadratic equation. Therefore, the previous method is still applicable.

APPENDIX II

The u-phase inductor current using fixed duty ratio is a superimposed waveform containing both DC and AC components. It is given by (3.13) and (3.16) as

$$i_{u1} = I_{ac}\left[\sin(\omega t) + \frac{2}{\pi}(n\gamma - 1)\right]. \tag{B.1}$$

The peak and RMS values of (B.1) can be calculated as

$$I_{peak\_old} = |I_{ac}| + |I_{dc}| = |I_{ac}|(1 + \frac{2}{\pi} - \frac{2}{\pi}n\gamma)$$

$$I_{rms\_old} = \sqrt{\frac{1}{2}I_{ac}^2 + I_{dc}^2} = |I_{ac}|\sqrt{\frac{1}{2} + \frac{2}{\pi^2}(n^2\gamma^2 - 2n\gamma + 1)}\,. \tag{B.2}$$

Meanwhile, since the variable-duty method eliminates the DC component from the inductor current, i_{u1} becomes to a pure sinusoidal waveform as

$$i_{u1} = I_{ac}\sin(\omega t). \tag{B.3}$$

The peak and RMS values of (B.3) can be calculated as

$$I_{peak\_new} = |I_{ac}|$$

$$I_{rms\_new} = \frac{1}{\sqrt{2}}|I_{ac}|. \tag{B.4}$$

REFERENCES

[1] Maximum efficiencies of engines and turbines, 1700-2000 - Visualizing Energy; https://visualizingenergy.org/maximum-efficiencies-of-engines-and-turbines-1700-2000/

[2] Joseph Swan - Wikipedia

[3] https://www.nea.gov.cn/2024-06/28/c_1212375938.htm; (In Chinese, by National Energy Administration, Chinese Government)

[4] https://mp.weixin.qq.com/s/Xx68yS1eulqD7qxzE36ctQ; (In Chinese, by National Energy Administration, Chinese Government)

[5] Report-Global-Electricity-Review-2024.pdf (Global Electricity Review 2024 | Ember (ember-climate.org)); https://ember-climate.org/insights/research/global-electricity-review-2024/supporting-material/;

[6] Zhang, Q., Hu, Y., Jiao, J. et al. The impact of Russia-Ukraine war on crude oil prices: an EMC framework. Humanit Soc Sci Commun 11, 8 (2024).

[7] Jennings, M. Oil and war: we had the warning 30 years ago. Nature 423, 15 (2003).

[8] Ruhnau, O., Stiewe, C., Muessel, J. et al. Natural gas savings in Germany during the 2022 energy crisis. Nat Energy 8, 621-628 (2023).

[9] IEA (2023), *World Energy Outlook 2023*, IEA, Paris https://www.iea.org/reports/world-energy-outlook-2023, Licence: CC BY 4.0 (report); CC BY NC SA 4.0 (Annex A).

[10] History of Hydropower | Department of Energy; https://www.energy.gov/eere/water/history-hydropower-0.

[11] The History of Nuclear Energy_0.pdf; https://www.energy.gov/sites/prod/files/The%20History%20of%20Nuclear%20Energy_0.pdf

[12] How deadly lessons from Fukushima changed Japan and the world — Harvard Gazette. https://news.harvard.edu/gazette/story/2023/04/how-deadly-lessons-from-fukushima-changed-japan-and-the-world/.

[13] Japan plans to release Fukushima's wastewater into the ocean | Science | AAAS, https://www.science.org/content/article/japan-plans-release-fukushima-s-contaminated-water-ocean/

[14] Chernobyl: How bad was it? | MIT News | Massachusetts Institute of Technology; https://news.mit.edu/2019/chernobyl-manual-for-survival-book-0306.

[15] Zhang, X.; Dong, Z.; Gupta, H.; Wu, G.; Li, D. Impact of the Three Gorges Dam on the Hydrology and Ecology of the Yangtze River. Water 2016, 8, 590.

[16] Effects | Facts - Climate Change: Vital Signs of the Planet (nasa.gov), https://climate.nasa.gov/effects

[17] Gasser, T., Guivarch, C., Tachiiri, K. et al. Negative emissions physically needed to keep global warming below 2 °C. Nat Commun 6, 7958 (2015).

[18] Liu, Z., Guan, D., Wei, W. et al. Reduced carbon emission estimates from fossil fuel combustion and cement production in China. Nature 524, 335-338 (2015).

[19] Li, H., Zick, M.E., Trisukhon, T. et al. Capturing carbon dioxide from air with charged-sorbents. Nature 630, 654-659 (2024).

[20] Marques Lameirinhas, R.A.; Torres, J.P.N.; de Melo Cunha, J.P. A Photovoltaic Technology Review: History, Fundamentals and Applications. Energies 2022, 15, 1823.

[21] John K. Kaldellis, D. Zafirakis, The wind energy (r)evolution: A short review of a long history, Renewable Energy, Volume 36, Issue 7, 2011, pp 1887-1901.

[22] Power Plant Efficiency: Coal, Natural Gas, Nuclear, and More | PCI (pcienergysolutions.com); https://www.pcienergysolutions.com/2023/04/17/power-plant-efficiency-coal-natural-gas-nuclear-and-more/

[23] Energy Efficiency: Buildings and Industry | Department of Energy; https://www.energy.gov/eere/energy-efficiency-buildings-and-industry

[24] IEA (2024), Renewables 2023, IEA, Paris https://www.iea.org/reports/renewables-2023, Licence: CC BY 4.0

[25] Annual Energy Outlook 2023 - U.S. Energy Information Administration (EIA); https://www.eia.gov/outlooks/aeo/

[26] https://www.nea.gov.cn/2024-05/31/c_1310776691.htm. (In Chinese, by National Energy Administration, Chinese Government)

[27] https://www.nea.gov.cn/2024-06/07/c_1310777542.htm (In Chinese, by National Energy Administration, Chinese Government)

[28] http://www.sgcc.com.cn:8000/#here. (In Chinese, by State Grid Corporation of China)

[29] Wang, Y., Wang, R., Tanaka, K. et al. Accelerating the energy transition towards photovoltaic and wind in China. Nature 619, 761-767 (2023).

[30] N. Sockeel, J. Gafford, B. Papari and M. Mazzola, "Virtual Inertia Emulator-Based Model Predictive Control for Grid Frequency Regulation Considering High Penetration of Inverter-Based Energy Storage System," in *IEEE Transactions on Sustainable Energy*, vol. 11, no. 4, pp. 2932-2939, Oct. 2020.

[31] J. Pahasa, P. Potejana and I. Ngamroo, "MPC-Based Virtual Energy Storage System Using PV and Air Conditioner to Emulate Virtual Inertia and Frequency Regulation of the Low-Inertia Microgrid," in *IEEE Access*, vol. 10, pp. 133708-133719, 2022.

[32] T. Rahimi, L. Ding, M. Kheshti, R. Faraji, J. M. Guerrero and G. D. A. Tinajero, "Inertia Response Coordination Strategy of Wind Generators and Hybrid Energy Storage and Operation Cost-Based Multi-Objective Optimizing of Frequency Control Parameters," in *IEEE Access*, vol. 9, pp. 74684-74702, 2021.

[33] M. Enomoto, K. Sano, J. Kanno and J. Fukushima, "Continuous Operation of Wind Power Plants Under Pole-to-Ground Fault in an HVDC System Consisting of Half-Bridge MMCs and Disconnecting Switches," in *IEEE Transactions on Power Electronics*, vol. 38, no. 3, pp. 3812-3823, March 2023.

[34] M. Enomoto, K. Sano, J. Kanno and J. Fukushima, "Reconfiguration of Bipolar HVDC System for Continuous Transmission Under DC Line Fault," in *IEEE Transactions on Power Electronics*, vol. 39, no. 7, pp. 8622-8633, July 2024.

[35] K. Mahmud, M. J. Hossain and J. Ravishankar, "Peak-Load Management in Commercial Systems With Electric Vehicles," in *IEEE Systems Journal*, vol. 13, no. 2, pp. 1872-1882, June 2019.

[36] 九州「太陽光で発電しすぎ問題」とは何なのか せっかくの再エネ発電を

無駄にしない秘策 | 資源・エネルギー | 東洋経済オンライン (toyokeizai.net); https://toyokeizai.net/articles/-/244405 (In Japanese)

[37] 関西エリア、初の出力制御　太陽光や風力発電一時停止 - 産経ニュース (sankei.com); https://www.sankei.com/article/20230604-AJ57N3B7ZRO75O4SDTDABCVJ2Q/ (In Japanese)

[38] 東京電力管内 8月31日まで節電要請 家庭で無理なくできる節電方法とは？ | NHK; https://www.nhk.or.jp/shutoken/newsup/20230703a.html (In Japanese)

[39] 最大電力実績カレンダー（2023年）｜でんき予報の解説｜東京電力ホールディングス株式会社 (tepco.co.jp); https://www.tepco.co.jp/forecast/html/calendar2023-j.html (In Japanese)

[40] Yi-chun CHEN, Taiwan's Nuclear Power Phase-out Decision-Making Process During the Energy Transition Pathway, Papers on Environmental Information Science, 2018, Volume ceis32, Vol.32 (The 32th Conference on Environmental Information Science), Pages 55-60, Released on J-STAGE December 07, 2018.

[41] 為邁向2025非核家園目標 推動新能源政策 (行政院全球資訊網-本院一般新聞) (ey.gov.tw); https://www.ey.gov.tw/Page/9277F759E41CCD91/c094fb4e-6c07-4a87-9435-fb97f11dde10 (In Chinese, by Taiwan Government)

[42] Rolling Blackouts Hit Taiwan After Accident at Power Plant - The New York Times (nytimes.com); https://www.nytimes.com/2021/05/13/world/asia/taiwan-blackout-power-outage.html

[43] Power goes out across Taiwan due to power plant failure | Taiwan News | May. 13, 2021 15:31; https://www.taiwannews.com.tw/news/4202759

[44] Blackouts reported across Taiwan | Taiwan News | Mar. 3, 2022 09:43; https://www.taiwannews.com.tw/news/4460516

[45] X. Huang et al., "Wind-Storage Collaborative Control Strategy for Considering the State of Charge of Energy Storage Batteries," 2023 5th International Conference on Smart Power & Internet Energy Systems (SPIES), Shenyang, China, 2023, pp. 250-255.

[46] W. Guodong, H. Diangang, L. Xiaohu and L. Lijuan, "Analysis of Energy Storage Mode and Configuration Strategy of Gansu Considering Grid Peak

Shaving," *2022 IEEE 6th Conference on Energy Internet and Energy System Integration (EI2)*, Chengdu, China, 2022, pp. 183-188.

[47] Negative prices in wholesale electricity markets indicate supply inflexibilities - U.S. Energy Information Administration (EIA); https://www.eia.gov/todayinenergy/detail.php?id=5110

[48] J. Feng, J. Hu, Y. Wang, S. Fang, K. Yan and Y. Zhou, "Distributed Robust Optimal Scheduling for Integrated Energy System Considering Source-Load Uncertainty," 2021 IEEE 5th Conference on Energy Internet and Energy System Integration (EI2), Taiyuan, China, 2021, pp. 1462-1467.

[49] W. Huang, X. Zhang, K. Li, N. Zhang, G. Strbac and C. Kang, "Resilience Oriented Planning of Urban Multi-Energy Systems With Generalized Energy Storage Sources," in *IEEE Transactions on Power Systems*, vol. 37, no. 4, pp. 2906-2918, July 2022

[50] M. -S. Lu, C. -L. Chang, W. -J. Lee and L. Wang, "Combining the Wind Power Generation System With Energy Storage Equipment," in *IEEE Transactions on Industry Applications*, vol. 45, no. 6, pp. 2109-2115, Nov.-dec. 2009.

[51] M. Kermani, E. Shirdare, G. Parise, M. Bongiorno and L. Martirano, "A Comprehensive Technoeconomic Solution for Demand Control in Ports: Energy Storage Systems Integration," in *IEEE Transactions on Industry Applications*, vol. 58, no. 2, pp. 1592-1601, March-April 2022.

[52] T. Luo, Y. -C. Su and M. Hagiwara, "An Isolated DC-DC Converter with Multiple Cascaded Choppers Featuring RMS Current Reduction toward Resilient Power Grids," in *IEEE Transactions on Industry Applications*.

[53] K. Bi, L. Sun, Q. An and J. Duan, "Active SOC Balancing Control Strategy for Modular Multilevel Super Capacitor Energy Storage System," in *IEEE Transactions on Power Electronics*, vol. 34, no. 5, pp. 4981-4992, May 2019.

[54] Z. Zhu, F. Xiao, Z. Huang, J. Liu, P. Chen and Q. Ren, "Bidirectional Power Control Strategy for Super Capacitor Energy Storage System Based on MMC DC-DC Converter," in *IEEE Access*, vol. 10, pp. 53225-53233, 2022.

[55] M. Shehzad, N. Jamal, H. A. Muqeet, S. Mirsaeidi and K. M. Muttaqi,

"Cost Effective Analysis of Stationary and Mobile Energy Storage Systems in Prosumer Microgrid Considering System Reliability and Real-Time Pricing Scheme," 2023 IEEE International Conference on Energy Technologies for Future Grids (ETFG), Wollongong, Australia, 2023, pp. 1-5.

[56] Y. Liu, C. Ke, L. Yang, H. Liu, Y. Chen, and J. Yuan, "The development of battery storage co-located with renewable energy in China: A policy-driven system dynamics approach," J. Renewable Sustainable Energy 15, 015903 (2023), 31 January 2023.

[57] https://www.nea.gov.cn/2024-08/02/c_1310783696.htm (In Chinese, by National Energy Administration, Chinese Government)

[58] W. Huang, X. Zhang, K. Li, N. Zhang, G. Strbac and C. Kang, "Resilience Oriented Planning of Urban Multi-Energy Systems With Generalized Energy Storage Sources," in *IEEE Transactions on Power Systems*, vol. 37, no. 4, pp. 2906-2918, July 2022.

[59] M. Liu, W. Li, C. Wang, M. P. Polis, L. Y. Wang and J. Li, "Reliability Evaluation of Large Scale Battery Energy Storage Systems," in *IEEE Transactions on Smart Grid*, vol. 8, no. 6, pp. 2733-2743, Nov. 2017.

[60] M. Basić and D. Dujić, "Hybrid modular multilevel converter for variable DC link voltage operation," in *CPSS Transactions on Power Electronics and Applications*, vol. 6, no. 2, pp. 178-190, June 2021.

[61] L. Maharjan, S. Inoue and H. Akagi, "A Transformerless Energy Storage System Based on a Cascade Multilevel PWM Converter With Star Configuration," in *IEEE Transactions on Industry Applications*, vol. 44, no. 5, pp. 1621-1630, Sept.-Oct. 2008.

[62] J. E. Huber and J. W. Kolar, "Applicability of Solid-State Transformers in Today's and Future Distribution Grids," in *IEEE Transactions on Smart Grid*, vol. 10, no. 1, pp. 317-326, Jan. 2019.

[63] Y. Lu, K. Sun, H. Wu, X. Dong and Y. Xing, "A Three-Port Converter Based Distributed DC Grid Connected PV System With Autonomous Output Voltage Sharing Control," in *IEEE Transactions on Power Electronics*, vol. 34, no. 1, pp. 325-339, Jan. 2019.

[64] Y. Xuan, X. Yang, W. Chen, T. Liu and X. Hao, "A Novel Three-Level CLLC Resonant DC-DC Converter for Bidirectional EV Charger in DC Microgrids," in *IEEE Transactions on Industrial Electronics*, vol. 68, no.

3, pp. 2334-2344, March 2021.

[65] F. Li et al., "Smart Transmission Grid: Vision and Framework," in *IEEE Transactions on Smart Grid*, vol. 1, no. 2, pp. 168-177, Sept. 2010.

[66] D. D. -C. Lu and V. G. Agelidis, "Photovoltaic-Battery-Powered DC Bus System for Common Portable Electronic Devices," in *IEEE Transactions on Power Electronics*, vol. 24, no. 3, pp. 849-855, March 2009.

[67] N. Hou, L. Ding, P. Gunawardena, T. Wang, Y. Zhang and Y. W. Li, "A Partial Power Processing Structure Embedding Renewable Energy Source and Energy Storage Element for Islanded DC Microgrid," in *IEEE Transactions on Power Electronics*, vol. 38, no. 3, pp. 4027-4039, March 2023.

[68] K. Sun, L. Zhang, Y. Xing and J. M. Guerrero, "A Distributed Control Strategy Based on DC Bus Signaling for Modular Photovoltaic Generation Systems With Battery Energy Storage," in *IEEE Transactions on Power Electronics*, vol. 26, no. 10, pp. 3032-3045, Oct. 2011.

[69] Y. -C. Su, H. -M. Li, P. -L. Chen and P. -T. Cheng, "Integration of PV Panels and EV Chargers on the Modular Multilevel Converter Based SST," in *IEEE Transactions on Industry Applications*, vol. 58, no. 5, pp. 6428-6437, Sept.-Oct. 2022.

[70] R. Kheirollahi *et al.*, "Techno-Economic Analysis of Solid-State Circuit Breakers in DC Power System Applications: Design, Cost, and Performance Analyses," in *IEEE Industry Applications Magazine*, vol. 30, no. 3, pp. 32-45, May-June 2024.

[71] D. Liu and H. Li, "A ZVS Bi-Directional DC-DC Converter for Multiple Energy Storage Elements," in *IEEE Transactions on Power Electronics*, vol. 21, no. 5, pp. 1513-1517, Sept. 2006.

[72] K. -M. Yoo and J. -Y. Lee, "A 10-kW Two-Stage Isolated/Bidirectional DC/DC Converter With Hybrid-Switching Technique," in *IEEE Transactions on Industrial Electronics*, vol. 60, no. 6, pp. 2205-2213, June 2013.

[73] J. Zeng, X. Du and Z. Yang, "A Multiport Bidirectional DC-DC Converter for Hybrid Renewable Energy System Integration," in *IEEE Transactions on Power Electronics*, vol. 36, no. 11, pp. 12281-12291, Nov. 2021.

[74] J. Rocabert, R. Capó-Misut, R. S. Muñoz-Aguilar, J. I. Candela and P. Rodriguez, "Control of Energy Storage System Integrating Electrochemical Batteries and Supercapacitors for Grid-Connected Applications," in *IEEE*

Transactions on Industry Applications, vol. 55, no. 2, pp. 1853-1862, March-April 2019.

[75] R. K. Kanaparthi, J. P. Singh and M. S. Ballal, "A Review on Multi-Port Bidirectional Isolated and Non-Isolated DC-DC Converters for Renewable Applications," *2022 IEEE International Conference on Power Electronics, Drives and Energy Systems (PEDES)*, Jaipur, India, 2022.

[76] Y. Li, Y. Wang, Y. Guan and D. Xu, "Design and Analysis of Integrated Bidirectional DC-DC Converter for Energy Storage Systems," in *IEEE Transactions on Industrial Electronics*, vol. 71, no. 9, pp. 10568-10579, Sept. 2024.

[77] N. Kondrath, "Bidirectional DC-DC converter topologies and control strategies for interfacing energy storage systems in microgrids: An overview," *2017 IEEE International Conference on Smart Energy Grid Engineering (SEGE)*, Oshawa, ON, Canada, 2017, pp. 341-345.

[78] S. A. Gorji, H. G. Sahebi, M. Ektesabi and A. B. Rad, "Topologies and Control Schemes of Bidirectional DC-DC Power Converters: An Overview," in *IEEE Access*, vol. 7, pp. 117997-118019, 2019.

[79] Q. Xu, N. Vafamand, L. Chen, T. Dragičević, L. Xie and F. Blaabjerg, "Review on Advanced Control Technologies for Bidirectional DC/DC Converters in DC Microgrids," in *IEEE Journal of Emerging and Selected Topics in Power Electronics*, vol. 9, no. 2, pp. 1205-1221, April 2021.

[80] H. Bai and C. Mi, "Eliminate Reactive Power and Increase System Efficiency of Isolated Bidirectional Dual-Active-Bridge DC-DC Converters Using Novel Dual-Phase-Shift Control," in *IEEE Transactions on Power Electronics*, vol. 23, no. 6, pp. 2905-2914, Nov. 2008.

[81] P. Yang, M. Wang, S. Liu, S. Li, X. Chen and Y. Peng, "Unilateral Asymmetric Triple Phase Shift Modulation Strategy for DAB Converter Compromising RMS Current and Soft-Switching Range," in *IEEE Transactions on Circuits and Systems II: Express Briefs*, vol. 71, no. 6, pp. 3216-3220, June 2024.

[82] H. Shi *et al.*, "Minimum-Backflow-Power Scheme of DAB-Based Solid-State Transformer With Extended-Phase-Shift Control," in *IEEE Transactions on Industry Applications*, vol. 54, no. 4, pp. 3483-3496, July-Aug. 2018.

[83] J. Yin, X. He, J. Lu and H. S. -H. Chung, "Phase-Shift Control With Unified PWM/PFM for Improved Transient Response in a Bidirectional Dual-Active-Bridge DC/DC Converter," in *IEEE Transactions on Industrial Electronics*, vol. 70, no. 9, pp. 8862-8872, Sept. 2023.

[84] J. Lu and J. Yin, "Unified Phase Shift Control Strategy to Optimize Transient Current Response in a Dual Active Bridge DC-DC Converter during Unidirectional and Bidirectional Power Flow Changes," *2020 IEEE 9th International Power Electronics and Motion Control Conference (IPEMC2020-ECCE Asia)*, Nanjing, China, 2020, pp. 2599-2604.

[85] Q. Bu, H. Wen, H. Shi and Y. Zhu, "A Comparative Review of High-Frequency Transient DC Bias Current Mitigation Strategies in Dual-Active-Bridge DC-DC Converters Under Phase-Shift Modulations," in *IEEE Transactions on Industry Applications*, vol. 58, no. 2, pp. 2166-2182, March-April 2022.

[86] R. W. A. A. De Doncker, D. M. Divan and M. H. Kheraluwala, "A three-phase soft-switched high-power-density DC/DC converter for high-power applications," in *IEEE Transactions on Industry Applications*, vol. 27, no. 1, pp. 63-73, Jan.-Feb. 1991.

[87] Divan, Deepakraj M., “High power density dc/dc converter: Component selection and design,”, *NASA Technical Reports*, January 1, 1989.

[88] M. N. Kheraluwala, R. W. Gascoigne, D. M. Divan and E. D. Baumann, "Performance characterization of a high-power dual active bridge DC-to-DC converter," in *IEEE Transactions on Industry Applications*, vol. 28, no. 6, pp. 1294-1301, Nov.-Dec. 1992.

[89] Rik W. De Doncker, Mustansir H. Kheraluwala, Deepakraj M. Divan, “Power conversion apparatus for DC/DC conversion using dual active bridges,” US Patent, US5027264A.

[90] G. -J. Su and L. Tang, "A Three-Phase Bidirectional DC-DC Converter for Automotive Applications," *2008 IEEE Industry Applications Society Annual Meeting*, 2008, pp. 1-7.

[91] H. Chen, S. Ouyang, J. Liu and X. Li, "An Asymmetrical Phase-Shift Scheme of Three-Phase Dual Active Bridge With Minimum Current Root-Mean-Square Value Control," in *IEEE Transactions on Power Electronics*, vol. 37, no. 12, pp. 14343-14361, Dec. 2022.

[92] K. Vorobev, R. Strzelecki and N. Poliakov, "Balancing energy consumption in limited power grid with active front-end and three phase dual active bridge system," *2020 IEEE 14th International Conference on Compatibility, Power Electronics and Power Engineering (CPE-POWERENG)*, Setubal, Portugal, 2020, pp. 429-432.

[93] Z. Wang and H. Li, "A Soft Switching Three-phase Current-fed Bidirectional DC-DC Converter With High Efficiency Over a Wide Input Voltage Range," in *IEEE Transactions on Power Electronics*, vol. 27, no. 2, pp. 669-684, Feb. 2012.

[94] P. Liu, C. Chen, S. Duan and W. Zhu, "Dual Phase-Shifted Modulation Strategy for the Three-Level Dual Active Bridge DC-DC Converter," in *IEEE Transactions on Industrial Electronics*, vol. 64, no. 10, pp. 7819-7830, Oct. 2017.

[95] H. M. de Oliveira Filho, D. de Souza Oliveira and P. P. Praça, "Steady-State Analysis of a ZVS Bidirectional Isolated Three-Phase DC-DC Converter Using Dual Phase-Shift Control With Variable Duty Cycle," in *IEEE Transactions on Power Electronics*, vol. 31, no. 3, pp. 1863-1872, March 2016.

[96] Y. Cui, D. Wang and A. Emadi, "Three-phase dual active bridge converter design considerations," *IECON 2017 - 43rd Annual Conference of the IEEE Industrial Electronics Society*, Beijing, China, 2017, pp. 4696-4701.

[97] X. Qu, X. Bi and C. Wang, "Efficiency Optimization of Three-Phase DAB Converter Based on APWM Cascade SPS Control," *2024 7th International Conference on Advanced Algorithms and Control Engineering (ICAACE)*, Shanghai, China, 2024, pp. 1248-1252.

[98] S. K. Rastogi, S. S. Shah, B. N. Singh and S. Bhattacharya, "Mode Analysis and Identification Scheme of Open-Circuit Fault in a Three-phase DAB Converter," *2021 IEEE Energy Conversion Congress and Exposition (ECCE)*, Vancouver, BC, Canada, 2021, pp. 2762-2769.

[99] A. Aouiti, A. Soyed and F. Bacha, "Control and Study of the Bidirectional Three Phase DAB Converter," *2022 8th International Conference on Control, Decision and Information Technologies (CoDIT)*, Istanbul, Turkey, 2022, pp. 1008-1013.

[100] C. A. Teixeira, J. Riedel, D. G. Holmes and B. P. McGrath, "Extended

soft switching operation of three-phase dual active bridge converters with unbalanced transformer impedances," *2016 IEEE 2nd Annual Southern Power Electronics Conference (SPEC)*, Auckland, New Zealand, 2016, pp. 1-6.

[101] A. Filba-Martinez, S. Busquets-Monge and J. Bordonau, "Modulation and Capacitor Voltage Balancing Control of Multilevel NPC Dual Active Bridge DC-DC Converters," in *IEEE Transactions on Industrial Electronics*, vol. 67, no. 4, pp. 2499-2510, April 2020.

[102] B. Khanzadeh and T. Thiringer, "Closed-Form ZVS Boundaries for Three-Phase M-Level-to-N-Level DAB Converters With Different Winding Configurations," in *IEEE Transactions on Power Electronics*, vol. 38, no. 7, pp. 8528-8543, July 2023.

[103] D. Wang, B. Nahid-Mobarakeh and A. Emadi, "Second Harmonic Current Reduction for a Battery-Driven Grid Interface With Three-Phase Dual Active Bridge DC-DC Converter," in *IEEE Transactions on Industrial Electronics*, vol. 66, no. 11, pp. 9056-9064, Nov. 2019.

[104] N. Blasuttigh, H. Beiranvand, T. Pereira and M. Liserre, "Comparative Study of Single-phase and Three-phase DAB for EV Charging Application," *2022 24th European Conference on Power Electronics and Applications (EPE'22 ECCE Europe)*, Hanover, Germany, 2022, pp. 1-9.

[105] A. Tong, L. Hang, G. li, X. jiang, and S. Gao, “Modeling and analysis of dual-active-bridge isolated bidirectional DC/DC converter to minimize rms current with whole operating range,” in *IEEE Trans. Power Electron.*, vol. 33, no. 6, pp. 5302-5316, Jun. 2018.

[106] N. Hou, W. Song, and M. Wu, “Minimum-current-stress scheme of dual active bridge DC-DC converter with unified phase-shift control,” in *IEEE Trans. Power Electron.*, vol. 31, no. 12, pp. 8552-8561, Dec. 2016.

[107] H. Shi, H. Wen, J. Chen, Y. Hu, L. Jiang, and G. Chen, “Minimum-reactive power scheme of dual-active-bridge DC-DC converter with three-level modulated phase-shift control,” in *IEEE Trans. Ind. Appl.*, vol. 53, no. 6, pp. 5573-5586, Nov./Dec. 2017.

[108] J. Huang, Y. Wang, Z. Li, and W. Lei, “Unified triple-phase-shift control to minimize current stress and achieve full soft-switching of isolated bidirectional DC-DCconverter,” in *IEEE Trans. Ind. Electron.*, vol.63, no.7,

pp. 4169-4179, Jul. 2016.

[109] K. Takagi and H. Fujita, "Dynamic Control and Performance of a Dual-Active-Bridge DC-DC Converter," in *IEEE Transactions on Power Electronics*, vol. 33, no. 9, pp. 7858-7866, Sept. 2018.

[110] "*IEEE* Standard Definitions for the Measurement of Electric Power Quantities Under Sinusoidal, Nonsinusoidal, Balanced, or Unbalanced Conditions," in *IEEE Std 1459-2010 (Revision of IEEE Std 1459-2000)*, vol., no., pp.1-50, 19 March 2010.

[111] Y. Shen, H. Wang, A. Al-Durra, Z. Qin and F. Blaabjerg, "A Bidirectional Resonant DC-DC Converter Suitable for Wide Voltage Gain Range," in *IEEE Transactions on Power Electronics*, vol. 33, no. 4, pp. 2957-2975, April 2018.

[112] J. Voss and R. W. De Doncker, "Modified Auxiliary-Resonant Commutated Pole Applied in a Three-Phase Dual-Active Bridge DC/DC Converter," in *IEEE Transactions on Power Electronics*, vol. 35, no. 2, pp. 1256-1268, Feb. 2020.

[113] R. Lenke, F. Mura and R. W. De Doncker, "Comparison of non-resonant and super-resonant dual-active ZVS-operated high-power DC-DC converters," *2009 13th European Conference on Power Electronics and Applications*, Barcelona, Spain, 2009, pp. 1-10.

[114] P. Apte, S. Lin, L. Fräger and J. Friebe, "Design Considerations for a 50 kW Dual Bridge Series Resonant DC/DC Converter with Wide-Input Voltage Range for Solid-State Transformers," *2021 IEEE Energy Conversion Congress and Exposition (ECCE)*, Vancouver, BC, Canada, 2021, pp. 1164-1170.

[115] X. Li and A. K. S. Bhat, "Analysis and Design of High-Frequency Isolated Dual-Bridge Series Resonant DC/DC Converter," in *IEEE Transactions on Power Electronics*, vol. 25, no. 4, pp. 850-862, April 2010.

[116] Z. Guo, M. Li and X. Han, "Triple-Phase Shift Modulation Scheme of DAB Converter With LCL Resonant Tank," in *IEEE Transactions on Transportation Electrification*, vol. 8, no. 2, pp. 1734-1747, June 2022.

[117] H. Chen, J. Liu, S. Ouyang, S. Du and X. Li, "A Novel Three Phase LCL Dual Active Bridge Converter to Reduce RMS Phase Current," *2022 IEEE Applied Power Electronics Conference and Exposition (APEC)*, Houston,

TX, USA, 2022, pp. 2154-2158.

[118] A. Z. Khan, K. H. Loo and Y. M. Lai, "Design, Analysis, and Performance Characterization of Dual-Active-Bridge DC-DC Converter Utilizing Three-Phase Resonant Immittance Network," in *IEEE Transactions on Power Electronics*, vol. 34, no. 2, pp. 1159-1180, Feb. 2019.

[119] A. Z Khan, K. H. Loo and Y. Ming Lai, "A Three-Phase Dual-Active-Bridge DC-DC Immittance Converter," *2018 IEEE Energy Conversion Congress and Exposition (ECCE)*, Portland, OR, USA, 2018, pp. 6336-6343.

[120] A. Z. Khan and K. H. Loo, "A Three-Phase Dual-Active-Bridge DC-DC Converter With Reconfigurable Resonant Network for Efficient Wide Voltage Range Operation," in *IEEE Transactions on Power Electronics*, vol. 35, no. 2, pp. 1322-1339, Feb. 2020.

[121] X. She, A. Q. Huang and R. Burgos, "Review of Solid-State Transformer Technologies and Their Application in Power Distribution Systems," in *IEEE Journal of Emerging and Selected Topics in Power Electronics*, vol. 1, no. 3, pp. 186-198, Sept. 2013.

[122] 村山 正樹ほか. リチウム二次電池の充放電における電圧降下に関する考察. 三重県工業研究所研究報告 / 三重県工業研究所 編. (34) 2009年度, p. 23〜29.

[123] 宮代 一, 小林 陽, 中村 龍哉, 関 志朗, 三田 裕一, 宇佐美 章, $LiFePO_4$ を用いた全固体型リチウムポリマー二次電池の基礎特性, Electrochemistry, 2006, 74 巻, 4 号, p. 321-325.

[124] 新国 哲也ほか. 電動車用リチウムイオン電池の劣化と熱的、電気的負荷の影響度について. 交通安全環境研究所フォーラム講演概要 / 交通安全環境研究所 編. 2010 年度, p. 142〜145.

[125] G. A. M. Nasution, M. Matsumoto and M. Hagiwara, "Bidirectional Chopper With Single-Cell Auxiliary Full-Bridge Converter for Onboard Battery Energy Storage System," in *IEEE Transactions on Power Electronics*, vol. 39, no. 8, pp. 10021-10033, Aug. 2024.

[126] 多田 清和ほか. 学生のページ 鉄道用電力変換装置のいろいろ. 電気学会誌 = The journal of the Institute of Electrical Engineers of Japan. 126(8) 2006. 8, p. 550〜553, 514.

[127] 道永 勝久, 東 直親, 作野 敏郎, 山口 雅英, 丸山 真範, 星 吉輝, 鉄道用架線電圧補償装置の開発, パワーエレクトロニクス学会誌, 2007, 33 巻, p. 187-193, 公開日 2010/03/12.

[128] J. Gao *et al.*, "Over 700 mV IBC Solar Cell by Optimizing Front Surface

Field Passivation," in *IEEE Journal of Photovoltaics*, vol. 13, no. 1, pp. 56-60, Jan. 2023.

[129] P. W. Hammond, "A new approach to enhance power quality for medium voltage drives," *Industry Applications Society 42nd Annual Petroleum and Chemical Industry Conference*, Denver, CO, USA, 1995, pp. 231-235.

[130] P. W. Hammond, "A new approach to enhance power quality for medium voltage AC drives," in *IEEE Transactions on Industry Applications*, vol. 33, no. 1, pp. 202-208, Jan.-Feb. 1997.

[131] M. Glinka and R. Marquardt, "A new AC/AC multilevel converter family," in *IEEE Transactions on Industrial Electronics*, vol. 52, no. 3, pp. 662-669, June 2005.

[132] J. S. Lai and F. Z. Peng, "Multilevel converters-A new breed of power converters," *IEEE Trans. Ind. Appl.*, vol. 32, no. 3, pp. 509-517, May/Jun. 1996.

[133] H. Akagi, "Classification, Terminology, and Application of the Modular Multilevel Cascade Converter (MMCC)," in *IEEE Transactions on Power Electronics*, vol. 26, no. 11, pp. 3119-3130, Nov. 2011.

[134] T. Tanaka, K. Ma, H. Wang and F. Blaabjerg, "Asymmetrical Reactive Power Capability of Modular Multilevel Cascade Converter Based STATCOMs for Offshore Wind Farm," in *IEEE Transactions on Power Electronics*, vol. 34, no. 6, pp. 5147-5164, June 2019.

[135] F. Z. Peng, J. S. Lai, J. W. McKeever, and J. VanCoevering, "A multilevel voltage-source inverter with separate dc sources for static Var generation," *IEEE Trans. Ind. Appl.*, vol. 32, no. 5, pp. 1130-1138, Sep./Oct. 1996.

[136] X. Pan, L. Zhang, Y. Li, K. Li and H. Huang, "Modulated Model Predictive Control With Branch and Band Scheme for Unbalanced Load Compensation by MMCC-STATCOM," in *IEEE Transactions on Power Electronics*, vol. 37, no. 8, pp. 8948-8962, Aug. 2022.

[137] L. Qiao, Y. Shimizu and M. Hagiwara, "Current Control of Three-Phase Inverter Using Multiple Bidirectional Choppers Intended for 1.5-kV PV Systems," in *IEEE Transactions on Industry Applications*, vol. 59, no. 1, pp. 910-924, Jan.-Feb. 2023.

[138] H. J. Ahmad and M. Hagiwara, "A Compact High-Power Noninverting Bidirectional Buck-Boost Chopper for Onboard Battery Energy Storage

Systems," in *IEEE Transactions on Power Electronics*, vol. 37, no. 2, pp. 1722-1735, Feb. 2022.

[139] K. Tesaki and M. Hagiwara, "High-efficiency Operation of a Bidirectional Non-isolated DC-DC Converter Based on Flying-capacitor Converters," *2021 IEEE Energy Conversion Congress and Exposition (ECCE)*, Vancouver, BC, Canada, 2021, pp. 1981-1988.

[140] 藤田 英明, 馬渕 雅夫, 坪田 康弘, 溝上 孝生, 可逆チョッパ回路を直列接続したソーラーパワーコンディショナ, 電気学会論文誌Ｄ（産業応用部門誌）, 2012, 132 巻, 1 号, p. 50-57, 公開日 2012/01/01.

[141] H. -C. Chen, P. -H. Wu, C. -T. Lee, C. -W. Wang, C. -H. Yang and P. -T. Cheng, "Zero-Sequence Voltage Injection for DC Capacitor Voltage Balancing Control of the Star-Connected Cascaded H-Bridge PWM Converter Under Unbalanced Grid," in *IEEE Transactions on Industry Applications*, vol. 51, no. 6, pp. 4584-4594, Nov.-Dec. 2015.

[142] L. Qiao and M. Hagiwara, "Evaluation and Performance of Three-Phase Inverter Using Multiple Bidirectional Choppers Intended for 1.5-kVdc PV Systems," in *IEEE Access*, vol. 11, pp. 32636-32647, 2023.

[143] J. S. Song, J. S. Kim, G. J. Cho, C. H. Kim and N. H. Cho, "A Study on Zero Sequence Impedance of 3-limb Core Transformer," *2019 IEEE PES GTD Grand International Conference and Exposition Asia (GTD Asia)*, Bangkok, Thailand, 2019.

[144] P. Pejovic and Z. Janda, "An analysis of three-phase low-harmonic rectifiers applying the third-harmonic current injection," in *IEEE Transactions on Power Electronics*, vol. 14, no. 3, pp. 397-407, May 1999.

[145] D. Menzi, S. Chhawchharia, G. Zulauf, D. Bortis, H. -P. Nee and J. W. Kolar, "Comparative Evaluation of Harmonic Injection Techniques for a Phase-Modular Three-Phase Six-Switch Buck-Boost Y-Inverter," in *IEEE Transactions on Power Electronics*, vol. 37, no. 3, pp. 2519-2524, March 2022.

[146] T. Luo, M. Hagiwara, Y. -C. Su, E. Ferri and L. Piegari, "Operating Principles of Isolated Cascaded-Choppers DC-DC Converter Based on Variable Duty Ratios," in *IEEE Transactions on Industry Applications*, vol. 60, no. 6, pp. 9028-9042, Nov.-Dec. 2024.

PUBLICATIONS

Domestic Conferences

1. Tian Luo ほか. An Isolated DC-DC Converter Featuring Inherent Unity-Power-Factor Operation with Multiple Cascaded Choppers. 電気学会研究会資料. MD / モータドライブ研究会 [編]. 2023(44-56): 2023.1.27, pp.67-72.

International Conferences

1. T. Luo, Y. -C. Su and M. Hagiwara, "Operation and Performance of DC-DC Converter Using Multiple Cascaded Choppers for Future DC Power Grids," *2023 11th International Conference on Power Electronics and ECCE Asia (ICPE 2023 - ECCE Asia)*, Jeju Island, Korea, Republic of, 2023, pp. 1745-1751, doi: 10.23919/ICPE2023-ECCEAsia54778.2023.10213854.

Journals

1. T. Luo, Y. -C. Su and M. Hagiwara, "An Isolated DC-DC Converter With Multiple Cascaded Choppers Featuring RMS Current Reduction Toward Resilient Power Grids," in *IEEE Transactions on Industry Applications*, vol. 60, no. 2, pp. 2249-2263, March-April 2024.
2. T. Luo, M. Hagiwara, Y. -C. Su, E. Ferri and L. Piegari, "Operating Principles of Isolated Cascaded-Choppers DC-DC Converter Based on Variable Duty Ratios," in *IEEE Transactions on Industry Applications*, vol. 60, no. 6, pp. 9028-9042, Nov.-Dec. 2024.

List of Figures

List of Tables

ACKNOWLEDGEMENT

I would like to express my deepest gratitude to the following individuals and organizations who have supported me throughout my doctoral journey:

First and foremost, I wish to thank my advisor, Prof. **Makoto Hagiwara** [萩原　誠], for his invaluable guidance, support, and encouragement. Despite being my advisor, he has never been condescending. Instead, he has always been like a friend, generously sharing your knowledge and maintaining patience with me. I will never forget the meticulous way he helped me review my papers and the times we spent conducting experiments together. Personally speaking, it is my honor to be one of his students.

I am also deeply grateful to Prof. **Hideaki Fujita** [藤田　英明], Prof. **Kenichiro Sano** [佐野　憲一郎], and Prof. **Takahiro Urakabe** [浦壁　隆浩], who are part of the power electronics Lab at Tokyo Tech. Although they are not my direct advisors, they have always been generous with their time and knowledge, to pose thought-provoking and directional academic questions during the seminar presentations, and they are passionate about teaching me how to improve my research. I must say, their suggestions have been incredibly valuable and have provided me with great inspiration.

Moreover, thanks to other professors in my doctoral thesis approving committee, Prof. **Kyohei Kiyota**, Prof. **Nozomi Takeuchi** from Institute of Science Tokyo, and Prof. **Hidemine Obara** from Yokohama National University.

Special thanks to my best friend, **Zheng Zhang**, who is also a Ph.D. student of the power electronics Lab, He is an intelligent and kind-hearted person who enjoys discussing philosophy with me. From him, I have learned to view the world from different perspectives. I wish him the best in successfully completing his studies as well. Also, heartfelt thanks to my beloved girlfriend, **Binlin Shenyang**, for her unwavering support, love, and understanding. I would not have been able to complete this journey without her companionship.

Furthermore, I am profoundly thankful to those important friends who have helped me along the way. **Edoardo Ferri** and **Yuchen Su**, although we have worked together for less than a year, they have both provided me with tremendous help. Likewise, sincerely thanks to those people: **Linyue Qiao** (OB), **Nikola Krneta** (OB), **Shasha Li** (Miyajima Lab), **Lijun Wei** (Junior), **Atsuya Suzuki** (Junior), **Ngo Trong Nhan** (Junior), **Nour Awwad Kamel Hamdan** (Junior), **Kyogo Umano** (Junior), **Ghiffari Aby Malik Nasution** (Same-grade), **Mitsuyoshi Enomoto** (Same-grade), and many others who have helped me in my life or academics.

Lastly, I would like to extend my gratitude to **My Family**. My father, who, despite suffering a stroke, continues to live life with positivity and dedication to his work. He has instilled in me the spirit of never giving up. My mother, the person who loves me most in this world, has always been my salvation in times of need. Truly, my family has been the cornerstone of my life, my most essential source of power.

Postscript

This dissertation represents the culmination of three years of academic work. Personally, I believe it is sufficiently comprehensive. However, here at the conclusion, I want to reflect on what these three years have truly meant to me.

After obtaining my master's degree from Kobe University, I did not choose to enter the workforce. Instead, I embarked on my doctoral journey at Tokyo Tech with somewhat superficial expectations. My master's program was fraught with challenges. I started a research project in an entirely unfamiliar field; everything was new. Nevertheless, I overcame all obstacles, progressing from knowing nothing to achieving some success. At that time, I believed I was professional enough to stand on my own. But once I became a student at the Power Electronics Lab at Tokyo Tech, reality hit me hard. I realized that I am not a genius; there are so many people in the world smarter and even more diligent than me. The knowledge I possess is merely the tip of the iceberg. My advisors, with their profound and vast knowledge, often offered insightful suggestions that took time for me to fully grasp.

I often pondered, "Why does one need a Ph.D.?" and "What can a Ph.D. bring to someone?" Initially, I thought it would earn recognition from others or society and the title of “Dr.”. However, these superficial "rewards" are shallow. I believe that what the PhD has given me is not just a supplement to my knowledge and an enhancement of my abilities, but more importantly, it has changed my way of thinking. I no longer fixate on the "phenomenon" itself but have learned to explore the "essence" behind it. I have become humble and more eager to communicate with those people who are better than me, not just academically, but to enjoy the intellectual friction and resonance with them.

To everyone who reads this dissertation, remember: the world is not as simple as it may seem, and what you see may not necessarily be the truth. Nothing is true, everything is permitted.